Department of Physics and Astronomy
University of Heidelberg

Master's Thesis in Physics
submitted by

David Walther Schönleber

born on April 5, 1988 in Tübingen

2013

Dissipative Dynamics
in Many-Body Rydberg Systems

This master's thesis has been carried out by David Walther Schönleber

at the

Max Planck Institute for Nuclear Physics in Heidelberg

under the supervision of

PD Dr. Jörg Evers

Abstract

Inevitably present in many current experiments with ultracold Rydberg atoms, dissipative effects such as dephasing and decay modify the dynamics of the examined system. In this thesis, the dynamics of many-body Rydberg systems in the incoherent regime is studied numerically. Specifically, a wave function Monte Carlo (MCWF) technique is integrated into a coherent two-level many-body Rydberg model, allowing a numerical simulation of dissipative dynamics. This model is used to benchmark a steady-state rate equation model and assess its range of validity. In addition, incoherent, off-resonant excitation dynamics is studied in a one-dimensional disordered geometry. We find that our simulation results can essentially be explained by the equilibration time scale as well as — for positive laser detuning — resonant excitations arising when the laser detuning compensates the Rydberg interaction. Eventually, we employ a rate equation model to investigate excitation spectra for an experimental trap geometry, which we benchmark using the MCWF technique. Based on numerical data, we deduce that in the considered parameter regime the dominant excitation mechanism can be characterized as sequential growth of aggregates of Rydberg excitations around an initial seed. Our simulation results highlight the impact of incoherent effects on observables such as Rydberg population, excitation number fluctuation and pair correlation function.

Zusammenfassung

Dissipative Effekte wie Dephasierung oder spontaner Zerfall sind unvermeidlich in vielen aktuellen Experimenten mit ultrakalten Rydbergatomen präsent und beeinflussen die Dynamik der untersuchten Systeme. In dieser Arbeit wird die Dynamik von Vielteilchensystemen, bestehend aus Rydbergatomen, im inkohärenten Regime numerisch untersucht. Insbesondere wird eine auf Ebene der Wellenfuktion durchgeführte Monte Carlo (MCWF) Methode in ein kohärentes Zwei-Niveau-Modell von Rydbergatomen implementiert, was eine numerische Simulation dissipativer Zeitentwicklung ermöglicht. Dieses Modell wird für den Benchmark und die Abschätzung des Gültigkeitsbereichs eines Ratengleichungsmodells verwendet, welche Gleichgewichtszustände berechnet. Darüber hinaus wird inkohärente, nichtresonante Anregungsdynamik in einer eindimensionalen, ungeordneten Geometrie untersucht. Es zeigt sich, dass die Simulationsergebnisse hauptsächlich durch die Zeitskala der Equilibrierung sowie — für positive Laserverstimmung — resonante Anregungen erklärt werden können, welche auftreten, wenn die Laserverstimmung die Rydbergwechselwirkung kompensiert. Schließlich verwenden wir eine Ratengleichung, um die Anregungsspektren einer experimentellen Fallengeometrie zu untersuchen, und benchmarken diese mithilfe der MCWF Methode. Auf Grundlage unserer numerischen Daten folgern wir, dass in dem betrachteten Parameterbereich der dominierende Anregungsmechanismus als von einem ursprünglichen Anregungskeim ausgehendes sequenzielles Wachstum von Aggregaten von Rydberganregungen charakterisiert werden kann. Unsere Simulationsergebnisse unterstreichen den Einfluss inkohärenter Effekte auf Observablen wie Rydberganregung, Fluktuation der Anregungszahl sowie Paarkorrelationsfuktion.

Contents

1 Introduction

The field of Rydberg physics has attracted a lot of attention since its establishment in the nineteen seventies [1] and is currently still further growing. Given the extreme properties of Rydberg atoms with respect to their giant size, long lifetimes and huge polarizability leading to strong and long-range interactions [1, 2], the field promises intriguing prospects to study spatially correlated many-body physics [3, 4] as well as nonlinear quantum optics phenomena [5]. Proposed applications range from quantum gates [6–8] required for quantum computing to quantum simulators [9] and atom-light interfaces such as single-atom or single-photon sources [10] and single-photon absorbers [11]. Dressed Rydberg systems are also considered promising candidates for the realization of a supersolid phase [12].

The dipole blockade, denoting the suppression of Rydberg excitations in the vicinity of an already existing excitation, has been extensively studied in the meantime [13–17], it being pivotal for the vast majority of proposed applications. Moreover, the collective enhancement of Rabi oscillations due to the dipole blockade effect has been observed for multiple atoms [18, 19] as well as for a single pair of atoms [20, 21].

Long-range Rydberg-Rydberg interactions can lead to crystalline structures of Rydberg excitations [22, 23], which can also be prepared deterministically by applying chirped laser pulses to the system [24]. Exploiting the dependence of the Rydberg interaction on the principal quantum number, the imaging of Rydberg impurities is made possible [25], opening up a new, auspicious avenue to spatially-resolved excitation measurements in disordered gases.

Another rapidly emerging field of research deals with the study of coupled excitations of light and matter (Rydberg polaritons) [5, 26], which arise when a weak probe field is propagated through a system in an electromagnetically induced transparency (EIT) configuration [27, 28].

Although the afore mentioned experiments usually take place in the ultracold regime at temperatures of few μK, experiments with hot vapor cells ($T \sim 90°$C) have been recently set up, showing evidence of van der Waals-type Rydberg-Rydberg interaction [29]. In addition, the huge spatial extent of the highly excited electronic wave function of a Rydberg state has been utilized to couple a single Rydberg electron to a Bose-Einstein condensate [30].

In theory, there are several possible approaches to modeling interacting many-body Rydberg gases numerically. The first approach is to omit the many-body correlations and employ a mean field approach (cf., for example, Ref. [13]) in which the individual atoms are treated as essentially identical and uncorrelated particles, which allows one in certain cases to incorporate the interaction induced by neighboring atoms into an overall background field. Alternatively, one can simulate the full Schrödinger equation, removing the states that cannot be populated due to the blockade effect (cf. Section 1.3). This procedure is called state space truncation (see e.g. Refs. [22, 31–33]). When inter-atomic coherences are suppressed by incoherent effects, models based on a rate equation enable an efficient simulation of many-body systems with classical correlations [34–38]. Other approaches comprise the cluster expansion model [39], the hybrid model [36], and the Dicke model [40]. Finally, an approach capable of accounting for incoherent processes without coming at the expense of neglected atomic correlations is the wave function Monte Carlo (MCWF) method [41–44]. This approach, which has so far only been applied to lattice geometries, is applied to disordered gases in this work, yielding a technique widely applicable in two-level Rydberg physics.

Introducing the concept of quantum trajectories along the lines of the wave function Monte Carlo method, phase transitions [45] as well as nontrivial spatiotemporal dynamics [46] and collective emission characteristics [47] have been found in lattice geometries by analyzing the photon emission statistics, enabling theoretical analysis by alternative means to pure excitation statistics.

The aim of this thesis is to analyze the dynamics of Rydberg systems in the dissipative regime. To this end, we implement the wave function Monte Carlo technique in an existing code which allows the coherent many-body Schrödinger equation to be solved. With this at hand we can, for the first time, benchmark other two-level many-body models for disordered gases in the dissipative regime, specifically the rate equation, to assess their range of validity. This is of particular interest since the rate equation allows for the fast simulation of large, i.e., experimentally realized systems, but strong approximations enter into the derivation of the rate equation. Hence, a systematic study of the range of validity of the rate equation is highly desirable. Secondly, we use the developed model to study the dynamics of incoherent systems in which collective effects are not negligible and thus effective models such as the rate equation cannot be applied. This is discussed in the first part of the thesis.

In the second part we apply a rate equation to a particular experimental setup to derive conclusions, via thorough analysis of the simulation results, on the dominant mechanism responsible for the strong fluctuations in the excitation numbers observed in the simulation data. To verify the applicability of the rate equation for the parameters used for the modeling, we employ wave function Monte Carlo calculation and find good agreement between two-level rate equation and MCWF simulation.

The thesis is organized as follows: In Sections 1.1 to 1.3 we introduce the most important properties of Rydberg atoms as well as the basics of Rydberg physics, as far as relevant for the understanding of our numerical modeling. We then review in Chapter 2 typical approximations and derive the single-atom and many-body Hamiltonian (Sections 2.1, 2.2) as well as the single-atom and many-body master equation (Sections 2.4, 2.5). In Chapter 3, the two main models already mentioned above are introduced in detail, namely the time-dependent effective two-level rate equation model (Section 3.1) and the wave function Monte Carlo model (Section 3.2). Subsequently, we characterize and comment on the implementation of the wave function Monte Carlo technique in Chapter 4, which allows us to discuss the main results of our simulations in Chapter 5. Chapter 6 addresses simulation results of the rate equation model introduced in Section 3.1 with respect to the particular experimental setup of Ref. [4] and discusses benchmark calculations using wave function Monte Carlo technique. Finally, we summarize our results in Chapter 7 and comment on possible fields of future research.

1.1 Rydberg Atoms

Rydberg atoms are atoms with at least one electron excited to a high principal quantum number n. They were first observed in the *Balmer series* of hydrogen [1], which refers to the spectral lines resulting from the transitions $n \to 2$ with n being a principal quantum number ≥ 3. Rydberg atoms are named after Johannes Rydberg (1854 – 1919), who discovered that the various spectral lines observed for some elements could be assigned to different series which followed a simple formula [48], the Rydberg formula. It was several years later that a theoretical grasp of the physical origins of this phenomenological description was developed by Niels Bohr. Restricting ourselves to the discussion of alkali metals (e.g. Li, Cs or Rb) whose valence electron is excited to a high principal quantum number, the charge seen by the electron is the charge Z of the nucleus shielded by $Z-1$ electrons, resulting in an effective hydrogen-like system. For low angular momentum l, the electronic wave function still penetrates the core, modifying the Coulomb potential seen by the valence electron. Introducing a quantum defect δ_{nlj}, slowly varying with n, the energy levels can be accurately described by the formula [7, 49]

$$E_{nlj} = -\frac{Ry}{(n - \delta_{nlj})^2}\,,\tag{1.1}$$

Property	Scaling behavior
Dipole moment	n^{*2}
Polarizability	n^{*7}
Level spacing of adjacent states	n^{*-3}
Orbital radius	n^{*2}
Lifetime	n^{*3}

Table 1.1: Scaling behavior of selected properties of Rydberg atoms with the effective principal number n^*.

with Ry being the Rydberg constant, $Ry \simeq 13.6 \, \text{eV}$ [50]. For the following discussion, we define the effective principal quantum number as $n^* \equiv n - \delta_{nlj}$. While the binding energy of the Rydberg states scales as n^{*-2}, the level spacing of the adjacent energy levels $E_n - E_{n-1}$ scales as n^{*-3} [2]. Being loosely bound, the electrons are extremely sensitive to electric fields, giving rise to a polarizability scaling as n^{*7} [7]. Moreover, at large principal quantum numbers, the correspondence limit applies and the orbital radius of the electron is adequately described by the Bohr model, which predicts radii of $\sim a_0 n^{*2}$ [1], with a_0 being the Bohr radius, $a_0 \simeq 0.53 \, \text{Å}$ [50]. For $n = 50$, this yields an orbital radius of already $\sim 0.1 \, \mu m$. Since the dipole matrix elements also scale as n^{*2} [2], there is a strong, long-range interaction between Rydberg atoms, which facilitates numerous applications in quantum optics and many-body physics. At zero temperature, when the blackbody contribution to the lifetime of the Rydberg excitation can be safely neglected, the lifetime of the Rydberg excitation scales as $\tau \sim n^{*3}$ [7]. Typical lifetimes are some tens to few hundred μs; for the state $|55S_{1/2}\rangle$ of ^{85}Rb, the lifetime is e.g. $\sim 80 \, \mu s$ [51]. A collection of the most prominent scalings is listed in Table 1.1.

1.2 Rydberg Interaction

Rydberg-Rydberg interactions essentially stem from dipole couplings of energetically nearby states [7]. According to a classical reasoning, the interaction between two Rydberg atoms is given by the electrostatic interaction that is induced by the point charges associated with atomic nuclei and Rydberg electrons respectively, as depicted in Figure 1.1. Assuming that the electron-nucleus distance is much smaller than the distance between the two nuclei, $R_1, R_2 \ll R$, we can expand the electrostatic potential[1]

$$\mathcal{V}_{\text{cl}} = \frac{e^2}{4\pi\varepsilon_0} \left[\frac{1}{|\boldsymbol{R}|} - \frac{1}{|\boldsymbol{R} - \boldsymbol{R}_1|} - \frac{1}{|\boldsymbol{R} + \boldsymbol{R}_2|} + \frac{1}{|\boldsymbol{R} - \boldsymbol{R}_1 + \boldsymbol{R}_2|} \right] \tag{1.2}$$

around R, yielding as leading contribution the dipole-dipole interaction [2]

$$\mathcal{V}_{\text{cl}} = \frac{e^2}{4\pi\varepsilon_0 R^3} \left(\boldsymbol{R}_1 \cdot \boldsymbol{R}_2 - 3(\boldsymbol{R}_1 \cdot \hat{\boldsymbol{R}})(\boldsymbol{R}_2 \cdot \hat{\boldsymbol{R}}) \right), \tag{1.3}$$

with $\hat{\boldsymbol{R}}$ being the unit vector in $\boldsymbol{R}$ direction and e the electron charge.

Moving from classical to quantum mechanics, the classical dipole moments $e\boldsymbol{R}_1, e\boldsymbol{R}_2$ have to be replaced with the dipole operators $e\mathcal{R}_i$, as the correspondence principle requires the replacement of classical observables by quantum mechanical operators. The expectation value of the quantum mechanical dipole operator can be expressed as the expectation value of the

---

[1]The potentials $e^2/|\boldsymbol{R}_1|$, $e^2/|\boldsymbol{R}_2|$ are intra-atomic potentials which do not contribute to the inter-atomic potential $\mathcal{V}_{\text{cl}}$.
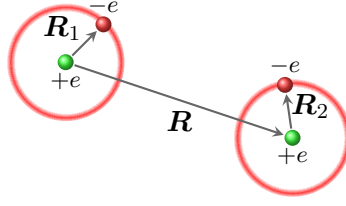
Figure 1.1: Illustration of a two-atomic system in classical terms. The dipole interaction is induced by the point charges associated with positively charged nuclei (green) and negatively charged electrons (red).

radial matrix element [7]

$$\langle nl|\mathcal{R}|n'l'\rangle = \int r R_{nl}(r) R_{n'l'}(r)\, dr \tag{1.4}$$

times the expectation value of the angular part quantified by the spherical harmonics $Y(\theta,\phi)$. In Eq. (1.4), R_{nl} denotes the radial wave function of a Rydberg state with quantum numbers n, l.

In brief, the quantum version of the dipole-dipole interaction (1.3) can be parametrized as

$$\mathcal{V} = \sqrt{D_\varphi}\frac{C_3}{R^3}\,, \tag{1.5}$$

introducing the parameter $C_3 = e^2\langle nl|\mathcal{R}|n'_1 l'_1\rangle\langle nl|\mathcal{R}|n'_2 l'_2\rangle/(4\pi\varepsilon_0)$ and the coefficient D_φ, which contains information about angular momentum coupling (Clebsch-Gordan coefficients) not resolved in C_3 [7]. Note that Eq. (1.5) is only valid if the spatial overlap of the wave functions can be neglected, which is justified if the distance between the atoms is much larger than the extent of the electronic wave function. For the systems discussed in this thesis, this condition is always fulfilled.

The dipole-dipole interaction (1.5) couples energetically neighboring states with energy defect δ which comply with the dipole selection rules $l'_1, l'_2 = l \pm 1$. That is, a quantum system in state $|\psi_{nl}\psi_{nl}\rangle$ with energy E can perform a transition to the state $|\psi_{n'_1 l'_1}\psi_{n'_2 l'_2}\rangle$ with energy E' as a consequence of the dipole interaction, $\langle\psi_{nl}\psi_{nl}|\mathcal{H}|\psi_{n'_1 l'_1}\psi_{n'_2 l'_2}\rangle = \hbar\mathcal{V}$. Here, $\mathcal{H}$ is the Hamiltonian of our system and the quantum defect is given by $\delta = E' - E$.

Disregarding for the moment that in principle multiple states contribute to the dipole coupling, we can set up the Hamiltonian for the two states $\left(|\psi_{n'_1 l'_1}\psi_{n'_2 l'_2}\rangle, |\psi_{nl}\psi_{nl}\rangle\right)^T$, reading

$$\mathcal{H} = \hbar \begin{pmatrix} \delta & \mathcal{V} \\ \mathcal{V} & 0 \end{pmatrix}. \tag{1.6}$$

The energy shift due to the dipole-dipole coupling is readily obtained via diagonalization,

$$\mathcal{V}_{rr} = \frac{\delta}{2} - \text{sign}(\delta)\sqrt{\frac{\delta^2}{4} + \frac{C_3^2}{R^6}D_\varphi}\,. \tag{1.7}$$

At large distances, the energy shift is governed by the energy defect δ, allowing us to expand Eq. (1.7) in $\mathcal{V}/\delta$, resulting in an energy shift of the state $|\psi_{nl}\psi_{nl}\rangle$,

$$\mathcal{V}_{rr} \simeq -\frac{D_\varphi C_3^2}{\delta R^6}\,. \tag{1.8}$$

This is simply a van der Waals-type interaction. At small distances, however, the energy defect becomes negligible compared to the dipole coupling, leading to a R^{-3} behavior of the
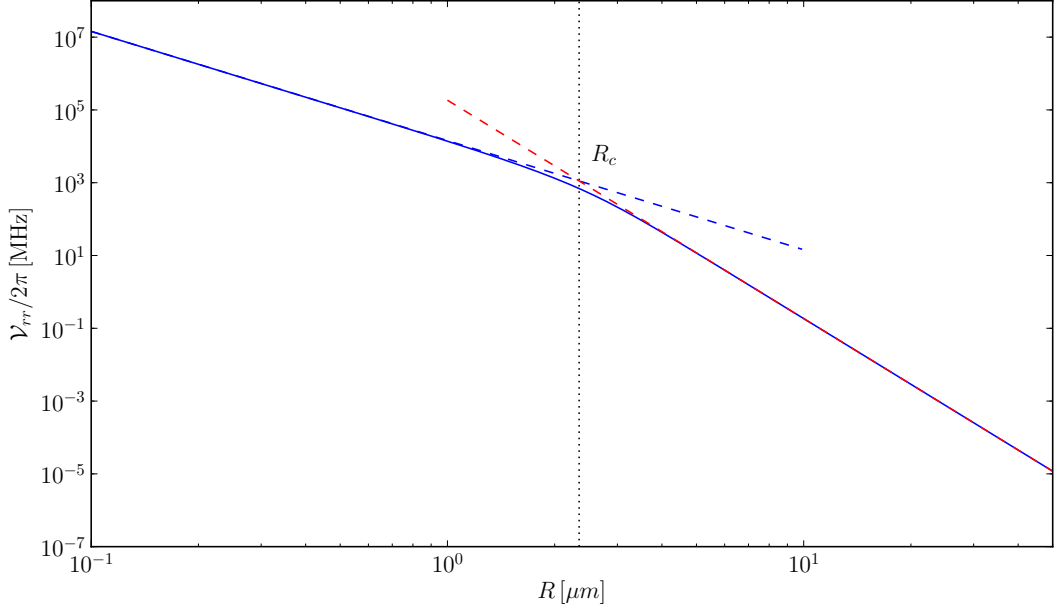
Figure 1.2: Dependence of the energy shift $\mathcal{V}_{rr}$ (solid, blue) on the inter-particle distance R for Rb $|60S_{1/2}\rangle$ (cf. text). The dashed lines indicate R^{-3} scaling (blue) and R^{-6} scaling (red), respectively. The crossover takes place at $R_c = (C_3\sqrt{D_\varphi}/\delta)^{1/3}$ [7].

eigenenergies instead of R^{-6}. In fact, plugging some numbers into Eq. (1.7), i.e., $D_\varphi = 4/3$ [7] and $\delta/2\pi = (E_{n_1'l_1'j_1'} + E_{n_2'l_2'j_2'} - 2E_{nlj})/h = -1.12\,\text{GHz}$, C_3 calculated via the formulas in Ref. [2] using the quantum defects stated in [52], we obtain Figure 1.2, which nicely illustrates the transition between the two scaling regimes. It should be noted, however, that the calculation takes into account only the dominant coupling $|60S_{1/2}\,60S_{1/2}\rangle \leftrightarrow |60P_{3/2}\,59P_{3/2}\rangle$ [53] and not the full manifold of states that would lead to a slightly modified energy shift.

For the sake of convenience, Eq. (1.8) is typically written as C_6/R^6, defining $C_6 = -D_\varphi C_3^2/\delta$. Since the dipole elements scale as n^{*2}, C_3 as n^{*4} and the energy defect as the level spacing n^{*-3}, as listed in Table 1.1, we have [2]

$$C_6 \sim n^{*11}, \tag{1.9}$$

illustrating that Rydberg systems feature strong tunable interactions.

The C_6 coefficient is usually stated in units of $\text{MHz}\,\mu m^6$ and can be calculated from the numerical data given in Ref. [54]; a typical figure is $C_6/2\pi = 16\,000\,\text{MHz}\,\mu m^6$ for the Rubidium $|50S_{1/2}\rangle$ state. For S states, the van der Waals interaction potential is isotropic, as nicely discussed in Ref. [55]. In this thesis, we exclusively study van der Waals-type interaction of S-states.

1.3 Dipole Blockade

One of the most important consequences of the strong dipole-dipole interaction between two Rydberg atoms is what became famous under the name *dipole blockade* [56]. It denotes the prevention of simultaneous excitation of two closely spaced Rydberg atoms due to the Rydberg interaction. This can be most easily understood by considering Figure 1.3. If two excited Rydberg atoms are far apart from each other, the energy shift of the twofold excited state due to dipole-dipole interaction is negligible (dropping off as R^{-6}). Accordingly, two ground state atoms can be simultaneously and independently excited via resonant $|g\rangle \leftrightarrow |r\rangle$ laser driving. Conversely, if the two atoms are closely spaced, the dipole-dipole interaction shifts
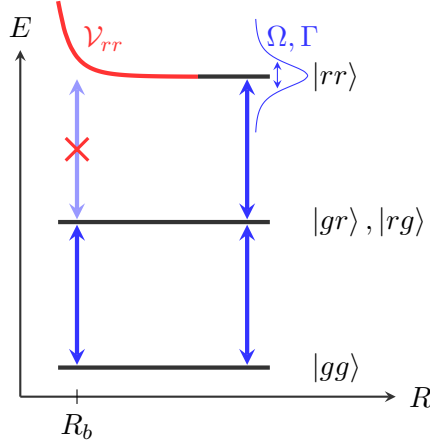
Figure 1.3: Illustration of the dipole blockade effect. The dipole interaction shifts the energy of the doubly excited state out of resonance if two atoms have a distance that is smaller than the blockade radius, $R \lesssim R_b$. The precise value of R_b depends on both the Rabi frequency Ω and the dephasing rate Γ introduced in Chapter 2.

the energy level of the doubly excited state out of resonance, such that the second atom cannot be excited. Thus, both atoms have to share the excitation. Loosely speaking, as soon as two atoms are too closely spaced, the energy provided by the laser field is not sufficient to excite both atoms simultaneously on account of the Rydberg-Rydberg interaction that increases (for repulsively interacting systems) the energy of the doubly excited state. The separation at which the blockade effect sets in is commonly called *blockade radius R_b*.

The dipole blockade not only inhibits nearby Rydberg excitations, it also causes collective effects. In our simple two-atom picture with only one excitation possible, the eigenstates with respect to the laser coupling are no longer the product states $|gr\rangle$, $|rg\rangle$, but rather

$$|+\rangle = \frac{1}{\sqrt{2}} \left(|gr\rangle + |rg\rangle \right), \quad |-\rangle = \frac{1}{\sqrt{2}} \left(|gr\rangle - |rg\rangle \right). \tag{1.10}$$

In this more appropriate basis, introducing the laser Hamiltonian on resonance, $\mathcal{H} = \hbar\Omega/2(|g\rangle\langle r| + h.c.)$, which couples ground and excited state, we immediately see that the antisymmetric state $|-\rangle$ is not coupled at all by the laser field, $\langle gg|\mathcal{H}|-\rangle = 0$. In contrast, the coupling of the symmetric state is enhanced, $\langle gg|\mathcal{H}|+\rangle = \sqrt{2}\,\hbar\Omega/2$. As $\langle gg|\mathcal{H}|gr\rangle = \hbar\Omega/2$, the excitation rate using the symmetric state $|+\rangle$ is enhanced by a factor of $\sqrt{2}$, clearly hinting at collective effects. For a thorough derivation of the laser Hamiltonian we refer to Section 2.1.

The enhancement of the Rabi oscillations holds for any number N_b of blockaded atoms, i.e., the symmetric Dicke state $|+\rangle = 1/\sqrt{N_b} \sum_{\alpha=1}^{N_b} |g_1 \ldots r_\alpha \ldots g_{N_b}\rangle$ is coupled to the collective ground state via the enhanced Rabi frequency $\sqrt{N_b}\Omega$ whereas the $N_b - 1$ antisymmetric states are — in the absence of dephasing — totally decoupled. The collective effects induced by the dipole blockade have been observed for two atoms [20, 21] as well as for many atoms [18, 19]. Since in the blockade regime one excitation is shared by all atoms, it is useful to introduce the concept of a *super atom*, denoting the compound of atoms which share a single excitation [57, 58].

Considering the fact that the energy shift due to the dipole-dipole interaction is distance-dependent, it is clear that the blockade effect is spatially confined. Thus, it is convenient to introduce the blockade radius R_b, which quantifies the spatial extent of the super atom on resonance (i.e., the transition $|g\rangle \leftrightarrow |r\rangle$ is resonant), via the condition

$$\frac{C_6}{R_b^6} = \sqrt{N_b}\Omega, \tag{1.11}$$
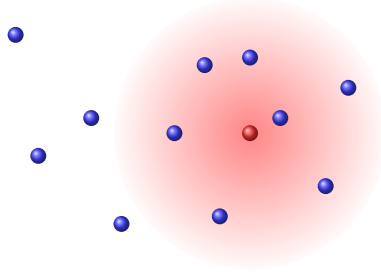
Figure 1.4: Illustration of the super atom picture. Atoms lying inside the blockade sphere of an excited Rydberg atom (radius R_b) are blockaded.

with N_b being the number of blockaded atoms [32]. This condition basically states that the blockade sets in as soon as the interaction-induced energy shift becomes comparable to the (collective) Rabi frequency with which the ground-to-Rydberg transition in the super atom is driven. Estimating the number of blockaded atoms N_b using a homogeneous atomic density ρ in a d-dimensional system ($d \in \{1, 2, 3\}$) via $N_b \sim \rho R_b^d$, we can solve Eq. (1.11) for R_b, yielding [32]

$$R_b \sim \left(\frac{C_6}{\Omega \sqrt{\rho}} \right)^{2/(d+12)}. \tag{1.12}$$

The effect of the blockade radius using the super atom picture is illustrated in Figure 1.4.

Apart from the case where the transition $|g\rangle \leftrightarrow |r\rangle$ is resonant, there is another regime in which an interesting, less explored feature of Rydberg physics arises. That is, for off-resonant laser frequency (i.e., the transition $|g\rangle \leftrightarrow |r\rangle$ is not resonant, but detuned by a detuning Δ), the interaction $\mathcal{V}_{rr}$ can compensate for the detuning, yielding the conditions for single-photon and two-photon resonance [23]

$$\mathcal{V}_{rr} = \Delta \quad \text{and} \quad \mathcal{V}_{rr} = 2\Delta, \tag{1.13}$$

respectively, such that two nearby atoms can be excited indeed, despite the interaction-induced blockade. The latter condition yields the two-photon resonance distance

$$R_{2\gamma} \sim \left(\frac{C_6}{2\Delta} \right)^{1/6}, \tag{1.14}$$

which is smaller than the single-photon resonance distance. These resonances are discussed in detail in the later chapters.

The notion of a super atoms is generally a useful concept as it allows the intuitive derivation of some estimates for a non-trivially interacting many-body system that has to be treated quantum mechanically in principle. It must, however, be treated with care when considering real systems, since the double excitation probability typically is not a $\Theta(R)$ step function of the distance as suggested by the term "blockade radius". Moreover, power broadening of the laser as well as dephasing has a softening impact on the blockade radius, as discussed in Section 5.3 and illustrated in Figure 1.3.

2 Theoretical Background

A sound theoretical description of our system of interest is vital when working towards the modeling of interacting many-body systems. Consequently, we first review the theoretical framework required to describe a single atom coupled coherently to a classical laser field in Section 2.1 and introduce incoherent processes subsequently in Section 2.2. Section 2.3 discusses the reduction of a general three-level scheme to an effective two-level one, which can be simulated with the wave function Monte Carlo technique detailed in Section 3.2. In Section 2.4 and Section 2.5 we generalize the single-atom description to the interacting many-body case for coherent and incoherent systems respectively. This provides us with the necessary means to discuss state-of-the-art techniques to model interacting many-body Rydberg systems, which we do in Chapter 3.

2.1 Single-Atom Hamiltonian

To treat light-atom interactions quantum mechanically, we first need to know how the interaction between light and charged particles influences the energy of the atomic system, i.e., we need to find a suitable Hamiltonian. In semi-classical theory (following Refs. [50, 59]), this can be done by starting from the electromagnetic non-relativistic minimal coupling Hamiltonian, which describes the interaction of an electron with a classical electromagnetic field. In radiation gauge, i.e., using gauge freedom to enforce $\boldsymbol{\nabla} \cdot \boldsymbol{A}(\boldsymbol{r}, t) = 0$, $U(\boldsymbol{r}, t) = 0$ on the gauge potentials, the minimal coupling Hamiltonian reads

$$\mathcal{H}_{\mathrm{mc}} = -\frac{\hbar^2}{2m} \left[\boldsymbol{\nabla} - \frac{iq}{\hbar} \boldsymbol{A}(\boldsymbol{r}, t) \right]^2 + V(\boldsymbol{r}). \tag{2.1}$$

Here, m denotes the mass of the electron at position $\boldsymbol{r}$, q its charge and V its binding potential.

Further employing the *dipole approximation*, which assumes that the wavelength of the incident field is large compared to the size of the atom and hence the variation of the electric field over the distance separating electron and nucleus can be neglected, the vector potential can be approximated by its (constant) value at the nucleus, $\boldsymbol{A}(\boldsymbol{r}, t) \simeq \boldsymbol{A}(\boldsymbol{R}, t)$. Remembering $\partial_t \boldsymbol{A}(\boldsymbol{R}, t) = -\boldsymbol{E}(\boldsymbol{R}, t)$ and performing a gauge transformation on the electronic wave function $\psi(\boldsymbol{r}, t) \to e^{iq/\hbar \, \boldsymbol{r} \cdot \boldsymbol{A}(\boldsymbol{R}, t)} \varphi(\boldsymbol{r}, t)$, we finally obtain

$$i\hbar \partial_t \varphi(\boldsymbol{r}, t) = \left[\frac{p^2}{2m} + V(\boldsymbol{r}) - q\boldsymbol{r} \cdot \boldsymbol{E}(\boldsymbol{R}, t) \right] \varphi(\boldsymbol{r}, t) \tag{2.2}$$

with the momentum operator $p = -i\hbar\nabla$, containing the electromagnetic interaction Hamiltonian in the semi-classical limit

$$\mathcal{H}_{\mathrm{L}} = -q\boldsymbol{r} \cdot \boldsymbol{E}(\boldsymbol{R}, t). \tag{2.3}$$

Having found a way to treat the interaction between a classical electromagnetic field and an electron quantum mechanically, we now aim to remove any explicit time dependence from the laser Hamiltonian $\mathcal{H}_{\mathrm{L}}$. To this end, we assume the electromagnetic field $\boldsymbol{E}(\boldsymbol{R}, t)$ at the center of mass of the atom to be a plane wave and thus write it using the unit vector $\hat{\boldsymbol{\epsilon}}$ as

$$\boldsymbol{E}(t) = \Re \left\{ \mathcal{E} \exp(-i\omega t) \hat{\boldsymbol{\epsilon}} \right\}, \tag{2.4}$$

where $\mathcal{E}$ denotes the field amplitude and ω the carrier frequency. In this notation, the dipole moment between the electronic states i and j is given by $d_{ij} = q \langle \varphi_i | \boldsymbol{r} \cdot \hat{\boldsymbol{\epsilon}} | \varphi_j \rangle$. Typically, the
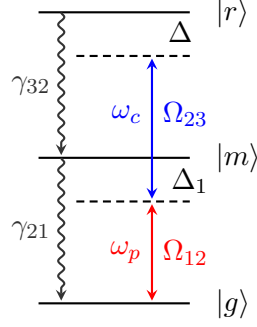
Figure 2.1: Three-level scheme consisting of the states $|g\rangle$, $|m\rangle$ and $|r\rangle$, illustrating the definitions of the laser parameters.

non-vanishing components of the transition moment are constrained by selection rules, such that only one polarization direction $\hat{\epsilon}$ yields a nonzero transition moment [60].

Next, we define the real *Rabi frequency* Ω_{ij} quantifying the strength of the laser coupling as

$$\Omega_{ij}e^{i\phi} = -\frac{\mathcal{E}d_{ij}}{\hbar},\tag{2.5}$$

where the complex degrees of freedom of the Rabi frequency are incorporated via the phase ϕ. By means of these definitions we are now able to rewrite the interaction Hamiltonian (2.3), considering for simplicity's sake only the single electronic transition $|i\rangle \leftrightarrow |j\rangle$ and assuming linear polarization of the electromagnetic field, as

$$(\mathcal{H}_{\mathrm{L}})_{ij} = \hbar\Omega_{ij}e^{i\phi}\cos(\omega t).\tag{2.6}$$

Eq. (2.6) still exhibits an explicit time dependence, which we want to remove. Therefore, we introduce a unitary transformation that changes our frame of reference to a frame rotating with the laser frequencies [52] similar to the interaction picture where the stationary, free Hamiltonian is shuffled into the time evolution of the state vector. In particular, we consider the transformed basis states

$$|\psi(t)\rangle = U(t)|\psi_0(t)\rangle,\tag{2.7}$$

where the index 0 denotes the states before the transformation. For a three-level scheme consisting of ground state $|g\rangle$, intermediate state $|m\rangle$ and Rydberg state $|r\rangle$, the unitary matrix $U(t)$ is given by

$$U(t) = |g\rangle\langle g| + e^{i\omega_p t}|m\rangle\langle m| + e^{i(\omega_p+\omega_c)t}|r\rangle\langle r|,\tag{2.8}$$

with ω_p being the probe laser frequency and ω_c the coupling laser frequency (cf. Figure 2.1). The ground state energy is set to zero as a constant energy offset drops out of any differential equation which quantifies the dynamics of the system.

Calculating the time evolution of the transformed frame we find

$$\begin{aligned}i\hbar\partial_t[U(t)|\psi_0(t)\rangle] &= i\hbar\left([\partial_t U(t)]|\psi_0(t)\rangle + U(t)\partial_t|\psi_0(t)\rangle\right)\\ &= [i\hbar\partial_t U(t) + U(t)\mathcal{H}]|\psi_0(t)\rangle\\ &= \left(i\hbar[\partial_t U(t)]U^\dagger(t) + U(t)\mathcal{H}U^\dagger(t)\right)|\psi(t)\rangle.\end{aligned}\tag{2.9}$$

Accordingly, the transformed system evolves under the counter-rotating Hamiltonian

$$
\begin{aligned}
\mathcal{H}_{\mathrm{rot}} &= i\hbar[\partial_t U(t)]U^\dagger(t) + U(t)\mathcal{H}U^\dagger(t) \\
&= \mathcal{H}_0 + U(t)\mathcal{H}_{\mathrm{L}}U^\dagger(t) - \hbar\omega_p \,|m\rangle\langle m| - \hbar(\omega_p + \omega_c)\,|r\rangle\langle r|,
\end{aligned} \tag{2.10}
$$

where $\mathcal{H}_0$ denotes the stationary Hamiltonian of the free system, which is diagonal in the electronic states and hence commutes with the transformation matrix $U(t)$. Plugging in the definition of $U(t)$ from Eq. (2.8), we obtain after the cancellation of some phases and rearrangement

$$
\begin{aligned}
U(t)\mathcal{H}_{\mathrm{L}}U^\dagger(t) = {} & \frac{\hbar}{2}\Omega_{12}\left[e^{-i\phi_p}(1+e^{-2i\omega_p t})\,|g\rangle\langle m| + e^{i\phi_p}(1+e^{2i\omega_p t})\,|m\rangle\langle g|\right] \\
& + \frac{\hbar}{2}\Omega_{23}\left[e^{-i\phi_c}(1+e^{-2i\omega_c t})\,|m\rangle\langle r| + e^{i\phi_c}(1+e^{2i\omega_c t})\,|r\rangle\langle m|\right].
\end{aligned} \tag{2.11}
$$

Here, ϕ_p and ϕ_c denote the phases corresponding to the transition $|g\rangle \leftrightarrow |m\rangle$ and $|m\rangle \leftrightarrow |r\rangle$, respectively.

The crucial part known as the *rotating wave approximation* (RWA) is now to drop the rapidly oscillating phases $e^{\pm 2i\omega_p t}, e^{\pm 2i\omega_c t}$ as they oscillate on a much faster time scale than the one given by the Rabi frequency Ω_{ij}. In fact, a typical Rabi frequency is of order MHz up to few GHz [17, 29], whereas the carrier frequency (for, e.g., the transition $|g\rangle \leftrightarrow |m\rangle$ with the intermediate state $|m\rangle$ being the $|5P_{3/2}, F=3\rangle$ state and $|g\rangle$ the $|5S_{1/2}, F=2\rangle$ state of ^{87}Rb) is of order $\omega_p/2\pi = c/\lambda_p \sim 10^8$ MHz and hence typically at least four orders of magnitude larger than the Rabi frequency. Thus, since we are usually interested in the dynamics of the electronic states whose coupling to the laser is quantified by the Rabi frequency, the Hamiltonian relevant for us is the one averaged over many carrier frequency cycles. Consequently, we can just drop the time-dependent phases in Eq. (2.11) since they average to zero over a Rabi cycle with period T,

$$
\frac{1}{T}\int_0^T e^{\pm 2i\omega_{p,c}t}dt \sim 0 \quad \text{for} \quad T \gg \max\left\{\frac{1}{\omega_p}, \frac{1}{\omega_c}\right\}. \tag{2.12}
$$

Further simplifying Eq. (2.10) by defining the laser detunings via the laser parameters as

$$
E_m - \omega_p \equiv -\Delta_1, \quad E_r - (\omega_p + \omega_c) = (E_r - E_m) - \omega_c - \Delta_1 \equiv -(\Delta_2 + \Delta_1) \equiv -\Delta, \tag{2.13}
$$

the full single-atom Hamiltonian reads

$$
\mathcal{H}'/\hbar = -\Delta_1\,|m\rangle\langle m| - \Delta\,|r\rangle\langle r| + \frac{\Omega_{12}}{2}\left(e^{-i\phi_p}\,|g\rangle\langle m| + h.c.\right) + \frac{\Omega_{23}}{2}\left(e^{-i\phi_c}\,|m\rangle\langle r| + h.c.\right). \tag{2.14}
$$

For a non-closed three-level scheme meaning that not all the levels are coupled to each other by a laser, we can lastly eliminate the complex degrees of freedom of the Rabi frequencies via a phase transformation of the states according to $\mathcal{H} = P\mathcal{H}'P^\dagger$, where the matrix P is given by

$$
P = e^{i(\phi_p - \eta_2)}\,|g\rangle\langle g| + e^{i\eta_2}\,|m\rangle\langle m| + e^{i(\eta_2 - \phi_c)}\,|r\rangle\langle r|. \tag{2.15}
$$

Hence we finally obtain for the single-atom Hamiltonian in the rotating wave approximation

the real expression

$$\mathcal{H} = \hbar \left[-\Delta_1 \left| m \right\rangle \left\langle m \right| - \Delta \left| r \right\rangle \left\langle r \right| + \frac{\Omega_{12}}{2} \left(\left| g \right\rangle \left\langle m \right| + h.c. \right) + \frac{\Omega_{23}}{2} \left(\left| m \right\rangle \left\langle r \right| + h.c. \right) \right]. \quad (2.16)$$

Note that for a closed scheme this is no longer possible, as can be seen from a simple counting argument. Since we do not want our transformation matrix to mix the different levels, we have to choose a transformation P which is diagonal in the atomic levels. One of the phases in (2.15) can be made a global phase, which drops out immediately in the transformation, consistent with the fact that the quantum states $\left| \psi \right\rangle$ and $e^{i\phi} \left| \psi \right\rangle$ cannot be distinguished by any quantum measurement [61]. Thus, only two phases remain, which can be adjusted to remove the complex degrees of freedom of the Rabi frequencies, leaving one Rabi frequency complex.

In Figure 2.1, the three-level scheme corresponding to the Hamiltonian (2.16) is depicted; the colors indicate the wavelengths of the laser light that is typically used for the corresponding transition.

The Hamiltonian (2.16) only describes the dynamics of a single atom correctly if an additional approximation, the *frozen gas approximation*, is employed. In this approximation, the motional degrees of freedom of the atom are neglected, assuming that the atom stays at its initial position for all times. Without a doubt, this approximation is never met exactly in experiments; however, as we model gases in the ultracold regime at typical temperatures of a few up to some ten μK [5, 17, 19], the thermal motion is of the order of $\approx 10 \, nm/\mu s$ and can thus be neglected for typical excitation times of a few μs.

Although different conventions exist (cf., for example, Refs. [3, 4]), the Rabi frequency as well as other terms contained in the Hamiltonian (2.16) are usually stated in units of MHz (frequency), while in the Hamiltonian the angular frequency ($\times 2\pi$) is plugged in. This is consistent with the fact that the Schrödinger as well as the von Neumann equation (2.18) contain the reduced Planck constant and not the plain Planck constant and thus allow to obtain the time evolution by solving the respective differential equations in proper time units. This can be easily seen by noting that for a two-level system on resonance, the inversion $\rho_{rr}(t) - \rho_{gg}(t)$ is just $-\cos(\Omega t)$ [59]. As the cosine is 2π periodic, we obtain Rabi oscillations with the period given by the inverse Rabi frequency (not the angular frequency). Alternatively, one can plug in mere frequencies in the Hamiltonian and shuffle the 2π into the time units (which is sometimes done in theory), such that $t = t'/2\pi$, where t' denotes the simulated time and t the 'real' time. To avoid confusion, we stick to the most commonly used convention, which states the parameters in units of frequency, i.e., when speaking of a Rabi frequency we refer to the quantity $\Omega/2\pi$ with Ω as defined in Eq. (2.5).

2.2 Single-Atom Master Equation

Up to now, we have only considered coherent dynamics, i.e., we considered *closed* quantum systems, meaning that there is no exchange of any information or the like[2] with the environment [63], such that the dynamics of the system is completely described by a hermitian, possibly time-dependent Hamiltonian.

Expecting that coupling our system of interest to a surrounding environment might change the coherence properties of our system, we ought to switch over to the *density matrix* formalism,

---

[2]Note that, strictly speaking, an atomic system interacting with a laser is no longer a *closed* system. However, it turns out that the dynamics of the atomic states is almost perfectly described by the atomic Hamiltonian introduced before [62]. This is why we refer to an atomic system interacting with classical laser light as to a closed system.

which allows for a statistical mixture of our system states. A numerically-equivalent method to this approach without employing a density matrix is being discussed in Section 3.2.

Considering an *open* system consisting of a quantum mechanical system S coupled to a reservoir R, the dynamics of the (closed) composite system $S + R$ can be described by the Hamiltonian

$$\mathcal{H} = \mathcal{H}_S + \mathcal{H}_R + \mathcal{H}_I, \tag{2.17}$$

where we have introduced the system and reservoir Hamiltonians $\mathcal{H}_S$ and $\mathcal{H}_R$ respectively, as well as the the Hamiltonian $\mathcal{H}_I \equiv \mathcal{I}_S \otimes \mathcal{I}_R$ describing the interaction between system and reservoir. Thus, in the interaction picture, the equations of motion for the total density matrix ρ read

$$i\hbar\partial_t\rho(t) = [\mathcal{H}_I(t), \rho(t)]. \tag{2.18}$$

Assuming weak coupling between the system and the reservoir, we can, as a perturbative expansion, insert the integral form of the von Neumann equation (2.18) back into Eq. (2.18) and find[3]

$$\partial_t\rho_S(t) = \mathrm{Tr}_R\left\{-\frac{i}{\hbar}[\mathcal{H}_I(t), \rho(0)]\right\} - \frac{1}{\hbar^2}\int_0^t d\tau\,\mathrm{Tr}_R\left\{[\mathcal{H}_I(t), [\mathcal{H}_I(\tau), \rho(\tau)]]\right\}. \tag{2.19}$$

Here, the partial trace over the reservoir has been inserted since we are only interested in the system dynamics. Eq. (2.19) can be further simplified by assuming

$$\mathrm{Tr}_R\left\{[\mathcal{H}_I(t), \rho(0)]\right\} = 0, \tag{2.20}$$

which is always possible to obtain by modifying both system and interaction Hamiltonian [64].

The next important step is now to replace the total density matrix by the tensor product $\rho(t) \sim \rho_S(t) \otimes \rho_R$, since in the weak coupling limit the reservoir is hardly affected by its interaction with the system. This approximation is known as *Born approximation*. Still, Eq. (2.19) is hard to solve, being non-local in time. We thus employ another approximation, known as the *Markov approximation*, which states that if the reservoir correlation time is much smaller than the typical time scale of the system, we can replace $\rho(\tau)$ by $\rho(t)$. This is a valid approximation if the system couples to (infinitely) many reservoir energy levels. To see this, we note that if the reservoir Hamiltonian commutes with the reservoir density matrix, the reservoir correlation function $\mathrm{Tr}_R\left\{\mathcal{I}_R(t)\mathcal{I}_R(\tau)\rho_R\right\}$ depends only on the difference of the time arguments[4] $|t - \tau|$. For a dense energy spectrum, the correlation function peaks strongly around $t = \tau$, implying that the system loses all memory about its past.

As a last step, we need to remove the remaining dependence on the system configuration at $t = 0$ to obtain a truly Markovian equation, which can — arguing along the lines above — be done by replacing the lower limit of the integral in (2.19) by $-\infty$. Thus, we finally obtain the *Born-Markov* master equation

$$\partial_t\rho_S(t) = -\frac{1}{\hbar^2}\int_{-\infty}^t d\tau\,\mathrm{Tr}_R\left\{[\mathcal{H}_I(t), [\mathcal{H}_I(\tau), \rho_S(t) \otimes \rho_R]]\right\}. \tag{2.21}$$

However, to obtain a master equation of Lindblad type, i.e., an hermitian equation preserving

---

[3]Though the interaction is weak, we cannot stay with Eq. (2.18) since only the second-order equation yields a non-vanishing contribution to the master equation.

[4]Inserting the definition $\mathcal{I}_R(t) = e^{i\mathcal{H}_R t/\hbar}\mathcal{I}_R e^{-i\mathcal{H}_R t/\hbar}$ into the trace yields this result immediately.

trace and positivity of the density matrix equation, we need to apply yet another approximation, namely the *rotating wave approximation* (which is, in this context, also known as *secular* approximation) discussed before. The demand for a master equation of Lindblad type stems from the fact that Eq. (2.21) does not necessarily preserve the positivity of the density matrix, which might lead to non-physical 'probabilities'. Accordingly, it is to a master equation of Lindblad type that we refer whenever we refer to a 'master equation' in the following. Furthermore, we are only interested in long-term observables for which the performed approximations (i.e., the Markov and the rotating wave approximation) are valid. A more detailed discussion of the master equation derivation can be found in Refs. [62, 64, 65].

As mentioned before, the major advantage of the master equation over the standard Schrödinger equation is that it allows for the inclusion of incoherent effects arising via the interaction of the system with its environment. Despite the multitude of incoherent processes, we will limit ourselves to *dephasing* and *decay* as they comprise the most important incoherent effects occurring in experiments.

For the sake of convenience, we now introduce the Lindblad super-operator [62]

$$\mathcal{L}(\mathcal{C})[\rho] = \mathcal{C}\rho\mathcal{C}^\dagger - \frac{1}{2}\left(\mathcal{C}^\dagger\mathcal{C}\rho + \rho\mathcal{C}^\dagger\mathcal{C}\right), \tag{2.22}$$

where $\mathcal{C}$ denotes a jump operator corresponding to an incoherent process and ρ is the reduced density matrix $\rho = \mathrm{Tr}_R\{\rho_S(t) \otimes \rho_R\}$.

For spontaneous emission (i.e., decay), the jump operators corresponding to the decays $|r\rangle \to |m\rangle$ and $|m\rangle \to |g\rangle$ in our three-level system (cf. Figure 2.1) read

$$\mathcal{C}_{\gamma_{32}} = \sqrt{\gamma_{32}}\,|m\rangle\langle r| \quad \text{and} \quad \mathcal{C}_{\gamma_{21}} = \sqrt{\gamma_{21}}\,|g\rangle\langle m| \tag{2.23}$$

respectively. Here, γ_{32} denotes the rate by which the population of the excited atomic state $|r\rangle$ is transferred to the energetically lower lying state $|m\rangle$ via photon emission into the vacuum. As the decay rates γ_{ij} are proportional to the modulus of the the dipole matrix element of the respective transition, selection rules apply to spontaneous emission as well, such that the decay $|r\rangle \to |g\rangle$ is strongly suppressed in a three-level scheme with the Rydberg state being an S state. Spontaneous emission is usually derived by assuming the system to couple to either a reservoir of simple harmonic oscillators in thermal equilibrium at zero temperature or via Weisskopf-Wigner theory, assuming coupling to infinite, closely spaced cavity modes with an emission spectrum centered at the atomic transition frequency [59].

Dephasing, conversely, denotes the process where atomic coherences decay in an atomic system. In general, one can distinguish between two types of dephasing, namely homogeneous and inhomogeneous dephasing [11]. Homogeneous dephasing acts on all atoms in the same way, which is the case for, e.g., fluctuations in the laser frequency being due to a finite (Lorentzian) laser linewidth. This laser linewidth-induced type of dephasing only affects the off-diagonal part of the Lindblad term by which the coherences decay, resulting in the super-operator

$$\mathcal{L}'(\Gamma_{ij}, i \leftrightarrow j)[\rho] = -\frac{\Gamma_{ij}}{2}\left(|i\rangle\langle i|\,\rho\,|j\rangle\langle j| + h.c.\right), \tag{2.24}$$

with i, j being the states coupled by the laser and Γ_{ij} the dephasing rate [66]. If two states are indirectly coupled (as the case for the states $|g\rangle$ and $|r\rangle$ in Figure 2.1), one has to add a dephasing term with $\Gamma_{31} \sim \Gamma_{32} + \Gamma_{21}$, accounting for the convolution of the two Lorentzians, which is again a Lorentzian whose width equals the sum of the single Lorentzian widths.

Inhomogeneous dephasing in turn influences each atom individually, which is the case for e.g. motion-induced Doppler shifts or a speckle light field with short range correlations in time and space (see Ref. [11] and Section 2.4). This type of dephasing can be described using

the standard Lindblad super-operator $\mathcal{L}(\sqrt{\Gamma_i} \left|i\right\rangle \left\langle i\right|)[\rho]$.

Having now collected all the incoherent terms from above, we arrive at the full single-atom master equation

$$
\begin{aligned}
\partial_t \rho(t) = {} & -\frac{i}{\hbar}[\mathcal{H}, \rho] \\
& + \mathcal{L}(\sqrt{\gamma_{32}} \left|m\right\rangle \left\langle r\right|)[\rho] + \mathcal{L}(\sqrt{\gamma_{21}} \left|g\right\rangle \left\langle m\right|)[\rho] \\
& + \mathcal{L}'(\Gamma_{32}, 3 \leftrightarrow 2)[\rho] + \mathcal{L}'(\Gamma_{21}, 2 \leftrightarrow 1)[\rho] + \mathcal{L}'(\Gamma_{32} + \Gamma_{21}, 3 \leftrightarrow 1)[\rho] \\
& + \mathcal{L}(\sqrt{\Gamma_3} \left|r\right\rangle \left\langle r\right|)[\rho] + \mathcal{L}(\sqrt{\Gamma_2} \left|m\right\rangle \left\langle m\right|)[\rho].
\end{aligned}
\tag{2.25}
$$

In Eq. (2.25), the first line describes the coherent evolution using the Hamiltonian (2.16), the second one spontaneous emission processes and the last two lines dephasing processes due to laser linewidth and e.g. motional dephasing respectively.

2.3 Two-Level Approximation

From a computational point of view, it is very challenging to calculate the exact dynamics of the full three-level master equation (2.25) for multiple atoms (cf. Chapter 3). In the usual two-step excitation scheme depicted in Figure 2.1, the intermediate level $\left|m\right\rangle$ is typically weakly coupled and far detuned,

$$
|\Delta_1| \gg |\Delta| \quad \text{and} \quad |\Delta_1| \gg \sqrt{\Omega_{12}^2 + \Omega_{23}^2}, \tag{2.26}
$$

such that the population of the intermediate state stays small. In this case also the dynamics of the intermediate state is much faster than the dynamics between the states $\left|g\right\rangle \leftrightarrow \left|r\right\rangle$. Focusing on the slow dynamics, we can therefore approximate [67]

$$
\partial_t \left|\psi_m(t)\right\rangle \sim 0, \tag{2.27}
$$

where $\left|\psi_m\right\rangle$ denotes the wave function of the intermediate state. Solving the Schrödinger equation $i\hbar \partial_t \left|\psi\right\rangle = \mathcal{H} \left|\psi\right\rangle$ with $\mathcal{H}$ from Eq. (2.16) under the constraint $\left|\psi_m(0)\right\rangle = 0$, we obtain the effective Hamiltonian after adiabatic elimination, with the effective Rabi frequency $\Omega_{12}\Omega_{23}/2\Delta_1$ [67],

$$
\mathcal{H}_{2\text{lvl}} = \frac{\hbar}{2} \begin{pmatrix} \dfrac{\Omega_{12}^2}{2\Delta_1} & \dfrac{\Omega_{12}\Omega_{23}}{2\Delta_1} \\ \dfrac{\Omega_{12}\Omega_{23}}{2\Delta_1} & -2\Delta + \dfrac{\Omega_{23}^2}{2\Delta_1} \end{pmatrix}. \tag{2.28}
$$

For pulsed excitation using a smooth pulse, i.e., if $\Omega(t)$ is pulse-shaped, the condition on the detuning can be significantly relaxed if one is mainly interested in the system's state after the pulse [68].

Note that there is an additional detuning shift of $(\Omega_{23}^2 - \Omega_{12}^2)/2\Delta_1$ introduced by the adiabatic elimination procedure, which needs to be accounted for when comparing, for instance, two-level simulation results with experimental three-level data.

The adiabatic elimination procedure, which is illustrated in Figure 2.2, is only applicable in the coherent case, which we do not consider too much in this thesis. In the incoherent case, there is no trivial mapping of a three-level system onto an effective two-level system without employing rather strong approximations such as extremely weak coupling [69], where the perturbative expansion of the laser driving can be stopped at a low order, or the presence of strong decoherence sources, which destroy any atomic coherences and allow for an effective
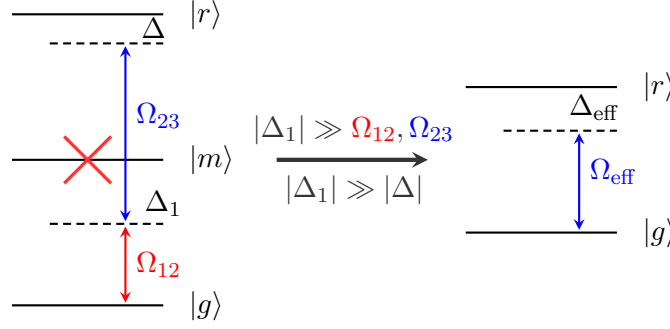
Figure 2.2: Illustration of the adiabatic elimination procedure of the intermediate level discussed in Section 2.3.

description [35]. These rather strong assumptions have to be made since the master equation resulting from a similar elimination procedure as discussed above is typically not of Lindblad form, which allows for negative populations and renders computation with the methods developed in Section 3.2 impossible. In addition, an EIT configuration (discussed e.g. in Ref. [17]) cannot be reduced to a two-level description, which, together with the afore mentioned assumptions, sets clear limitations on the adiabatic elimination method. In certain cases, these constraints might be relaxed by using more involved perturbation theory [70].

Note that even though we will primarily consider two-level systems in the following, we do not rely on the Hamiltonian (2.28). Rather, we regard the adiabatic elimination procedure discussed above as a justification to consider instead of a three-level Rydberg system consisting of the states $|g\rangle$, $|m\rangle$ and $|r\rangle$ a two-level system consisting of the states $|g\rangle$ and $|r\rangle$ only, assuming we have reasonable estimates for the effective parameters Ω, Δ, γ and Γ.

2.4 Many-Body Hamiltonian

In what has been discussed so far, we only considered a single atom interacting with a classical laser field and a decoherence-inducing environment. The intriguing feature of Rydberg physics, however, is the non-trivial many-body dynamics that is brought about by Rydberg-Rydberg interaction. Thus, we need to take a step further and generalize Eqs. (2.16), (2.25) to an interacting many-body case.

To improve readability, we set $\hbar$ to 1 in the following. Moreover, internal atomic degrees of freedom (such as electronic states) are labeled using Roman letters whereas the individual atoms are labeled using Greek letters.

Starting from the single-atom Hamiltonian (2.16), the many-body Hamiltonian of a cloud of N Rydberg atoms is — up to the Rydberg-Rydberg interaction — straightforwardly obtained by summing up the single-atom contributions [2, 7, 57, 71],

$$\mathcal{H}_{\text{iso}} = \sum_{\alpha=1}^{N} \left(\frac{\Omega_{12}^{(\alpha)}}{2} \left(|g_\alpha\rangle \langle r_\alpha| + h.c. \right) - \Delta^{(\alpha)} |r_\alpha\rangle \langle r_\alpha| \right). \tag{2.29}$$

Here, we explicitly allowed for an individual detuning $\Delta^{(\alpha)}$ as well as an individual Rabi frequency $\Omega_{12}^{(\alpha)}$. Often, however, these parameters will be the same for all atoms.

As a side note, transforming into the many-body basis $|\sigma_1 \sigma_2 \ldots \sigma_N\rangle$ with $\sigma_\alpha \in \{g, r\}$, we see that each Rydberg excitation contributes a detuning shift of $-\Delta$ to the total detuning of the state; moreover, only states differing by one excitation are coupled via the laser Hamiltonian $\mathcal{H}_{\text{L}}$. These observations are useful when aiming at implementing the many-body Hamiltonian

numerically [33].

The interaction between the Rydberg states can be included via the Hamiltonian $\mathcal{V}_{rr}$ which accounts for the repulsive van der Waals interaction,

$$\mathcal{V}_{rr} = \sum_{\alpha < \beta}^{N} \frac{C_6}{|\mathbf{R}_\alpha - \mathbf{R}_\beta|^6} |r_\alpha\rangle \langle r_\alpha| \otimes |r_\beta\rangle \langle r_\beta|, \tag{2.30}$$

with $\mathbf{R}_{\alpha,\beta}$ denoting the position of the atoms α and β respectively. The validity of Eq. (2.30) requires that the interparticle distance is much larger than the size of the Rydberg atom wave function such that the interaction between the atoms can only be due to dipole-dipole interactions.

In addition, as discussed in [31], modeling Rydberg-Rydberg interactions via pairwise interactions is only valid as long as the energy defect of the (nearest) Förster resonance is large compared to the largest dipole coupling. By Förster resonances we denote energy-exchange resonances of type $r_1 + r_2 \leftrightarrow r_1' + r_2'$ of two Rydberg states r_1, r_2 [2]. For van der Waals-type interaction, however, approximating the Rydberg-Rydberg interaction by pairwise interactions is valid, an assumption used throughout this thesis.

Hence, using the definitions from above, the general full many-body two-level Hamiltonian reads

$$\mathcal{H} = \sum_{\alpha=1}^{N} \left(\frac{\Omega_{12}^{(\alpha)}}{2} \left(|g_\alpha\rangle \langle r_\alpha| + h.c. \right) - \Delta^{(\alpha)} |r_\alpha\rangle \langle r_\alpha| \right)$$
$$+ \sum_{\alpha<\beta}^{N} \frac{C_6}{|\mathbf{R}_\alpha - \mathbf{R}_\beta|^6} |r_\alpha\rangle \langle r_\alpha| \otimes |r_\beta\rangle \langle r_\beta|. \tag{2.31}$$

2.5 Many-Body Master Equation

From all this, the extension of the master equation to the many-body case seems obvious, except for the caveat that we need to be sure that incoherent processes such as dephasing and decay are not modified by the presence of other atoms. In fact, collective effects such as superradiance can occur in systems in which the interparticle distance is much smaller than the wavelength corresponding to the dipole transition $|g\rangle \leftrightarrow |m\rangle$, e.g., through which the intermediate state decays [72]. In this *Dicke limit*, the dipole elements can mix, leading to superradiance [72]. For this reason we compare along the lines of Ref. [35] the typical interparticle distances in current experiments to the wavelength of the transition $|g\rangle \leftrightarrow |m\rangle$ by means of the dimensionless quantity $x \equiv k_p \bar{R} = 2\pi\bar{R}/\lambda_p$ with $\bar{R}$ being the mean interparticle distance and $\lambda_p = 2\pi c/\omega_p$. For $x \ll 1$, superradiant effects are dominant whereas superradiance is negligible for $x \gg 1$. In our simulations, $x \gtrsim 1$, so we neglect the impact of superradiance in this thesis[5].

Given the independence of incoherent processes, the full many-body master equation becomes

$$\partial_t \boldsymbol{\rho} = -i[\mathcal{H}, \boldsymbol{\rho}] + \sum_{\alpha=1}^{N} \left(\mathcal{L}(\sqrt{\gamma_{21}} |g_\alpha\rangle \langle r_\alpha|)[\boldsymbol{\rho}] + \mathcal{L}(\sqrt{\Gamma_2} |r_\alpha\rangle \langle r_\alpha|)[\boldsymbol{\rho}] \right), \tag{2.32}$$

where $\mathcal{H}$ is the many-body Hamiltonian (2.31) and $\boldsymbol{\rho}$ the many-body density matrix.

Let us now supplement the previous discussion about inhomogeneous dephasing with a more rigorous treatment, starting from Eq. (2.21). Dropping the index S whenever the reservoir

---

[5]To obtain this relation, we assumed $\lambda_p = 780\,\mathrm{nm}$ as the case for the two-step excitation scheme in the experiments [4, 17, 29].

is already traced out, the Lindblad term used to model inhomogeneous dephasing can be derived from Eq. (2.21) by utilizing the microscopic noise term [11]

$$\mathcal{H}_{\text{noise}} = \sum_{\alpha=1}^{N} \Delta^{(\alpha)}(t) \left|r_\alpha\right\rangle \left\langle r_\alpha\right|, \tag{2.33}$$

where $\Delta^{(\alpha)}$ denotes an ac stark shift of the Rydberg level, being different for every atom α. Assuming further uncorrelated white noise, $\langle \Delta^{(\alpha)}(t)\Delta^{(\beta)}(\tau)\rangle = \Gamma/2\delta_{\alpha\beta}\delta(t-\tau)$, where the correlation function is defined in the reservoir subspace, $\langle\,\cdot\,\rangle = \text{Tr}_R\{\cdot\,\rho_R\}$, we find

$$
\begin{aligned}
\partial_t \boldsymbol{\rho} = & -\int_{-\infty}^{t} d\tau \sum_{\alpha,\beta} \text{Tr}_R \Big\{ \Delta^{(\alpha)}(t)\Delta^{(\beta)}(\tau) \left|r_\alpha\right\rangle \left\langle r_\alpha\right| \otimes \left|r_\beta\right\rangle \left\langle r_\beta\right| \boldsymbol{\rho}_S \otimes \rho_R + h.c. \\
& -\Delta^{(\alpha)}(t) \left|r_\alpha\right\rangle \left\langle r_\alpha\right| \boldsymbol{\rho}_S \otimes \rho_R \, \Delta^{(\beta)}(\tau) \left|r_\beta\right\rangle \left\langle r_\beta\right| + h.c. \Big\} \\
= & -\frac{\Gamma}{2} \sum_\alpha \int_{-\infty}^{t} d\tau\, \delta(t-\tau) \left(\left|r_\alpha\right\rangle \left\langle r_\alpha\right| \boldsymbol{\rho} - \left|r_\alpha\right\rangle \left\langle r_\alpha\right| \boldsymbol{\rho} \left|r_\alpha\right\rangle \left\langle r_\alpha\right| + h.c. \right) \\
= & \sum_\alpha \mathcal{L}(\sqrt{\Gamma} \left|r_\alpha\right\rangle \left\langle r_\alpha\right|)[\boldsymbol{\rho}].
\end{aligned}
\tag{2.34}
$$

Note that, in the two-level case at least, the two dephasing terms $\mathcal{L}(\sqrt{\Gamma_2} \left|r_\alpha\right\rangle \left\langle r_\alpha\right|)[\rho]$ and $\mathcal{L}'(\Gamma_2, 1_\alpha \leftrightarrow 2_\alpha)[\rho]$ introduced in Eqs. (2.22), (2.24) coincide. Moreover, the super-operator $\mathcal{L}'^{(\alpha)}(\Gamma_2, 1_\alpha \leftrightarrow 2_\alpha)[\rho]$ can be rewritten to fit the standard Lindblad form as [44]

$$\mathcal{L}'(\Gamma_2, 1_\alpha \leftrightarrow 2_\alpha)[\boldsymbol{\rho}] = \mathcal{L}\left(\frac{\sqrt{\Gamma_2}}{2} (\left|r_\alpha\right\rangle \left\langle r_\alpha\right| - \left|g_\alpha\right\rangle \left\langle g_\alpha\right|) \right)[\boldsymbol{\rho}]. \tag{2.35}$$

However, no measurement process can be assigned to the Lindblad jump operator introduced in Eq. (2.35), which collapses the atomic wave function to a theoretically infinite number of final states [44, 73]. To avoid this issue and maintain a physical interpretable jump operator without employing the cumbersome quantum-jump technique described in Ref. [73], we will stick to the dephasing term introduced in Eq. (2.34) in the following.

Operator (2.35) (and, equivalently, the dephasing term in Eq. (2.34)) can be also used to model the effect of atomic collisions [74] and has been used in Ref. [75] to model dephasing induced by both laser linewidth and decay from the eliminated intermediate state $\left|m\right\rangle$.

Lastly, it should be noted that the dephasing constants plugged into the respective Lindblad terms in Eq. (2.35) differ by a factor of 4, which needs to be adjusted when comparing simulations that employ different definitions of the Lindblad operator modeling atomic dephasing. Specifically, the dephasing constant Γ' pertaining to the jump operator $\Gamma'(\left|r\right\rangle \left\langle r\right| - \left|g\right\rangle \left\langle g\right|)$ is actually $4 \times \Gamma$ with Γ pertaining to our conventional jump operator $\Gamma \left|r\right\rangle \left\langle r\right|$.

3 Modeling

The task of simulating an interacting many-body system quantum mechanically is quite challenging from a computational perspective since the Hilbert space of a many-body system grows exponentially with the number of atoms. More precisely, the number of basis states for a system consisting of N atoms, each having l levels, is given by l^N. From a technical point of view this implies, assuming the complex amplitude of each state being stored in a variable of type double (8 bytes) each, that $N < 30$ for a two-level system and $N < 19$ for a three-level system, to not exhaust a typical RAM of 16 GB, not considering the feasibility to solve coupled differential equations of that size. If one wants to take into account incoherent effects as well by means of the density matrix formalism, the state space grows as l^{2N}, lowering the limit based on memory arguments alone to $N < 19$ for a two-level system and $N < 9$ for a three-level system.

Several approaches have been developed to tackle this problem, each having its own range of validity. In this thesis, we focus primarily on the two main approaches, namely the rate equation approach (Section 3.1, Chapter 6) and the wave function Monte Carlo approach (Section 3.2, Chapter 4 and 5). For other approaches, see Chapter 1 and the references introduced there.

3.1 Rate Equation Model

The main idea behind the rate equation model first introduced in Refs. [34, 35] is to reduce the many-body master equation to a rate equation for the populations of the many-body states, taking into account the Rydberg-Rydberg interaction via an effective energy shift of the Rydberg level depending on the state of the surrounding atoms. The resulting equations can be solved numerically very efficiently via Monte Carlo algorithms, allowing one to simulate systems consisting of several thousands of atoms. In addition, the rate equation approach can — with some caveats — be generalized to a three-level description, which can still be solved efficiently. Though there are some variations in what is meant in particular by "rate equation model", we discuss the rate equation model developed in Ref. [35] in the following since it is this kind of rate equation model which was used to model the experiments described in Ref. [4]. Later on we also comment on the modifications introduced in Ref. [36].

As discussed in Section 2.5, it is valid under typical experimental conditions to write the Lindblad terms appearing in the many-body master equation simply as the sum of the individual single-atom Lindblad terms given by Eq. (2.25), which — neglecting for the moment the Rydberg interaction between the atoms — yields a totally decoupled master equation for each atom. The main approximation at this level is now to adiabatically eliminate the atomic coherences by setting

$$\partial_t \rho_{ij} = 0 \quad \text{for} \quad i \neq j. \tag{3.1}$$

This is a valid approximation if, for example, the intermediate level is far detuned, such that a) the dynamics of the system is governed by the (slow) effective two-photon Rabi frequency $\Omega_{\text{eff}} = \Omega_{12}\Omega_{23}/2\Delta_1$ and b) the time scale of incoherent effects damping the atomic coherences is fast compared to the time evolution of the population, $\Gamma_{ij}, \gamma_{ij} \gg \Omega_{\text{eff}}$. Using Eq. (3.1) as well as the trace condition for the conservation of probability, $\text{Tr}[\rho] = \sum_i \rho_{ii} = 1$, one can solve Eq. (2.25) for $\dot\rho_{rr}$ and $\dot\rho_{mm}$. Approximating further $\dot\rho_{mm} - \dot\rho_{gg} \sim 0$, which is valid if the decay γ_{21} is large, and using once again the trace condition to rewrite this approximation as
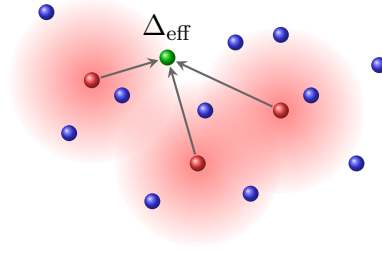
Figure 3.1: Illustration of the rate equation approach. Surrounding Rydberg atoms effectively shift the energy of the atom's Rydberg level, which is accounted for by a modified, effective detuning Δ_{eff}.

$2\dot{\rho}_{mm} + \dot{\rho}_{rr} \sim 0$, we finally obtain a rate equation for an effective two-level atom [35]

$$\partial_t \rho_{rr}(t) = \gamma_\uparrow \rho_{gg}^{\text{eff}}(t) - \gamma_\downarrow \rho_{rr}(t), \tag{3.2}$$

where we introduced an effective ground state population ρ_{gg}^{eff} as well as the (de-)excitation rates $\gamma_\downarrow$ and $\gamma_\uparrow$, respectively. The rates $\gamma_\downarrow$, $\gamma_\uparrow$ are analytical functions of the master equation's parameters.

Using the approximations discussed above, the density matrix simplifies to a matrix containing the populations of the atoms only. For convenience, we let $\rho_{\alpha,r}$ denote the Rydberg population of atom α and $\rho_{\alpha,g}$ the population of the effective ground state.

The next important step is now to approximate the Rydberg-Rydberg interaction (2.30), neglecting two-photon processes $|gg\rangle \leftrightarrow |rr\rangle$. In essence, it is an approximation which allows us to include the energy shift induced by surrounding Rydberg atoms in the detuning of the individual atoms [35],

$$\Delta_{\text{eff}}^{(\alpha)} = \Delta^{(\alpha)} - \sum_{\beta \neq \alpha} \mathcal{V}_{rr}^{(\alpha,\beta)} \rho_{\beta,r}. \tag{3.3}$$

Neglecting two-photon processes is fully consistent with approximation (3.1) since the adiabatic elimination of single-atom coherences inhibits the direct transition $|gg\rangle \leftrightarrow |rr\rangle$, which requires two-atom correlations.

Two remarks are in order. First, the interaction and the detuning in Eq. (3.3) have different signs. This holds for a repulsive van der Waals interaction with $C_6 > 0$. For attractive interaction, the interaction-induced energy shift changes sign an hence negative detunings are required to observe the same qualitative dynamics as for repulsive interaction and positive detuning. Second, Eq. (3.3) allows us to generalize our effective two-level equation (3.2) to the interacting case without the need to abandon its convenient structure. An illustration of the procedure described in Eq. (3.3) is shown in Figure 3.1.

The time-dependent rate equation (3.2) can be most efficiently solved using kinetic Monte Carlo (kMC) technique [76, 77]. *Monte Carlo* typically denotes any kind of algorithm that involves (pseudo) random numbers, i.e., no deterministic simulation of the underlying equations is performed, but rather a stochastic one [78]. More specifically, by sampling many realizations of the system under consideration, a reliable estimate is obtained by averaging the various outcomes if the sample size is sufficiently large (cf. Section 4.2).

In essence, there are two kinds of Monte Carlo techniques involved in the numerical solution of the rate equation (3.2). First, the states of the atoms become discrete numbers, i.e., an atom is either excited or not, $\rho_{\alpha,i} \in \{0, 1\}$. There is no statistical mixture at this level. The correct excitation fraction of the respective configuration is obtained only by sampling many realizations of the system. This procedure is usually referred to as 'Monte Carlo sampling' as it represents a standard example of a Monte Carlo solution along the lines of the definition

given in the previous paragraph. Second, the time evolution is calculated using kinetic Monte Carlo technique.

In the many-body basis $B = \{(i_1, \ldots, i_N)^T \,|\, i \in \{g, r\}\}$, we can rewrite the rate equation (3.2) as [77]

$$\frac{d\sigma_\ell}{dt} = \sum_{\ell'} (\Gamma_{\ell\ell'}\sigma_{\ell'} - \Gamma_{\ell'\ell}\sigma_\ell), \tag{3.4}$$

with $\sigma_\ell \in B$ denoting the probability for configuration ℓ, $\Gamma_{\ell\ell'}$ the respective excitation rates to the many-body state σ_ℓ and $\Gamma_{\ell'\ell}$ the respective de-excitation rates from the many-body state σ_ℓ. Since the master equation is a loss-gain equation, $\Gamma_{\ell\ell} = 0$ by definition (in the von Neumann equation, the commutator takes care of this). Defining the matrices $(\boldsymbol{U})_{\ell\ell'} = \Gamma_{\ell\ell'}$, $(\boldsymbol{D})_{\ell\ell'} = \sum_{\tilde{\ell}} \Gamma_{\tilde{\ell}\ell'}$ for $\ell = \ell'$ and zero otherwise, Eq. (3.4) is readily written in matrix notation as

$$\frac{d\boldsymbol{\sigma}}{dt} = -(\boldsymbol{D} - \boldsymbol{U})\boldsymbol{\sigma}. \tag{3.5}$$

By means of the matrix $\boldsymbol{S}(t) = \exp[-\boldsymbol{D}t]$ we can determine the probability that a system being initially in the configuration ℓ is at time t still in configuration ℓ:

$$p_\ell(t) = (\boldsymbol{S})_{\ell\ell}(t) = \exp[-(\boldsymbol{D})_{\ell\ell}t]. \tag{3.6}$$

Hence, the time of the first reaction is given by $p_{\bar{\ell}}(t) = 1 - p_\ell(t)$, which has the probability distribution $\partial_t p_{\bar{\ell}} = (\boldsymbol{D})_{\ell\ell} \exp[-(\boldsymbol{D})_{\ell\ell}t]$. The normalization is easily checked by integrating the distribution from 0 to t.

We can thus draw the time of the first change of the system by solving $p_{\bar{\ell}} = r$, where r is a uniform random number on the unit interval [77], which gives simply $\exp[-(\boldsymbol{D})_{\ell\ell}t] = r$, or, solved for t,

$$t = -\ln[r]/(\boldsymbol{D})_{\ell\ell}. \tag{3.7}$$

In our simulation, the system is always in a certain state σ_ℓ, as a consequence of the Monte Carlo approach. Accordingly, the total rate $\gamma_{\updownarrow\text{tot}}$ by which the system changes its state can, with respect to our rate equation (3.2), be obtained by adding $\gamma_\downarrow^{(\alpha)}$ if atom α is excited and $\gamma_\uparrow^{(\alpha)}$ otherwise to the total rate $\gamma_{\updownarrow\text{tot}}$. The time for the next change of the system is then calculated via $t = -\ln[r]/\gamma_{\updownarrow\text{tot}}$.

We have now everything required to solve the many-body version of Eq. (3.2) by means of the kinetic Monte Carlo algorithm, which is summarized in Algorithm 1. After one run of Algorithm 1, we obtain a certain realization of the system, which does not capture the full available configuration space. In practice, we need to embed Algorithm 1 in some loop which ensures that enough simulations are performed to sample a representative part of the system's configuration space. The number of simulations that are required depends on the observables and the geometry; for "typical" parameters, several thousand simulations suffice to produce reasonable data for the Rydberg population. Observables are calculated subsequent to Algorithm 1. By design, the kMC algorithm does not allow for calculating time resolved observables[6], but it allows one to compute observables measured at a certain (end-)time by following the dynamics of the system.

---

[6]Admittedly, one can devise a way to compute the time evolution by considering only configurations of the system at times that match the given time interval, but this comes at the expense of an increased number of total simulations to ensure reasonable statistics for all time intervals.

Algorithm 1: Kinetic Monte Carlo algorithm for the rate equation

---

Place the atoms (randomly) in the trap
Set all atoms to the ground state
while $t \leq t_{\text{end}}$ **do**
  for $\alpha \leq N$ **do**
    Calculate Δ_{eff} based on the current configuration
    if *Atom α is excited* **then**
      Calculate $\gamma_{\downarrow}^{(\alpha)}$
    else
      Calculate $\gamma_{\uparrow}^{(\alpha)}$
    Add rate to $\gamma_{\updownarrow\text{tot}}$
  Draw random numbers $r_1, r_2 \in [0, 1)$
  Determine $\delta t = -\ln[r_1]/\gamma_{\updownarrow\text{tot}}$, update time
  Determine atom β that changes its state via $\sum_{\alpha=1}^{\beta-1} \gamma_{\downarrow,\uparrow}^{(\alpha)} \leq r_2 \, \gamma_{\updownarrow\text{tot}} < \sum_{\alpha=1}^{\beta} \gamma_{\downarrow,\uparrow}^{(\alpha)}$
  Change state of atom β

The rate equation model is applicable as long as many-body-coherence effects such as two-photon excitations $|gg\rangle \leftrightarrow |rr\rangle$ are negligible and thus inter-atomic coherences do not play a significant role in the system's dynamics.

Moreover, the dynamics of the system can only be calculated reliably if the reduction to an effective two-level scheme (as performed above) is possible. In the full three-level case, non-physical negative rates frequently occur [36]. By modifying the rates in a way that ensures that the respective steady state is still reached, positive rates can be obtained [79], however, this cumbersome technique is usually impractical for general systems [55].

Consequently, another approach has been developed in Refs. [36, 55] to circumvent this problem. There, the calculation of the dynamics of the system was abandoned in favor of the steady-state calculation. In particular, the calculation of a three-level single-atom steady state was optimized and the global steady state of the system was determined via Monte Carlo sampling. That is, after initialization, the atom that is supposed to change its state is randomly picked and its steady state is calculated taking into account the current realization of the system via the effective detuning Δ_{eff} as above. Then, using a random number, it is determined whether the atom changes its state or not, by comparing the random number with the steady-state populations of the single-atom levels (linear search algorithm as in Algorithm 1). The same procedure is repeated several times until the global steady state is reached (which is usually the case after a few N steps [36]).

In conclusion, rate equation models allow to efficiently simulate interacting many-body Rydberg systems in the strong dissipative regime where inter-atomic coherences as well as multi-photon processes are negligible. Realistic systems consisting of several thousand atoms can be simulated and even the steady-state properties of EIT systems can be analyzed [17, 80].

3.2 Wave Function Monte Carlo Technique

The wave function Monte Carlo (MCWF) technique [41–44] is a numerical simulation technique which allows one to solve the many-body master equation (2.32) without employing the density matrix formalism. Accordingly, the problem of the quadratic scaling of the number of density matrix elements with respect to the number of many-body states can be avoided without

giving up the ability to account for incoherent processes.

In short, the MCWF technique is based on an analytical equivalence between the master equation (2.32) and the average of quantum wave function trajectories that are obtained using non-hermitian time evolution combined with additional random quantum jumps [44]. In other words, instead of a deterministic evolution of the density matrix, a piecewise deterministic process of the wave function is employed, which is sometimes called the *unraveling* of the master equation [62]. The periods of deterministic evolution are interrupted by discontinuous jumps of the wave function that, in a statistical average, reproduce the deterministic time evolution of the density matrix.

More precisely, the many-body Hamiltonian (2.29) governing the coherent time evolution is replaced by a non-hermitian Hamiltonian including the anti-commutator part of the Lindblad term (2.22) in Eq. (2.32),

$$\mathcal{H}_{\mathrm{nh}} = \mathcal{H} - \frac{i}{2}(\gamma + \Gamma) \sum_{\alpha=1}^{N} |r_\alpha\rangle \langle r_\alpha| \equiv \mathcal{H} - \frac{i}{2} \sum_{\alpha=1}^{N} \left(\mathcal{C}_\Gamma^{(\alpha)\,\dagger} \mathcal{C}_\Gamma^{(\alpha)} + \mathcal{C}_\gamma^{(\alpha)\,\dagger} \mathcal{C}_\gamma^{(\alpha)} \right). \tag{3.8}$$

Here, we have again made use of the jump operators associated with dephasing and decay, respectively, i.e.,

$$\mathcal{C}_\Gamma^{(\alpha)} = \sqrt{\Gamma} |r_\alpha\rangle \langle r_\alpha|, \quad \mathcal{C}_\gamma^{(\alpha)} = \sqrt{\gamma} |g_\alpha\rangle \langle r_\alpha|. \tag{3.9}$$

For an infinitesimal time step δt, the time evolution of the many-body wave function $|\psi(t)\rangle$ is given by

$$|\psi'(t + \delta t)\rangle = (1 - i\mathcal{H}_{\mathrm{nh}}\delta t) |\psi(t)\rangle, \tag{3.10}$$

which is simply the expansion of the time translation operator $\exp[-i\mathcal{H}_{\mathrm{nh}}\delta t]$ to first order in δt. The time evolution given by a non-hermitian Hamiltonian does not preserve the norm of the wave function since the time translation operator is no longer unitary,

$$\begin{aligned}
\langle\psi'(t + \delta t)|\psi'(t + \delta t)\rangle &= \langle\psi(t)| \left(1 + i\mathcal{H}_{\mathrm{nh}}^{\dagger}\delta t\right)\left(1 - i\mathcal{H}_{\mathrm{nh}}\delta t\right) |\psi(t)\rangle \\
&= 1 - i\delta t \langle\psi(t)| \left(\mathcal{H}_{\mathrm{nh}} - \mathcal{H}_{\mathrm{nh}}^{\dagger}\right) |\psi(t)\rangle \\
&= 1 - \delta t \langle\psi(t)| \sum_{\alpha=1}^{N} \left(\mathcal{C}_\Gamma^{(\alpha)\,\dagger} \mathcal{C}_\Gamma^{(\alpha)} + \mathcal{C}_\gamma^{(\alpha)\,\dagger} \mathcal{C}_\gamma^{(\alpha)} \right) |\psi(t)\rangle \\
&\equiv 1 - \delta p, \tag{3.11}
\end{aligned}$$

where we dropped all terms of order δt^2 and assumed that the wave function is normalized at time t, $\langle\psi(t)|\psi(t)\rangle = 1$. This is why we introduced the prime $'$ in Eq. (3.11): it indicates that the wave function is not normalized. Additionally, we have introduced the *jump probability*

$$\delta p = \sum_{\alpha, F} \delta p_{\alpha, F} \quad \text{with} \quad \delta p_{\alpha, F} = \langle\psi(t)| \mathcal{C}_F^{(\alpha)\,\dagger} \mathcal{C}_F^{(\alpha)} |\psi(t)\rangle \delta t \tag{3.12}$$

and $F \in \{\gamma, \Gamma\}$. The association of δp with a quantum jump becomes obvious when considering Eq. (3.12): The operators $\mathcal{C}_F^{(\alpha)}$ collapse the wave function (thus the term *quantum jump*) and perform so to speak (at least for our choice of operators) a measurement, called a *gedanken measurement* in [44], on the wave function. As $\mathcal{C}_F^{(\alpha)\,\dagger} \mathcal{C}_F^{(\alpha)}$ is hermitian, the jump probability is always ≥ 0. However, in order for the first-order-in-time-approximation to be valid, we need to adjust δt such that $\delta p \ll 1$.

Stochastically speaking, the wave function undergoes in a given interval δt either a non-

---

Algorithm 2: Wave function Monte Carlo algorithm

Place the atoms (randomly) in the trap
for *many times* **do**
    Initialize the system in the ground state
    while $t \leq t_{\text{end}}$ **do**
        Calculate the jump probability δp
        Draw a random number $r_1 \in [0,1)$
        if $\delta p < r_1$ **then**
            Calculate the non-hermitian time evolution $\exp[-i\mathcal{H}_{\text{nh}}\delta t] |\psi(t)\rangle$
        else
            Draw a random number $r_2 \in [0,1)$
            Determine the jump $\tilde{\ell}$ via $\sum_{\ell=1}^{\tilde{\ell}-1} \delta p_\ell \leq r_2\, \delta p < \sum_{\ell=1}^{\tilde{\ell}} \delta p_\ell$
            Collapse the wave function using $\mathcal{C}_F^{(\alpha)}$ with $\{\alpha, F\} \iff \tilde{\ell}$ (i.e., atom α decays/dephases)
        Normalize the wave function
        Update the time $t \to t + \delta t$

Average over the quantum trajectories

---

hermitian time evolution with probability $1 - \delta p$ (3.11) or a certain quantum jump associated with the operator $\mathcal{C}_F^{(\alpha)}$ with probability $\delta p_{\alpha,F}$.

Putting these two observations together and ensuring the physical interpretation of the wave function by correct normalization (cf. Eqs. (3.11), (3.12)), we can write down the equation for the respective density matrix $\rho(t + \delta t) = |\psi(t + \delta t)\rangle \langle\psi(t + \delta t)|$ averaged over the various possible outcomes at time $t + \delta t$:

$$\overline{\rho(t + \delta t)} = (1 - \delta p)\frac{|\psi'(t + \delta t)\rangle}{\sqrt{1 - \delta p}}\frac{\langle\psi'(t + \delta t)|}{\sqrt{1 - \delta p}} + \sum_{\alpha,F} \delta p_{\alpha,F} \frac{\mathcal{C}_F^{(\alpha)} |\psi(t)\rangle}{\sqrt{\delta p_{\alpha,F}/\delta t}}\frac{\langle\psi(t)| \mathcal{C}_F^{(\alpha)\,\dagger}}{\sqrt{\delta p_{\alpha,F}/\delta t}}. \quad (3.13)$$

Simplifying this equation and plugging in the definitions (3.9), (3.10) yields, using $\rho(t) = |\psi(t)\rangle \langle\psi(t)|$,

$$\overline{\rho(t + \delta t)} = \rho(t) - i\delta t[\mathcal{H}, \rho(t)]$$
$$+ \sum_{\alpha,F} \left(-\frac{1}{2}\mathcal{C}_F^{(\alpha)\,\dagger}\mathcal{C}_F^{(\alpha)}\rho(t) - \frac{1}{2}\rho(t)\mathcal{C}_F^{(\alpha)\,\dagger}\mathcal{C}_F^{(\alpha)} + \mathcal{C}_F^{(\alpha)}\rho(t)\mathcal{C}_F^{(\alpha)\,\dagger} \right)\delta t. \quad (3.14)$$

For a small time step δt, this is simply the master equation with the time derivative written as a difference quotient,

$$\partial_t\overline{\rho(t)} = (\overline{\rho(t + \delta t)} - \overline{\rho(t)})/\delta t = -i[\mathcal{H}, \overline{\rho(t)}] + \sum_{\alpha,F} \mathcal{L}\left(\mathcal{C}_F^{(\alpha)}\right)[\overline{\rho(t)}], \quad (3.15)$$

where we averaged over the density matrix at time t as well. If the initial conditions of master equation and the above approach coincide, the exact density matrix and the one obtained by averaging, Eq. (3.15), coincide as well, at any time t [44].

There is, however, a caveat concerning the approximation performed in Eq. (3.10). Although there are no explicit constraints on the time step δt so far (except for the condition $\delta p \ll 1$ already mentioned), the first order approximation of the time evolution requires $\mathcal{H}_{\text{nh}}\delta t$ to be

small; in particular the eigenvalues of the Hamiltonian multiplied with the numerical time step, $|\lambda_m \delta t|$, need to be small compared to 1 [44]. This requirement is non-trivial for an interacting many-body system where the interaction energy depends on the atoms' spacings (cf. Section 4.2). The converse condition on δt, namely that δt needs to be larger than the correlation time of the reservoir [44], is typically not an issue in numerical simulations of Rydberg systems for the parameter range considered in the later chapters.

From the viewpoint of numerical computation, the procedure described above is easily translated into an algorithm by realizing the stochasticity of the time evolution by means of random numbers. To ensure a clear notation, we define a one-to-one correspondence between every number ℓ and the tuple $\{\alpha, F\}$ with $\alpha \in \{1, \dots, N\}$ and $F \in \{\gamma, \Gamma\}$. With the help of this definition we can summarize the MCWF technique in an algorithm, Algorithm 2.

To sum up, the wave function Monte Carlo technique allows one to numerically solve the master equation without employing the density matrix formalism. Instead, an equation of Schrödinger type is solved; incoherent processes are included via non-hermitian time evolution and additional random quantum jumps. In each step of the time evolution the system can either undergo a coherent, non-hermitian time evolution or perform a quantum jump associated with incoherent processes such as dephasing or decay. Whether or not a jump occurs in a single time step is determined by a Monte Carlo method, which randomly selects the jumping atom as well as the jump operator according to the respective jump probability. Averaging many random trajectories allows us to obtain a 'mixed' state that solves the corresponding master equation.

4 Implementation and Characterization of the MCWF Technique

Since a thorough understanding of the MCWF technique is indispensable to simulating interacting many-body Rydberg systems for experimentally relevant parameters, we address the technical details of our MCWF simulations in this chapter.

In Section 4.1 we discuss details on the implementation of the MCWF technique, which was implemented in an existing code that allows one to solve the coherent many-body Schrödinger equation [23, 32, 33]. As state space truncation is applied in this code, the projection operators for the MCWF model need to be adjusted to ensure correct simulation results.

Subsequently, we analyze the MCWF technique with respect to accuracy and convergence (Section 4.2) as well as to the robustness of the pair correlation function against variations of the numerical blockade radius (Section 4.3). In particular, we review the convergence properties of a general Monte Carlo procedure and discuss different instances that might decrease or increase the rate of convergence of the signal-to-noise ratio, which is the actually important quantity in our simulations. As expected from theory, we find that the MCWF calculation converges to the master equation result with increasing sample size. It turns out, though, that the finite size of the numerical time step required in the MCWF algorithm introduces a small error in the strongly interacting and far-detuned regime, due to the breakdown of the first-order approximation of the non-hermitian time evolution. The numerical blockade radius, in contrast, causes strong deviations of the pair correlation function only if varied considerably.

Moreover, the averaging procedure (Section 4.4) and the computational efficiency (Section 4.5) is examined. Considering observables consisting of individually averaged quantities[7], it turns out to be favorable to increase the number of simulated geometries rather than the number of trajectories simulated for each geometrical realization to obtain an accurate result most rapidly. The efficiency of our simulation is found to depend crucially on the number of matrix-vector multiplications performed in the simulation, which constitute the bottleneck of our simulation in terms of CPU time.

With these results, we can then turn to the discussion of simulation results of physically more relevant systems in Chapter 5.

Note that, in this as well as the following chapters, the units of the master equation parameters are dropped to improve readability. They can be easily restored, however, by consistently adding the unit MHz to the parameters Δ, Ω, γ, Γ and $\mathcal{V}_{rr}$, MHz μm^6 to the van der Waals coefficient C_6 and μm to any length/distance. The numerical time step δt is given in $2\pi\mu s$.

4.1 Details on the Implementation

Before discussing the technical details of the implementation of the wave function Monte Carlo technique, we need to first review the approach employed in [23, 32, 33] to tackle the problem of the exponentially growing Hilbert space, as it constitutes the starting point of our implementation of the MCWF technique.

In general, an established technique to deal with the exponential growth of the Hilbert space is state space truncation [22, 31, 32, 57], which essentially removes any state from the Hilbert space which cannot be populated due to the blockade effect. More specifically, considering the

---

[7]'Individually averaged' in this context means that these quantities can be calculated subsequent to both Monte Carlo and geometrical sampling (see below), such as the Rydberg population, for instance.
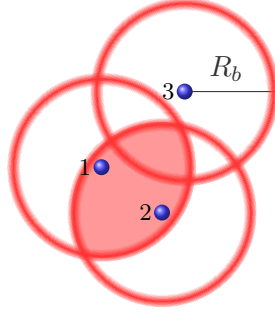
Figure 4.1: Illustration of the state space truncation procedure. States that cannot be populated due to the blockade effect (i.e., the doubly excited states in the reddish shaded area) are removed from the Hilbert space.

system shown in Figure 4.1, the state space truncation removes the states $|rrg\rangle$, $|rrr\rangle$ from the total many-body basis

$$\left\{ |\sigma_1\sigma_2\sigma_3\rangle \mid \sigma_1, \sigma_2, \sigma_3 \in \{g, r\} \right\}. \tag{4.1}$$

The truncation condition can either be given by setting a limit on the energy of the Rydberg states by hand or by estimating the cutoff energy C_6/R_b^{*6} using a numerical blockade radius $R_b^* < R_b$ with R_b denoting the estimated blockade radius that can be calculated, for instance, via Eq. (1.12). In our simulations, the latter procedure is used and the numerical blockade radius is adjusted so that no states with a relevant population contribution are removed, which can be checked for example by considering the pair correlation function that is introduced in Section 4.3. The linewidth broadening effect of the dephasing is factored in via the naïve replacement $\Omega \to \Omega + \Gamma$ in Eq. (1.12). For typical parameters such as the ones stated in Figure 4.4, the state space consists of $\mathcal{O}(10^3)$ states after truncation.

Details on the state space truncation (as well as state space construction) employed in [23, 32] can be found in Ref. [33]. For two-level systems, the state space truncation is extremely helpful since it allows one to significantly increase the number of atoms that can be simulated (for strong blockade and hence few excitations, $N > 100$ is possible). For three-level systems, however, the state space truncation is rendered inefficient as only interacting Rydberg states can be eliminated, leaving the number of intermediate states unaltered.

Consequently, our implementation of the wave function Monte Carlo technique has to take into account the modified Hilbert space underlying the simulation, induced by state space truncation, which particularly affects the many-body projection operators introduced in Section 3.2. That is, the many-body projection operator $\mathcal{C}_F^{(\alpha)}$ defined in Eq. (3.9) needs to set all many-body wave function amplitudes to zero which do not correspond to any excited state (for $F = \Gamma$) or ground state with existing excited state (for $F = \gamma$) of atom α. For $F = \Gamma$, the wave function amplitude is multiplied by $\sqrt{\Gamma}$ and stays in the excited (many-body) states of atom α, for $F = \gamma$ the amplitude is multiplied with $\sqrt{\gamma}$ and transfered to the respective ground states of atom α (cf. Eqs. (4.10), (4.11) for a two-atom example). If, due to the state space truncation, the excited states corresponding to certain ground states do not exist, the jump operator of both decay and dephasing needs to set the amplitudes of the respective ground states to zero nonetheless, since it is assumed that the amplitudes of the excited states are negligible, and that any transfer or mere multiplication with $\sqrt{F}$ will not change the simulation result. This modification is the most important one when trying to apply the MCWF technique detailed in [44] to Rydberg systems, apart from the implementation details.

In our three-atom example from above, for instance, the jump operator $\mathcal{C}_\Gamma^{(1)}$ projects the amplitudes of the states $|grg\rangle$, $|grr\rangle$ to zero although the corresponding excited states $|rrg\rangle$,

$|rrr\rangle$ do not exist, since we know that only a tiny error is introduced by neglecting the states $|rrg\rangle$, $|rrr\rangle$. $\mathcal{C}_\gamma^{(1)}$ conversely projects the amplitudes of the states $|grg\rangle$, $|grr\rangle$ to zero since the corresponding excited states $|rrg\rangle$, $|rrr\rangle$ do not exist and hence zero population is transferred from the excited states. This can be directly seen by applying the jump operator $\mathcal{C}_\gamma^{(1)} = \sqrt{\gamma}\, |g_1\rangle \langle r_1|$ to the wave function

$$|\psi\rangle = c_{ggg}\,|ggg\rangle + c_{rgg}\,|rgg\rangle + c_{grg}\,|grg\rangle + c_{ggr}\,|ggr\rangle + c_{rgr}\,|rgr\rangle + c_{grr}\,|grr\rangle, \tag{4.2}$$

yielding only two nonzero amplitudes,

$$\mathcal{C}_\gamma^{(1)}\,|\psi\rangle = \sqrt{\gamma}\,(c_{rgg}\,|ggg\rangle + c_{rgr}\,|ggr\rangle). \tag{4.3}$$

To determine the respective ground states of our many-body Hilbert space, a routine, which we call "calculation of jump connection array", is implemented. The routine loops over each excited state with m excitations and determines the states that are coupled to it by means of the many-body Hamiltonian[8], satisfying $m' = m - 1$ with m' being the excitations of the coupled state. With this in mind, the jump operators can be implemented according to the aforementioned instruction.

Apart from this caveat, Algorithm 2 can be implemented in a straightforward manner. Considering that the GSL routines available to solve ordinary differential equations treat real and imaginary part separately, the non-hermitian modification to the coherent Hamiltonian has to be split into two parts that act on the real and imaginary part of the many-body wave function. Denoting the real part of the wave function by $|\psi_\Re\rangle$, the imaginary part by $|\psi_\Im\rangle$ and the imaginary part of the Hamiltonian by $\mathcal{H}_\Im \equiv -i(\mathcal{H}_{\mathrm{nh}} - \mathcal{H})$ (cf. Eq. (3.8)), the modified Schrödinger equation reads

$$\partial_t(|\psi_\Re\rangle + i\,|\psi_\Im\rangle) = (\mathcal{H}_\Re\,|\psi_\Im\rangle - i\mathcal{H}_\Re\,|\psi_\Re\rangle) + (\mathcal{H}_\Im\,|\psi_\Re\rangle + i\mathcal{H}_\Im\,|\psi_\Im\rangle). \tag{4.4}$$

4.2 Accuracy and Convergence

Aiming to study the accuracy and convergence properties of the wave function Monte Carlo method, we start off by reviewing some statistics related to Monte Carlo procedures in general, i.e., the *law of large numbers* (LLN) and the *central limit theorem* (CLT).

Let $\bar{X}_n$ denote the arithmetic mean of a sequence of independent, identically distributed (i.i.d.) random variables X_i $(i = 1, \ldots, n)$ with expectation value μ each. Then, the *law of large numbers* states that

$$\lim_{n\to\infty} \bar{X}_n = \mu, \tag{4.5}$$

even if the variance σ^2 is not bounded from above [81]. Eq. (4.5) is the essence of the two formulations of the LLN, i.e., the weak and a strong one. Whereas the weak formulation asserts the convergence of $\bar{X}_n$ to μ while leaving open the possibility for a large deviation $|\bar{X}_n - \mu|$ to occur an arbitrary number of times (but very infrequently, of course) as n increases, the strong formulation ensures that such deviations cannot happen arbitrarily often [81]. The LLN thus guarantees convergence to the true mean without giving any information on the rate of convergence or the error. For this, we need the central limit theorem.

The *central limit theorem* states that if the variance is bounded from above, $\sigma^2 < \infty$, the

---

[8]Strictly speaking, only the lower triangular part of the Hamiltonian is required for this procedure.

probability P satisfies

$$\lim_{n \to \infty} \mathrm{P}\left(\frac{|\bar{X}_n - \mu|}{\sigma/\sqrt{n}} \leq \lambda\right) = \frac{1}{\sqrt{2\pi}} \int_{-\lambda}^{\lambda} e^{-x^2/2}\, dx \tag{4.6}$$

for the random variable X_i introduced above. In other words, the X_i are asymptotically distributed with mean μ and standard deviation $\sigma/\sqrt{n}$ [81]. Accordingly, the error of our estimate $\bar{X}_n$ decreases with $1/\sqrt{n}$ for standard Monte Carlo sampling. By replacing the 'true' variance $\sigma^2 = \sum_i (X_i - \mu)^2$ by the estimated one, one can in principle specify a confidence interval for the estimate $\bar{X}_n$ via Eq. (4.6).

Although the Monte Carlo sampling technique has a rather poor convergence rate of $1/\sqrt{n}$ compared to direct numerical integration schemes which solve ordinary differential equations, for example, it is an extremely flexible method which can be applied to highly complex and multidimensional problems without altering the convergence properties.

As a side note, a false understanding of the law of large numbers can lead to the *gambler's fallacy* by which a gambler might reason that if a fair coin was tossed ten times with eight occurrences of "tail", the probability for "head" in subsequent tosses would be larger than one half to even out the excess of "tails" [81].

Analysis of Convergence With Respect To Sample Size

Relating Eq. (4.6) to the wave function Monte Carlo technique, we expect a $1/\sqrt{n}$ scaling of the population error with respect to the number of simulations n. To quantify this scaling, we introduce the effective, time-averaged variance

$$\sigma_t^2 = \frac{1}{N} \sum_{\nu=1}^{N} \left(\langle \mathcal{N}(t_\nu)\rangle_{\mathrm{ME}} - \overline{\langle \mathcal{N}(t_\nu)\rangle}\right)^2, \tag{4.7}$$
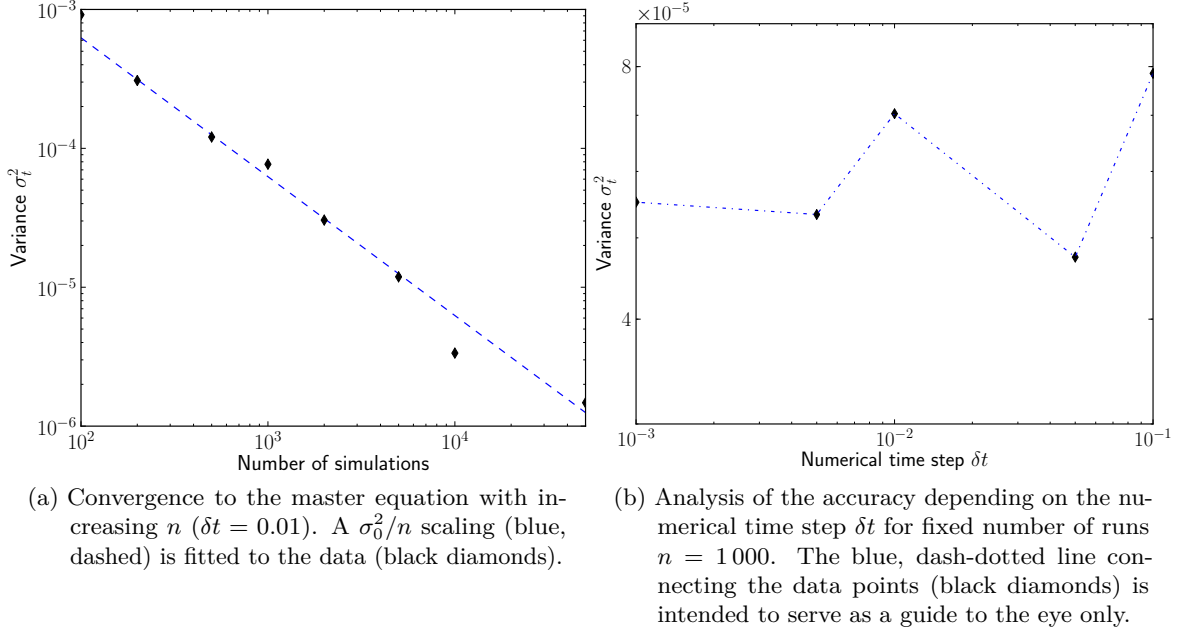
where ME abbreviates the master equation solution, t_ν denotes the discrete evaluation times and the measurement operator for the total Rydberg population is defined as

$$\mathcal{N} = \sum_\alpha \mathcal{N}^{(\alpha)} \quad \text{with} \quad \mathcal{N}^{(\alpha)} = |r_\alpha\rangle\langle r_\alpha|. \tag{4.8}$$

Plotting the variance (4.7) over the number of Monte Carlo simulations, we obtain a scaling compatible with the expected $1/\sqrt{n}$ scaling (cf. Figure 4.2a).

Note that, to compare the accuracy of different simulation results, one should use a relative error estimate like the signal-to-noise ratio μ/σ rather than the simple variance σ_t^2. For this ratio, the condition for good statistics is crucially dependent on the observable that is to be evaluated [44]. For an observable to which many states contribute, called global operator in Ref. [44], less statistics is required to obtain a good signal-to-noise ratio than for a local operator which acts on a single state only. As the Rydberg population operator $\mathcal{N}$ is a global operator, the number of Monte Carlo runs required for good statistics decreases as we simulate a system consisting of many atoms.

Moreover, from the full time-averaged variance shown in Figure 4.2a we cannot deduce an error estimate for the population $\langle \mathcal{N}(t_\nu)\rangle$ as the standard deviation $\sigma(t_\nu)$ is not uniform. More precisely, the variance depends both on the jump rate and the effect of the quantum jump. At the beginning of the simulation, the jump rate is negligible, leading to a small variance which is approximately independent of the number of Monte Carlo runs. This adds another explanation for the deviations in the fit in Figure 4.2a. As soon as the jump probability becomes clearly nonzero, quantum jumps can occur, projecting the system onto a distinct

(a) Convergence to the master equation with increasing n ($\delta t = 0.01$). A σ_0^2/n scaling (blue, dashed) is fitted to the data (black diamonds).

(b) Analysis of the accuracy depending on the numerical time step δt for fixed number of runs $n = 1\,000$. The blue, dash-dotted line connecting the data points (black diamonds) is intended to serve as a guide to the eye only.

Figure 4.2: Accuracy of the MCWF simulation for two atoms (quantified by the variance σ_t^2, cf. text). Parameters: $\Omega/2\pi = 1$, $\Delta/2\pi = 5$, $\mathcal{V}_{rr}/2\pi = 10$, $\gamma/2\pi = 0.5$ and $\Gamma/2\pi = 0.5$.

quantum state. To illustrate the effect of dephasing and decay on the wave function, let us consider for simplicity a two-atom system, whose wave function can be written as

$$|\psi\rangle = c_{gg}\,|gg\rangle + c_{rg}\,|rg\rangle + c_{gr}\,|gr\rangle + c_{rr}\,|rr\rangle\,. \tag{4.9}$$

If atom 2 decays by emitting a photon, the wave function becomes

$$|\psi_{\gamma,2}\rangle = \frac{c_{gr}\,|gg\rangle + c_{rr}\,|rg\rangle}{\sqrt{|c_{gr}|^2 + |c_{rr}|^2}}\,. \tag{4.10}$$

In the case of dephasing, we rather have

$$|\psi_{\Gamma,2}\rangle = \frac{c_{gr}\,|gr\rangle + c_{rr}\,|rr\rangle}{\sqrt{|c_{gr}|^2 + |c_{rr}|^2}}\,. \tag{4.11}$$

Accordingly, the total jump probability decreases after a decay if the amplitude c_{rr} for double excitation is almost vanishing, $|c_{rr}|^2 \ll |c_{rg}|^2, |c_{gr}|^2$. Conversely, if $|c_{rr}|^2$ is comparable to $|c_{rg}|^2, |c_{gr}|^2$, the jump probability for atom 1 increases and collective jumps become likely [47]. For dephasing, in contrast, the jump probability always increases unless the amplitudes c_{gg}, c_{rg} are negligible; in that case, the probability stays the same as the dephasing jump does not alter the wave function. If no jumps occur for some time, the system is, via the non-hermitian time evolution, evolved into the ground state again, reducing the jump probability.

In the presence of a large detuning, the Rydberg population is usually small, implying that a dephasing jump can have a significant impact on the wave function. This is shown in Figure 4.3a: For zero detuning, the doubly excited state is essentially blockaded and the population is bounded by one. For $\Delta = \mathcal{V}_{rr}/2$, resonant double excitation is possible, leading to an enhanced fluctuation. Accordingly, the variance is larger for positive detunings, requiring more statistics to obtain a smooth curve. This is an observation somewhat equivalent to the one elaborated in Ref. [44]. There, it was noted that the sample variance depends on the

(a) Single quantum trajectories for $\Delta = 0$ (blue curve) and $\Delta/2\pi = 5$ (solid and dashed red curves).

(b) Time evolution of the Rydberg population depending on the interaction median $\tilde{\mathcal{V}}_{rr}^{(\alpha,\beta)}/2\pi \approx 5, 100, 4\,500$ for the red, blue and green curve, respectively, from top to bottom.
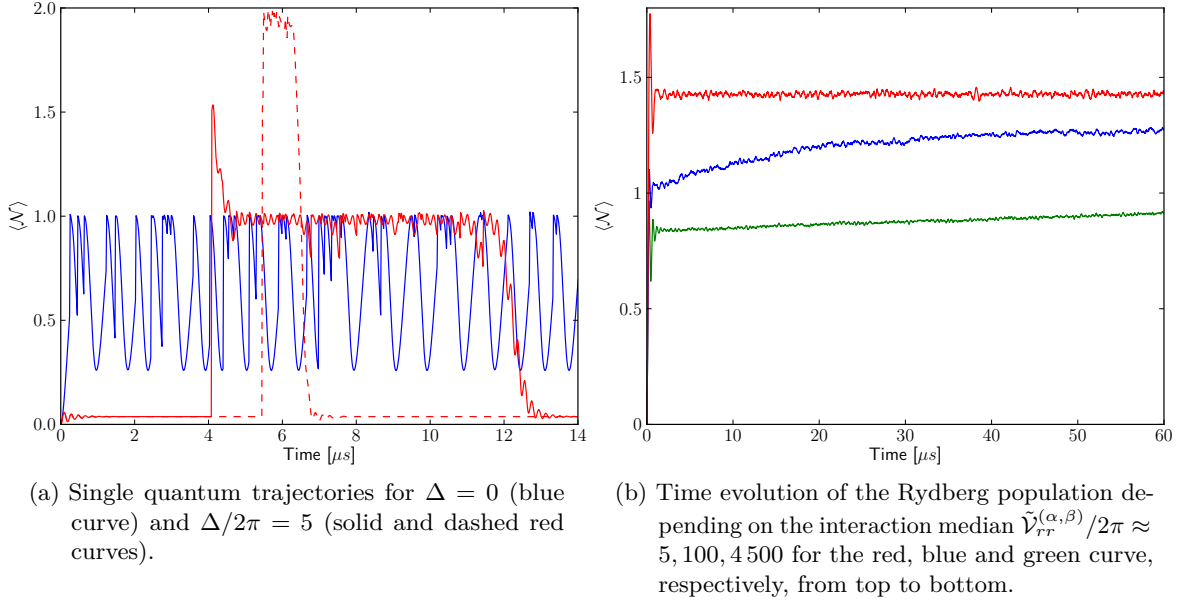
Figure 4.3: Impact of detuning and interaction on the Rydberg population. Parameters: (a) $N = 2$, $\mathcal{V}_{rr}/2\pi = 10$. (b) $N = 5$, $\Delta = 0$, $n = 2\,000$. Common parameters: $\Omega/2\pi = 1$, $\Gamma/2\pi = 1$, $\gamma = 0$, $\delta t = 0.01$.

particular jump operator used for measurement, which was chosen from a class of operators that yield the same master equation. For an operator that projects onto an eigenstate of the system, an enhanced variance was observed compared to an operator which projects onto a superposition. As the dephasing jump operator projects onto an eigenstate of the system, the fluctuation induced by this jump is particularly large for positive detunings, so more statistics (or a larger atom number) are required to obtain a good signal-to-noise ratio.

Analysis of the Numerical Time Step

In addition to the number of simulations, we have to examine yet another parameter and its impact on the accuracy of the wave function Monte Carlo simulation, namely the numerical time step δt introduced in Section 3.2. Constraining ourselves again to the two-atom case where we can compare the simulation results most easily with the exact master equation solution, we find for the parameters in Figure 4.2 no obvious scaling of the accuracy with the numerical step size (cf. Figure 4.2b). At first sight, this is not too surprising since the equivalence between the master equation and the MCWF approach does not depend on a particular value of δt [44]. Nevertheless, it is unclear whether the generalization of the simple two-atom system with easily tunable interaction strength to a many-body system with more versatile interactions affects our conclusion concerning the arbitrariness of the numerical time step δt. Indeed, for multiple atoms, we find a deviation in the Rydberg population depending on the numerical step size δt, which is shown in Figure 4.4.

To check whether this is an effect of the numerical time step δt only or of the violation of the condition $\delta p \ll 1$, we first observe that the total jump probability δp can be easily calculated from the total Rydberg population via $\delta p = (\gamma + \Gamma)\langle\mathcal{N}\rangle\delta t$. With respect to Figure 4.4, this implies that the condition $\delta p \ll 1$ is met for all numerical time steps δt. However, the condition $|\lambda_m \delta t| \ll 1$ with λ_m denoting the eigenvalues of the Hamiltonian $\mathcal{H}_{\mathrm{nh}}$ is more difficult to fulfill as we do not know the exact eigenvalues. Assuming weak driving ($\Omega \ll \Delta, \mathcal{V}_{rr}$), the
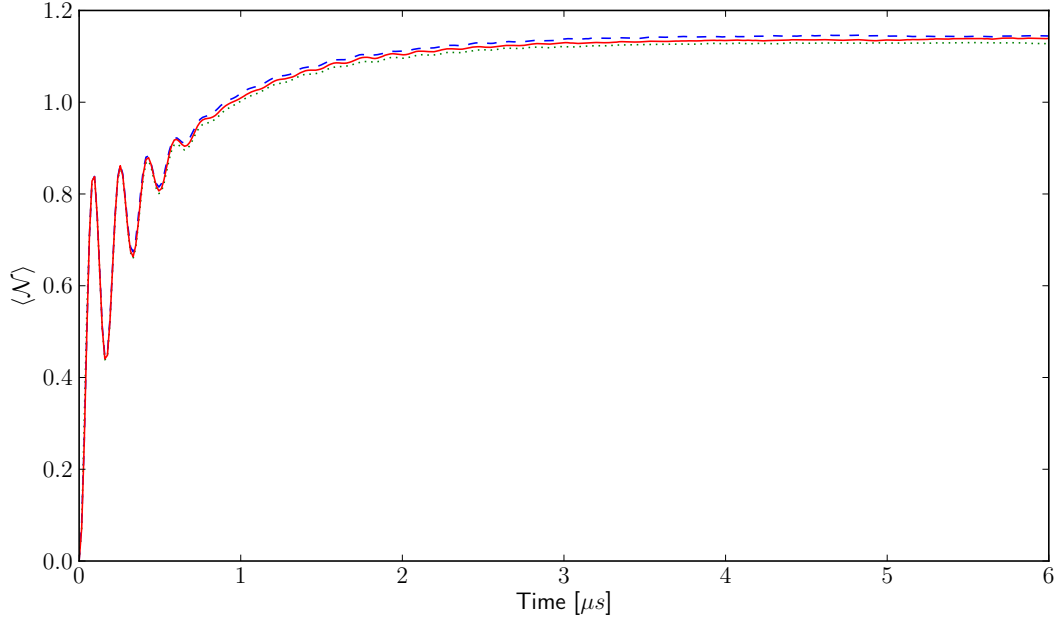
Figure 4.4: Analysis of the dependence of simulation results on the numerical time step δt: $\delta t = 0.02$ (green, dotted), $\delta t = 0.01$ (blue, dashed) and $\delta t = 0.001$ (red, solid). Parameters: $N = 30$, $L_{1D} = 10$, $\Omega/2\pi = 1$, $\Delta/2\pi = 5$, $C_6/2\pi = 900$, $\gamma/2\pi = 0.2$ and $\Gamma = 0$.

eigenvalues of the non-hermitian Hamiltonian are basically given by

$$\lambda_m \sim -m\left(\Delta + \frac{i}{2}(\gamma + \Gamma)\right) + \sum_{\alpha < \beta \in \boldsymbol{\sigma}_m} \mathcal{V}_{rr}^{(\alpha,\beta)}, \tag{4.12}$$

with $\boldsymbol{\sigma}_m$ denoting the many-body state restricted to m excitations, $\sum_\alpha \delta_{(\boldsymbol{\sigma}_m)_\alpha r} = m$. For any number m of excitations, the number of interaction terms is given by the binomial coefficient $\binom{m}{2}$.

At first sight, Eq. (4.12) looks as if the condition $|\lambda_m \delta t| \ll 1$ could not be fulfilled in general if the number of excitations is larger than, say, two, since $\mathcal{V}_{rr}^{(\alpha,\beta)}$ is unbounded. Nonetheless, we need to remind ourselves that state space truncation ensures that the sum of the interaction energies is bounded from above, and, what is more, that far detuned states do not contribute significantly to the simulation result. Accordingly, the error introduced by the numerical time step is expected to only affect the subspace of sparsely populated states, which should reduce the impact on the simulation result.

In fact, for the simulations shown in Figure 4.4 we have a relative deviation of $\lesssim 1\%$. For another simulation with slightly different parameters ($N = 35$, $L_{1D} = 15$, $\Omega/2\pi = 0.8$, $\Delta/2\pi = 5$, $C_6/2\pi = 16\,000$, $\gamma = 0.025$, $\Gamma/2\pi = 2$) we find a relative deviation of $\sim 2\%$ when comparing the steady-state values for $\delta t = 0.01$ and $\delta t = 0.002$. This suggests that the relative deviation introduced by the large eigenvalues of the Hamiltonian can be as large as a few percent for typical simulation parameters in the strongly interacting regime. It should be noted, however, that the relative deviation of 2% between the simulation results does not necessarily translate into a relative error of 2% as the two simulation results could correspond to upward and downward fluctuations, respectively (cf. Figure 4.4). Notwithstanding, the relative deviation strongly suggests that some non-vanishing error is introduced by choosing a computationally favorable, i.e., large numerical time step in a strongly interacting and far detuned regime.

We do not attribute this deviation to the lack of statistics with respect to geometrical averaging since a comparison of simulations with equal numerical time steps $\delta t = 0.02, 0.01$

and number of simulations $n_{\text{geo}} \times n \sim 10^3 \times 100$ yields a deviation $\lesssim 3\,\%_0$, which is one order of magnitude smaller than the deviation found by comparing different numerical step sizes. Thus, there is an inaccuracy arising from the numerical step size δt if the simulated system is strongly interacting and far detuned, which we have to tolerate if we want to avoid very computationally-expensive, time-consuming numerical simulations. Based on the relative deviation of the simulation results, we estimate this error to be in the order of few percent in a worst case scenario.

Another regime where the dipole interaction brings about a numerically challenging regime with respect to steady-state (SS) calculations is the regime with zero decay but nonzero dephasing. In this regime, the steady-state value of the population is reached extremely slowly, as shown in Figure 4.3b. This can be understood as follows: If the interaction potential between the atoms is large enough to significantly reduce the speed of the population transfer to the excited level, but still sufficiently small to not prevent a measurable population transfer, the population will reach its steady state only in the limit of large times. It is clear that an improper choice of the numerical time step δt entails a non-negligible population error in this regime where the sparsely populated subspace plays an important role.

In addition, the state space truncation criterion is, strictly speaking, invalidated in this regime since the blockade only applies dynamically for zero decay, i.e., for zero decay, the equally populated steady state of a strongly interacting system is only reached in the limit of 'infinite' times. In our simulations, however, we only consider finite times $t \lesssim 60\,\mu s$, so that the (dynamical) truncation still applies and thus also the static truncation. In a sense, a system with zero decay is unphysical, as in real physical systems there is a particular direction towards the energetic ground state of the system in the long-term dynamics. This tendency is only negligible for short-term dynamics for which the steady state of the system is never reached. For a detailed analysis of a two-atomic system with zero decay, see Section 5.6.

In the coherent case, the resulting stiffness[9] of the Hamiltonian is typically taken care of by an appropriate adaptive step size of the ODE solving routine (cf. Section 4.5). For the MCWF technique as detailed above, the step size needs to be fixed at the beginning, introducing a small error in the case of stiff ODEs, i.e., if $|\lambda_m \delta t| \ll 1$ is not fulfilled.

4.3 Numerical Blockade Radius

Besides the numerical parameters on which the MCWF technique explicitly depends, our simulation also relies on the state space truncation introduced in Section 3.2. To quantify its impact, it is convenient to introduce an new observable: the pair correlation function. In particular the blockade radius R_b, which affects the many-body dynamics as discussed in Section 1.3, is easily accessible via the pair correlation function.

The pair correlation function $G^{(2)}$ is defined as [36, 82]

$$G^{(2)}(R) = \frac{\sum_{\alpha<\beta} \langle \mathcal{N}^{(\alpha)} \mathcal{N}^{(\beta)} \rangle \delta_R^{(\alpha,\beta)}}{\left(\frac{1}{N}\langle \mathcal{N} \rangle\right)^2 \sum_{\alpha<\beta} \delta_R^{(\alpha,\beta)}}, \tag{4.13}$$

where $\delta_R^{(\alpha,\beta)}$ is 1 only if the two atoms α, β are separated by a distance which lies in the interval $R < |\boldsymbol{R}_\alpha - \boldsymbol{R}_\beta| < R + \Delta R$,

$$\delta_R^{(\alpha,\beta)} \equiv \left[\Theta\left(\frac{|\mathbf{R}_\alpha - \mathbf{R}_\beta| - R}{\Delta R}\right) - \Theta\left(\frac{|\mathbf{R}_\alpha - \mathbf{R}_\beta| - R}{\Delta R} - 1\right) \right], \tag{4.14}$$

---

[9]In computational language, an ordinary differential equation (ODE) is called *stiff* if the eigenvalues of its Jacobian matrix (in our case the Hamiltonian) have greatly differing magnitudes [78].

where $\Theta(x)$ is the Heaviside step function, $\Theta(x) = 1$ for $x > 0$ and $\Theta(x) = 0$ for $x < 0$. The pair correlation function defined in (4.13) quantifies the probability to find two excited atoms in a certain distance R. There is, however, a drawback in the definition of $G^{(2)}$, namely that it is not immune to finite-size effects. More specifically, the division by the total number of pairs with distance R takes into account the spatial distribution of the atoms, but not of the excitations.

To illustrate this, let us consider an atom positioned at the trap border. Following a simple mean-field argument, atoms positioned at the trap border are preferentially excited, since the total dipole interaction is reduced at the trap border as only atoms *inside* the trap contribute to it and hence the background field is smaller for border atoms. Thus, the excitation fraction is larger for atoms at the trap border, yielding an increase of $G^{(2)}(R)$ as R approaches the trap length. This increase is not what one would expect from a properly defined pair correlation function, because for a finite correlation length, atoms separated by large distances should not be correlated, $\langle \mathcal{N}^{(\alpha)}\mathcal{N}^{(\beta)}\rangle \simeq \langle \mathcal{N}^{(\alpha)}\rangle\langle \mathcal{N}^{(\beta)}\rangle$, and hence the correlation function should approach the constant value $G^{(2)} = 1$ for large R.

The drawback in the definition of $G^{(2)}(R)$ could be remedied by using a different definition [32], introducing the observable $g^{(2)}(R)$ via

$$g^{(2)}(R) = \left(\sum_{\alpha<\beta} \delta_R^{(\alpha,\beta)} \frac{\langle \mathcal{N}^{(\alpha)}\mathcal{N}^{(\beta)}\rangle}{\langle \mathcal{N}^{(\alpha)}\rangle\langle \mathcal{N}^{(\beta)}\rangle} \right) \Big/ \sum_{\alpha<\beta} \delta_R^{(\alpha,\beta)}. \tag{4.15}$$

Here, finite-size effects are divided out since $g^{(2)}$ explicitly respects the distribution of excitations via normalization by $\langle \mathcal{N}^{(\alpha)}\rangle\langle \mathcal{N}^{(\beta)}\rangle$. Eq. (4.15) provides a normalized measure of the conditional probability of finding an excitation at $\mathbf{R}_\beta$ if there is already an excitation at $\mathbf{R}_\alpha$, with $|\mathbf{R}_\alpha - \mathbf{R}_\beta| = R$ [32]. Besides the definition (4.15), there are also slightly different definitions like the one given in Ref. [3] where numerator and denominator are summed separately. In practice, the precise definition of $g^{(2)}$ is usually modified depending on how easily the quantities needed to calculate $g^{(2)}$ are experimentally accessible and how numerically stable $g^{(2)}$ can be calculated.

Though the pair correlation function $g^{(2)}$ is somewhat more advantageous than $G^{(2)}$, we use Eq. (4.13) in the following. The reason is that, due to a quantum jump (in particular a dephasing jump) during a MCWF simulation, the product of the single excitation probabilities can be much smaller than the doubly excited one, $\langle \mathcal{N}^{(\alpha)}\rangle\langle \mathcal{N}^{(\beta)}\rangle \ll \langle \mathcal{N}^{(\alpha)}\mathcal{N}^{(\beta)}\rangle$, which causes $g^{(2)}$ to diverge. In the averaging procedure, this divergence doesn't average out since the single quantum trajectory is weighted far too much by means of the quotient-taking. Hence, the calculation of $g^{(2)}$ requires averaging of the quantum trajectories prior to geometry averaging discussed in Section 4.4, both with good statistics. If we use the pair correlation function $G^{(2)}$ instead, the first condition (i.e., good statistics for the trajectory average) can be relaxed. Hence, we use $G^{(2)}$ in the following since it can be calculated from separately averaged quantities only. Note that we expect $G^{(2)}$ to prove more favorable as compared to $g^{(2)}$ in experiments with disordered gases that measure spatial correlations via excitation imaging techniques, since it requires less statistics to obtain meaningful data.

Although we have access to the time-dependent pair correlation function $G^{(2)}(R,t)$, it is for most purposes more expedient to show the pair correlation function in the steady state of the system if it is reached for typical simulation times. If it is, we perform a temporal average to improve statistics, calculating $\langle \overline{G^{(2)}(R,t)} \rangle_{t\in[t_s,t_{\text{end}}]}$ where t_s denotes the time where the system has reached its steady state. If not stated otherwise, it is this averaged $G^{(2)}$ function that is shown in the following.

By means of the definition (4.13) we can now plot the pair correlation function $G^{(2)}(R)$ for
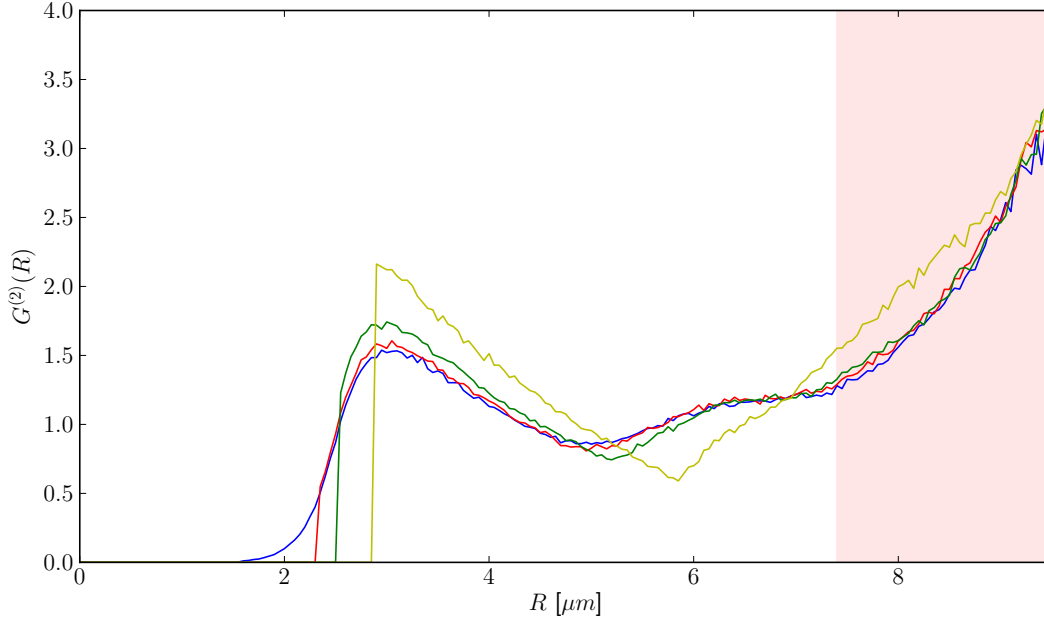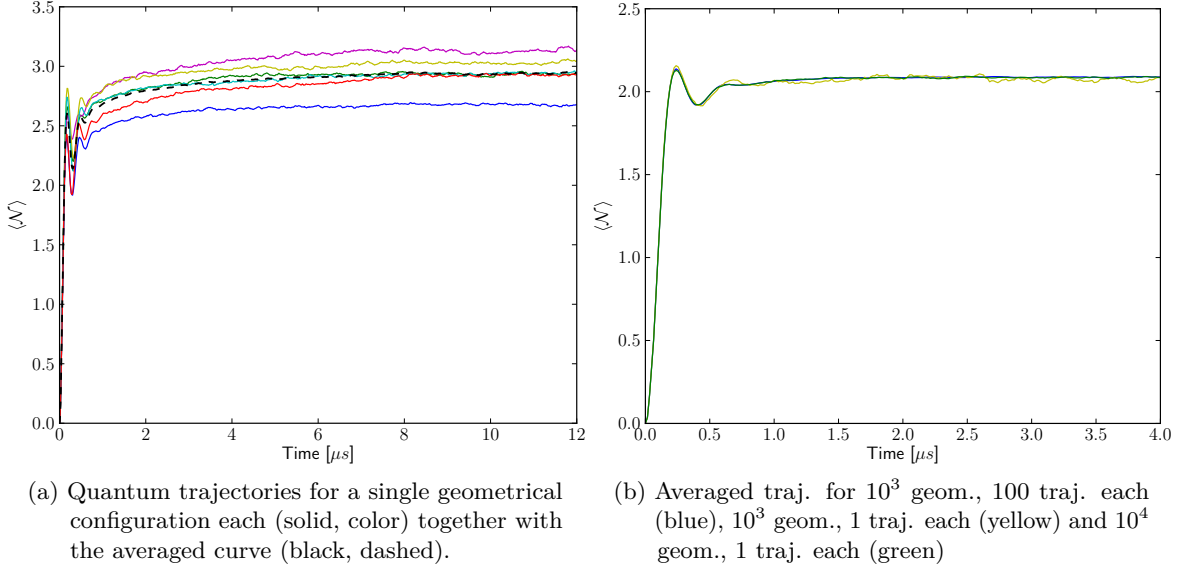
Figure 4.5: Analysis of $G^{(2)}(R)$ for different numerical blockade radii: $R_b^* = 0.68 R_b$ (blue), $R_b^* = R_b$ (red), $R_b^* = 1.1 R_b$ (green) and $R_b^* = 1.25 R_b$ (yellow), using an estimated $R_b = 2.35$ (cf. text). The reddish shaded area indicates dominance of finite-size effects. Parameters: $N = 30$, $L_{1D} = 10$, $\Omega/2\pi = 1$, $\Delta = 0$, $C_6/2\pi = 900$, $\gamma/2\pi = 0.1$, $\Gamma/2\pi = 1$, $n_{geo} = 1\,000$ and $\delta t = 0.02$.

several numerical blockade radii, which is done in Figure 4.5. There, the blockade radius R_b was estimated via Eq. (1.12) using the naïve replacement $\Omega \to \Omega + \Gamma$. For positive detuning, resonant processes can occur, as discussed in Sections 1.3 and 3.1. In that case, the estimate for R_b is rather given by Eq. (1.14). These estimates for the blockade radius R_b are reasonable estimates in general, but they take into account the effect of dephasing only approximately and neglect the effect of spontaneous decay on the blockade radius. Thus, the numerical blockade radius should be smaller than the estimate R_b in general to be on the safe side; in our simulations, $R_b^* = 0.8 R_b$ is usually used.

As can be seen from Figure 4.5, the pair correlation function $G^{(2)}(R)$ is fairly robust with respect to the choice of the numerical blockade radius; the distinct curves agree well for $R_b^* \leq R_b$. For $R_b^* \geq R_b$, however, even relevant states are excluded from the numerical calculation, spoiling the simulation result. Pictorially, the numerical blockade radius must be smaller than the first point of inflection of the $G^{(2)}$ function to preserve the main features of the $G^{(2)}$ function as well as the correct steady state of $\langle \mathcal{N} \rangle$, since the Rydberg population obviously decreases as more and more excited states are removed. For $R_b^* \leq R_b$, the state space truncation only introduces a small error without changing the main properties of both the $G^{(2)}$ function and the population data, which is exactly what is required for an approximation to be valid. For the analysis of the pair correlation function $G^{(2)}$, though, the numerical blockade radius should be chosen such that the onset of $G^{(2)}$ is still captured, requiring R_b^* to be considerably smaller than R_b.

4.4 Averaging Procedure

Unless lattice geometries are considered, the simulation includes, in addition to the quantum trajectory averaging, an averaging over different geometrical configurations. That is, the atoms are randomly placed inside the trap volume at the beginning of the simulation and a

(a) Quantum trajectories for a single geometrical configuration each (solid, color) together with the averaged curve (black, dashed).

(b) Averaged traj. for 10^3 geom., 100 traj. each (blue), 10^3 geom., 1 traj. each (yellow) and 10^4 geom., 1 traj. each (green)

Figure 4.6: Analysis of the averaging procedure. Parameters: (a) $N = 30$, $\gamma/2\pi = 0.01$, $1\,000$ runs. (b) $N = 15$, $\gamma/2\pi = 0.1$. Common parameters: $\Omega/2\pi = 1$, $C_6/2\pi = 900$, $\Gamma/2\pi = 1$, $\Delta/2\pi = 0$, $L_{1D} = 10$, $\delta t = 0.02$.

number n of quantum trajectories (traj.) are simulated using this particular geometry (geom.). After this, another geometrical realization is determined randomly and another set of quantum trajectories is simulated. This is typically repeated a large number of times and the resulting data is averaged, yielding the simulation result. The procedure is illustrated in Figure 4.6a: For each geometrical realization, the dynamics of the system are different, resulting in a fluctuation in the observables such as the Rydberg population. The average, however, reduces the impact of uncommon geometrical configurations and balances the different realizations. In that sense, the simulation reproduces the experimental procedure as it comprises the averages over different geometrical configurations that can arise in an experiment.

The averaging procedure begs the question of how the two averaging procedures relate to each other and whether both of them are required to yield good results. Considering Figure 4.6b, we find that the global population average does not depend on the number of quantum trajectories considered for a single geometrical configuration, but rather on the total sample size. Note that this statement does not implicate any insight into the interchangeability of the two averages — for the population observable, the averages are trivially interchangeable. It rather confirms the assumption that for an unordered sample the trajectory for a single geometrical configuration does not need to be fully converged to guarantee an accurate simulation result, as long as sufficient different realizations are taken into account. Indeed, one could imagine regrouping the quantum trajectories into 'geometrical similarity classes', thus obtaining converged trajectories for each representative geometry as is the case for a larger trajectory sample size for each geometry.

This conclusion holds even for the observable $G^{(2)}$ since the normalization of the correlation function is performed with the global population average, which does not — according to the previous explanation — depend on the number of quantum trajectories for a single geometrical realization.

It is therefore advantageous to decrease the number n of quantum trajectories for each geometrical configuration with respect to the number n_{geo} of geometrical configurations. For a typical simulation involving $N \gtrsim 30$ atoms in a one-dimensional trap of $L_{1D} \sim 10$, we usually use $n = 100$ and $500 \lesssim n_{geo} \lesssim 1\,000$. Considering the time evolution of the population as well

Routine	Scaling behavior
Calculation of jump connection array	$\sim \mathcal{O}(N^2 n_{st} \langle m \rangle^2) \sim \mathcal{O}(N^2 n_{st})$
Calculation of jump probability vector	$\mathcal{O}(n_{st} \langle m \rangle) \sim \mathcal{O}(n_{st})$
Determination of jumping atom	$\mathcal{O}(N)$
Jump projection	$\mathcal{O}(n_{st})$
Normalizing	$\mathcal{O}(n_{st})$
Matrix-vector multiplication	$\mathcal{O}(n_{st} N)$

Table 4.1: Scaling behavior of the numerical routines of the MCWF implementation.

as the $G^{(2)}$ function, it is readily apparent whether the number of simulations was enough to provide accurate data.

4.5 Efficiency

To fully characterize the MCWF technique we also need to discuss the efficiency of its implementation. Denoting the number of states with n_{st}, the number of atoms with N as before and the number of excitations with m, we find for the routines introduced in Algorithm 2 for the current implementation the scaling behaviors listed in Table 4.1. Except for the first routine 'Calculation of jump connection array', which belongs to the initialization block, all routines are called in each time step[10], leading to an overall scaling additionally multiplied by the number of time steps $n_\tau = t_{end}/\delta t$.

The initialization procedure 'Calculation of jump connection array' has a rather unfavorable scaling $\sim \mathcal{O}(N^2 n_{st})$, which could be significantly reduced by including it in the optimized state space construction routine described in Ref. [33]. However, this is not the bottleneck of our simulation since the array storing the jump connections has to be calculated only once for each geometry and can be reused in the successive simulations of the same geometry, which are required to obtain reasonable statistics. It is the time evolution which constitutes the bottleneck of our simulation as it involves the matrix-vector multiplication $\mathcal{H}_{nh} |\psi\rangle$, which is of order $\mathcal{O}(n_{st} N)$.

For a fixed set of typical parameters, the runtime for the MCWF simulation is shown in Figure 4.7. All calculations were performed on a single 3.4 GHz CPU core. To ensure a well-defined increase of the state space with the number of atoms, a lattice geometry was employed for the runtime study. As the number of states increases, the scaling $\mathcal{O}(n_{st} N)$ becomes dominant; the runtime for the remaining parts of the program such as state space construction or calculation of the jump connection array is negligible (well below 1%) compared to the calculation of the time evolution.

Due to adaptive step size control, the time step chosen by the GSL ordinary differential equations routine `gsl_odeiv_step_rk8pd` is typically much larger than δt on average for a coherent time evolution. Thus, enforcing the constant time step δt leads to an overall scaling of $\mathcal{O}(n_{st} N n_\tau)$ for the non-hermitian time evolution, with $n_\tau \sim \mathcal{O}(10^4)$ in typical simulations. Though an adaptive step size would be highly desirable for the MCWF algorithm (e.g. by requiring $\delta p \simeq \text{const} \ll 1$), is is not feasible since the additional $|\lambda_m \delta t| \ll 1$ constraint has to be taken care of as well, as discussed in Section 4.2. A fixed step size δt is therefore most convenient to use. A generalization of Eq. (3.10) to a higher order in δt as suggested in Ref. [44] might prove beneficial, yet even this approach is limited by the condition $|\lambda_m \delta t| \ll 1$.

---

[10]While the matrix-vector multiplication may be called several times in each time step, all other routines are called at most once per time step.
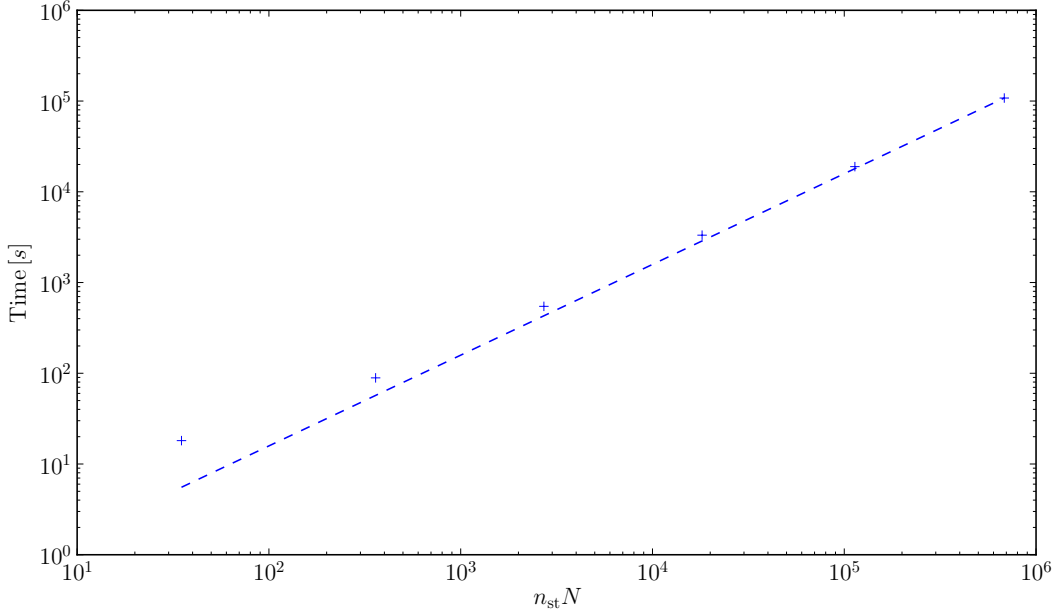
Figure 4.7: Runtime of a set of MCWF simulations ($n = 1000$) as a function of the product $n_{st}N$ (blue crosses). The blue, dashed line shows to a linear fit to the data.

If large systems consisting of many atoms are simulated, trivial parallelization is used to decrease the simulation time, i.e., the same simulation is run with fewer statistics on several kernels and the simulation results are combined at the end.

In summary, for the simulations typically performed using MCWF technique, the efficiency is basically limited by the time step δt which determines the number of matrix-vector multiplications that scale most unfavorably in the routine calculating a single quantum trajectory. The (unfavorable) scalings in the initialization procedure can be ignored compared to the scaling of the time evolution for our purposes. Therefore, any optimization must address primarily the acceleration of the matrix-vector multiplication. For further details on the implementation of the Schrödinger model, see Ref. [33].

Noting that the data structure used to store the Hamiltonian is a sparse matrix format [33] akin to the general compressed sparse row (CSR or CRS, compressed row storage) format, a genuine parallelization on graphics processing units (GPUs) using Compute Unified Device Architecture (CUDA) could be utilized to accelerate particular functions that perform the matrix-vector multiplication $\mathcal{H}_{nh} |\psi\rangle$ (cf. Ref. [83]).

5 MCWF Results

Having discussed the technicalities and possible issues concerning the wave function Monte Carlo technique in Chapter 4, we can now turn to the discussion of more physically motivated simulations, which is the topic of this chapter.

In the first part, Sections 5.1–5.3, we focus on the comparison between the MCWF and the two-level rate equation model developed in Refs. [36, 55] on the basis of the observables population and pair correlation function. The aim is to benchmark the rate equation in a partially coherent regime, and to assess the consequences of the approximations introduced during the derivation of the rate equation. We find that the rate equation yields correct results only in the strong dissipative regime ($\gamma \neq 0$, $\Gamma \gtrsim \Omega_{\mathrm{eff}}$), where coherent effects such as two-photon resonances do not contribute significantly to the the system's dynamics.

In addition, we study the impact of dissipative effects on the pair correlation function $G^{(2)}(R)$ in Section 5.3. While both dephasing and decay smear out the structure of the pair correlation function on resonance, the dephasing substantially decreases the blockade radius in addition and destroys the two-photon resonance present for off-resonant ($\Delta > 0$) excitation.

In Section 5.4 we discuss the build-up of spectral asymmetry in a small sample in which at most two excitations are possible. Comparing this to super atom dynamics, the differences in the dynamics can be ascribed to the different number of atoms contributing to the collective Rabi oscillations as well as to resonance effects.

Subsequently, the response of the atomic coherences present in our two-level model to an excitation pulse is examined in Section 5.5, motivated by recent experiments reported in Ref. [29]. Comparing our results with experimental data, it turns out that our two-level model does not reproduce the high-density data adequately, which we attribute to the elimination of the intermediate level not being justified here.

Finally, we investigate incoherent, off-resonant excitation dynamics in a one-dimensional disordered trap geometry in Section 5.6, in particular with respect to the dynamics of the excitation number fluctuation quantified by the Mandel Q parameter. We find non-trivial dynamics in the Q parameter for both resonant and far off-resonant excitation, associated with slow population increase due to slow equilibration in the weak dissipative regime ($\gamma \approx 0$). For off-resonant ($\Delta/2\pi = 5$) excitation, bimodal excitation statistics are observed at rather large times in the quasi coherent regime, which we trace back to coherent oscillations between ground and doubly excited states that are visible only for small system sizes.

Overall, this chapter comprises our main simulation results of the wave function Monte Carlo model, emphasizing the necessity to take dissipative as well as multi-photon effects into account when considering the dynamics of many-body Rydberg systems in the weak dissipative regime.

5.1 Super Atom Dephasing

Recalling the super atom picture introduced in Section 1.3 we could ask how incoherent effects such as dephasing modify the dynamics of a super atom [11]. This is an interesting question, since the super atom we discussed so far was a coherent system that exhibited an enhanced Rabi coupling of $\sqrt{N_b}\Omega$. Assuming negligible decay, $\gamma = 0$, but nonzero dephasing, the system can no longer be described using the collective states $|g \ldots g\rangle$ and $|+\rangle$ only, but the full singly excited state manifold is required as dephasing damps the atomic coherences, leaving the system in a totally mixed state. The population of the mixed state can easily be calculated by enforcing the detailed balance condition on the steady state, i.e., the rate by which the

(a) Excitation probability of a dephasing super atom as a function of the atom number N, comparing theory prediction (black, solid), MCWF (blue squares), rate equation [36] $\times 1/N$ (red, dashed) and Schrödinger equation [32] (green triangles) simulations. The inset shows $\langle \mathcal{N} \rangle(t)$ for $N = 30$.

(b) Rydberg population for a lattice configuration as a function of the detuning, comparing MCWF (blue, solid) and rate equation [36] (red, dashed) simulations.

Figure 5.1: Model comparison plots. In (a), the steady-state values using $\Omega/2\pi = 0.4$, $\gamma = 0$, $\Gamma/2\pi = 1$ and $\Delta = 0$ are plotted, in (b) $N = 15$, $\Omega/2\pi = 2$, $C_6/2\pi = 900$, $\gamma/2\pi = 0.5$, $\Gamma/2\pi = 1$ and the lattice spacing is $\Delta R = 0.7$.

ground state loses population must be equal to the rate by which it gains population,

$$N\rho_{g_1...g_N} = \sum_{i=1}^{N} \rho_{g_1...r_\alpha...g_N}. \tag{5.1}$$

Here, the diagonal density matrix elements are written in short-hand notation, $\rho_{i_1...j_N} = \rho_{i_1 i_1,...,j_N j_N}$ and we already canceled the effective (de-)excitation rate. Using the trace condition $\rho_{g_1...g_N} = 1 - \sum_i \rho_{g_1...r_\alpha...g_N}$, we find for the excited Rydberg fraction the simple expression [11]

$$\sum_{i=1}^{N} \rho_{g_1...r_\alpha...g_N} = \frac{N}{N+1}. \tag{5.2}$$

This result can be intuitively understood by recalling that in the dephasing-induced mixed state all states, in particular the N excited states and the ground state, are equally populated, yielding an excitation fraction of $N/(N+1)$.

Eq. (5.2) provides us with a nice relation to cross-check our MCWF model on the basis of an easy physical system. Choosing the numerical blockade radius to be large enough such that only one excitation is allowed in our system and selecting some arbitrary nonzero laser parameters which transform the system into the steady state, we can plot the excitation probability as a function of the atom number N. The result is shown in Figure 5.1a; the MCWF simulations nicely follow the theoretical prediction. The time evolution of the Rydberg population is shown in the inset of Figure 5.1a, featuring collective oscillations with Rabi frequency $\sqrt{N}\Omega$ with $N = 30$. The collectivity of the oscillations can be easily seen by noting that $1/\Omega = 2.5\,\mu s$, which is a time scale much larger than the period for the oscillations in the inset.

To assess the benefit of the MCWF simulations, we can also contrast its results with the ones obtained from solving the coherent Schrödinger equation (cf. Ref. [32]) as well as the steady-state rate equation (cf. Ref. [36]). The results, which are also shown in Figure 5.1a, clearly differ from the theoretical prediction. For the coherent Schrödinger model, the reason is simply that the population coherently oscillates between the ground and the excited state with Rabi frequency $\sqrt{N}\Omega$ and hence the temporal averaging required to obtain a steady-state value yields just $1/2$ for the excited Rydberg fraction.

For the rate equation, the reason is more subtle. Calculating the single-atom steady-state value for a two-level atom

$$\langle \mathcal{N}^{(\alpha)} \rangle = \frac{1}{2 + \gamma \dfrac{(4\Delta_{\text{eff}}^2 + (\gamma + \Gamma)^2)}{4(\gamma + \Gamma)\Omega^2}} \,, \tag{5.3}$$

on which the rate equation [36] is based on, we see that for $\gamma \to 0$ the steady-state value converges to $1/2$, independent of the interaction which is incorporated in the effective detuning Δ_{eff}. Ergo, the blockade is not accounted for[11], leading to a steady-state value of $1/2$ for both Rydberg and ground state. The overall Rydberg excitation probability is thus $N/2$, which has been scaled in Figure 5.1a by a factor of $1/N$ to fit the scale of the plot. The particular choice of $\gamma = 0$ is somewhat artificial, admittedly, as it renders the rate equation useless by focusing on a case that can be argued to be a pathological case[12]. Nevertheless, the system considered is a very illuminating example of a system for which the existing models, namely the rate equation and the coherent Schrödinger model, do not capture the relevant properties.

Similar findings have been reported in Ref. [38]. There, a benchmark of the rate equation for a super atom consisting of $N \leq 10$ atoms using full density matrix calculation is discussed, finding good agreement for $\gamma \neq 0$, $\Gamma = 4\Omega$ (note the different definition of the dephasing term as discussed in Section 2.5).

It should be noted that the regime $\gamma \simeq 0$ is troublesome in general with respect to convergence properties (cf. Section 5.3) if more than one super atom is considered. In many experiments (e.g. [4]), however, the system is measured before it has reached its steady state, such that a dynamical simulation of the system is inevitable and techniques like the MCWF technique are needed.

5.2 Resonant Effects in a Lattice Geometry

In the previous section we have checked the correct implementation of the wave function Monte Carlo model as well as discussed its advantages with respect to other state-of-the-art models, especially the rate equation. In this section we now consider a lattice geometry with lattice spacing $\Delta R = 0.7$ and $C_6/2\pi = 900$ to further examine the range of validity of the rate equation, specifically the validity of the approximation made by ignoring the two-photon resonance process (cf. Section 3.1) in this particular setup. Due to the strong nearest neighbor interaction, the lattice sites are blockaded up to the next-nearest-neighbor site, implying that excitations are spaced by at least $3\Delta R$.

Plotting the Rydberg population as a function of the detuning, we expect a peaked structure with the peak position corresponding to the specific (positive) detuning values for which the Rydberg interaction of a certain inter-atomic separation corresponding to integral multiples of ΔR is compensated. This is shown in Figure 5.1b. Whereas the rate equation and the

---

[11]More precisely, for $\gamma = 0$ the blockade effect only applies for finite times, as discussed in Section 5.6 and at the end of Section 4.2.

[12]For $\gamma \simeq \varepsilon$ with ε an 'arbitrarily small' positive quantity, the rate equation converges to $\approx N/(N+1)$.

MCWF simulation both show a peak at $\Delta_\gamma^{(1)}$ and $\Delta_\gamma^{(2)}$, the peak at $\Delta_{2\gamma}^{(1)}$ is unique for the MCWF simulation, indicating the breakdown of the rate equation approximation, namely the approximation that two-photon resonance effects can be ignored. Not surprisingly, neglecting the two-photon process also leads to a slight overestimation of the single-photon resonant process for the rate equation.

In fact, regarding the definitions

$$\Delta_\gamma^{(1)}/2\pi = \frac{C_6}{(3\Delta R)^6}\,, \quad 2\Delta_{2\gamma}^{(1)}/2\pi = \frac{C_6}{(3\Delta R)^6} \quad \text{and}$$

$$\Delta_\gamma^{(2)}/2\pi \simeq \frac{C_6}{2}\left(\frac{1}{(4\Delta R)^6} + \frac{1}{(5\Delta R)^6}\right), \tag{5.4}$$

we immediately see that the resonance $\Delta_{2\gamma}^{(1)}$ can be attributed to a two-photon resonance, even in the presence of dephasing. This is a particular property of lattice geometries, since for an appropriate detuning, the number of atoms which have a nearest neighbor distance that overlaps with the narrow two-photon resonance width is much smaller in an unordered sample than in a lattice geometry with fixed lattice spacing.

Note that the estimate (5.4) is an effective estimate which assumes that the single-photon resonances $C_6/(4\Delta R)^6$ and $C_6/(5\Delta R)^6$ are approximately equally likely and hence the peak at a small positive detuning is just the superposition of the two resonances. This seems to be justified since, due to the rapid decrease of the van der Waals potential, only the smallest resonance distances need to be considered to understand the excitation structure of Figure 5.1b.

Consequently, rate equation results should be treated with care regarding off-resonantly driven lattice geometries in the weakly dissipative regime $\Omega > \Gamma, \gamma$.

5.3 Pair Correlation Function: A Parameter Study

A complementary way to use lattice geometries to access the spatial excitation characteristics of the atomic cloud is to utilize the pair correlation function $G^{(2)}(R)$ as introduced in Section 4.3. With the help of the pair correlation function, the ratio of single to two-photon excitation processes can be assessed even for an unordered sample since the resonance distances for both kinds of resonances differ.

To study the impact of incoherent processes on the pair correlation function it is most expedient to contrast simulation results that differ in a single parameter only. With respect to dephasing, a plot of the pair correlation function $G^{(2)}(R)$ is shown in Figure 5.2 for the dephasing constants $\Gamma = 0$ and $\Gamma/2\pi = 2$, respectively. Note, however, that apart from the dephasing constants, also the range of detuning values scanned in Figure 5.2 differ, the reason being that with increasing dephasing, the numerical blockade radius decreases, rendering the simulation highly time consuming, such that the simulation of Figure 5.2b had to be aborted after a fair simulation time.

For zero dephasing, two pronounced peaks can be observed in Figure 5.2a, corresponding to the single and two-photon resonance, whose conditions read $R_\gamma = (C_6/\Delta)^{1/6}$ and $R_{2\gamma} = (C_6/2\Delta)^{1/6}$, respectively. The dashed, white line shows the expected resonance positions, nicely fitting the simulation results. The resonance peaks are echoed at larger distances, corresponding to higher order correlations which naturally arise in a system with well defined excitation distances. That is, a strong probability to find two excitations in a distance R' also entails a nonzero probability to find two excitations in the distance $2R'$, which is simply the next-nearest resonant excitation distance.

For increasing dephasing, the two-photon resonance gets smaller and even vanishes, while
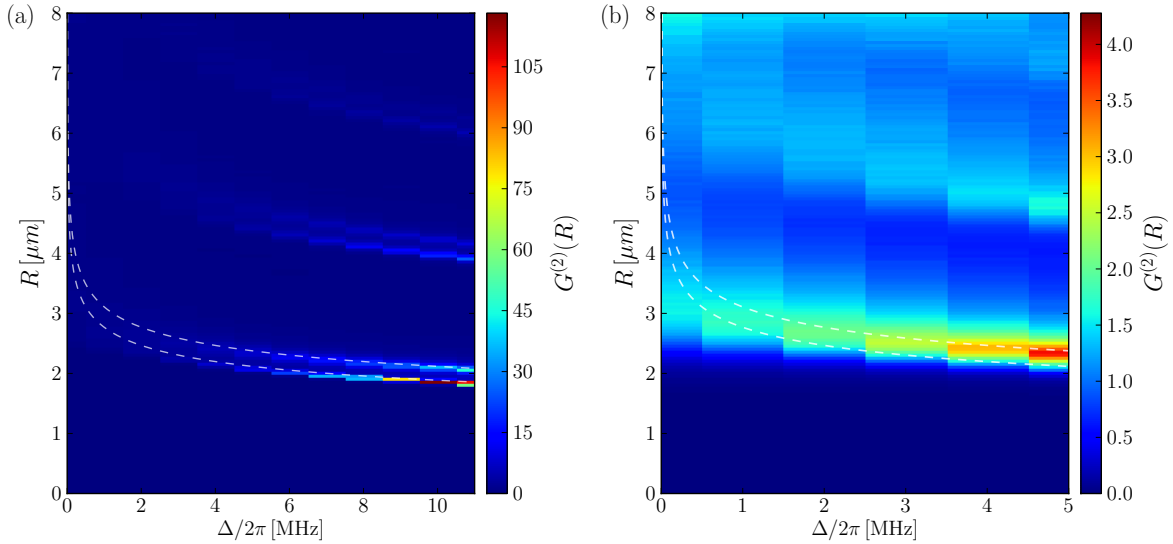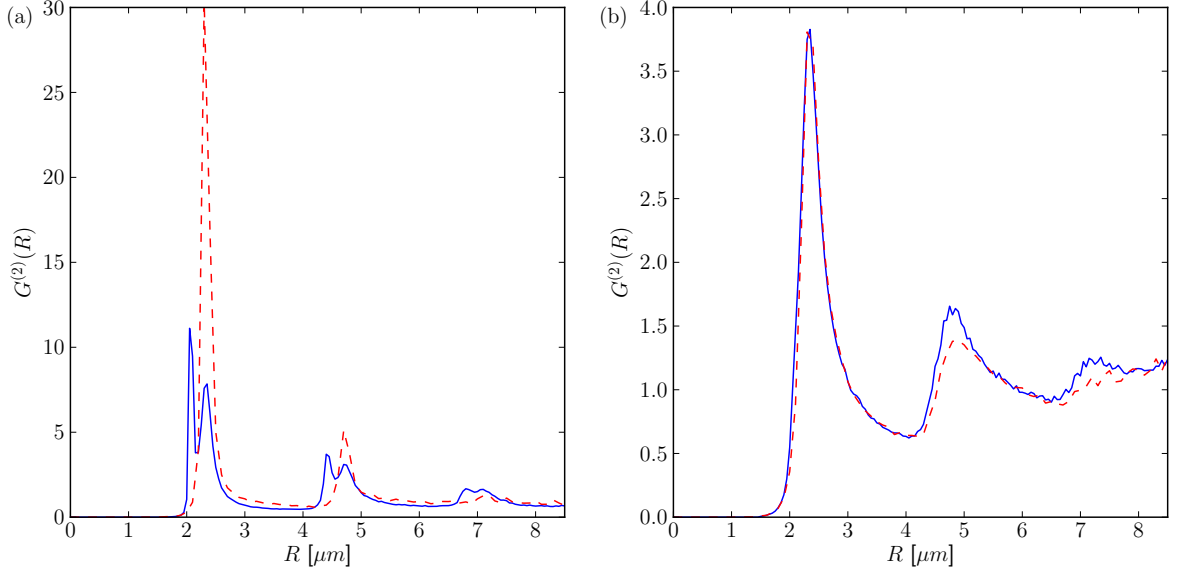
Figure 5.2: Pair correlation function $G^{(2)}(R)$ as a function of the detuning for different dephasing rates $\Gamma = 0$ (a) and $\Gamma/2\pi = 2$ (b). Further parameters: $N = 30$, $\Omega/2\pi = 1$, $C_6/2\pi = 900$, $\gamma/2\pi = 0.2$, $L_{1D} = 10$. The dashed, white lines correspond to the resonant distances $R_{2\gamma} = (C_6/2\Delta)^{1/6}$ and $R_\gamma = (C_6/\Delta)^{1/6}$, from bottom to top.

the single-photon resonance gets smeared out and broadened. This can be most easily seen in Figure 5.3, which shows a vertical cut through Figure 5.2 at the detuning $\Delta/2\pi = 5$. Loosely speaking, while for $\Gamma = 0$ the two photon peak dominates, only the single-photon resonance peak is left for $\Gamma/2\pi = 2$. Strictly speaking, we cannot state anything but that the single-photon peak apparently dominates in Figure 5.3b, since due to the small distance separating the two peaks we cannot exclude the two-photon peak just being superposed with the broadened single-photon resonance peak, yielding a single peak with a slight shoulder.

The reduction of the two-photon resonance can be intuitively understood by considering the damping effect of the dephasing on the coherences. The direct transition $|gg\rangle \leftrightarrow |rr\rangle$ not populating the singly excited states is possible only by means of two-atom coherences, which get destroyed by a large dephasing. Consequently, a large dephasing leads to population dynamics that always involve the singly excited states, which, in turn, result in a relative enhancement of single-photon processes.

In addition to the wave function Monte Carlo results, also rate equation [36] results are shown in Figure 5.3, allowing us again to judge the range of validity of the rate equation. For zero dephasing when coherent effects such as two-photon excitations are not negligible, the rate equation clearly fails (cf. Figure 5.3a). Basically, this is not surprising, given the fact that the rate equation *a)* totally ignores inter-atomic coherences which are essential in coherent (or quasi coherent) systems and *b)* ignores any resonant processes higher than first order (single-photon) processes. It is not clear, however, how the neglect of inter-atomic coherences translates into observables such as the $G^{(2)}$ function apart from the missing two-photon peak. Figure 5.3a suggests that for a quasi coherent system (nonzero, but relatively small decay), the single-photon resonance is significantly overestimated by the rate equation model. The reason for introducing the decay constant $\gamma/2\pi = 0.2$ is that the rate equation [36] is only able to calculate steady-state values. The decay ensures that the system has reached its steady state in the time scales simulated using MCWF technique.

For nonzero dephasing, the rate equation agrees surprisingly well with the MCWF results (cf. Figure 5.3b), supporting the claim that for large dephasing (large compared to coherent quantities such as the collective Rabi frequency) the rate equation becomes a valid model since the 'classical' approximation, i.e., the disregard of inter-atomic coherences, applies. The

Figure 5.3: Off-resonant ($\Delta/2\pi = 5$) pair correlation function $G^{(2)}(R)$ for different dephasing rates $\Gamma = 0$ (a) and $\Gamma/2\pi = 2$ (b), comparing MCWF (blue, solid) and rate equation [36] (red, dashed) simulations. All other parameters are identical to Figure 5.2.

same conclusion can be drawn by considering, instead of off-resonant excitation, resonant excitation with $\Delta = 0$. Just as in the off-resonant case, the $G^{(2)}$ function of the rate equation agrees with MCWF simulations for $\Gamma/2\pi = 2$ whereas a significant deviation is observed for $\Gamma = 0$.

As a rule of thumb, the rate equation can be applied whenever the simulated system is strongly dissipative, i.e., $\Gamma/\Omega_{\text{eff}} \gtrsim 1$ and $\gamma \neq 0$. The effective Rabi frequency Ω_{eff} includes the collective enhancement $\sqrt{N_b}$ and possibly some (weak) detuning-dependence. To give a precise formula is beyond the scope of this thesis, since it would require an extensive parameter study involving Γ, γ, N and Δ for different trap dimensionalities d. While significantly nonzero decay ensures convergence to a steady state in finite time, the dephasing guarantees the validity of the rate equation approximations, viz. negligible inter-atomic coherences that allow for the neglect of resonant two-photon excitations. Note that strong atomic decay also reduces the inter-atomic coherences by reducing the Rydberg population. Though the above analysis is based on pair correlation functions only, our conclusion also applies to other observables such as the Rydberg population. The need for large atomic dephasing for the rate equation to yield valid results has also been noted in Ref. [38].

To get a sense of how incoherent effects such as dephasing and decay modify the resonance properties captured by $G^{(2)}(R)$, let us now consider the limiting cases, i.e., $\Gamma = 0$, $\gamma \neq 0$ and $\gamma \approx 0$, $\Gamma \neq 0$.

In Figure 5.4a, $G^{(2)}(R)$ is shown on resonance ($\Delta = 0$) for $\Gamma = 0$, $\gamma \neq 0$, contrasted to the coherent case $\Gamma = \gamma = 0$ (blue, dashed). As the decay constant increases, the blockade radius slightly decreases while the peak position of $G^{(2)}(R)$ does not significantly change. In addition, the maximum of $G^{(2)}(R)$ gets smaller and the structure of the pair correlation function gets smeared out. Interestingly, the effect of the increased decay constant does not seem to be very strong for the chosen laser parameters (in particular $\Delta = 0$): it only slightly changes the curve progression.

For 'approximately zero' decay, the system hardly reaches its steady state for 'finite' simulation times, making it an extremely unfavorable system to simulate numerically. Still, one can evaluate $G^{(2)}(R)$ at a point at which the population is changing only slightly. This is done in Figure 5.4b where $G^{(2)}(R)$ is averaged over a time span for which the population
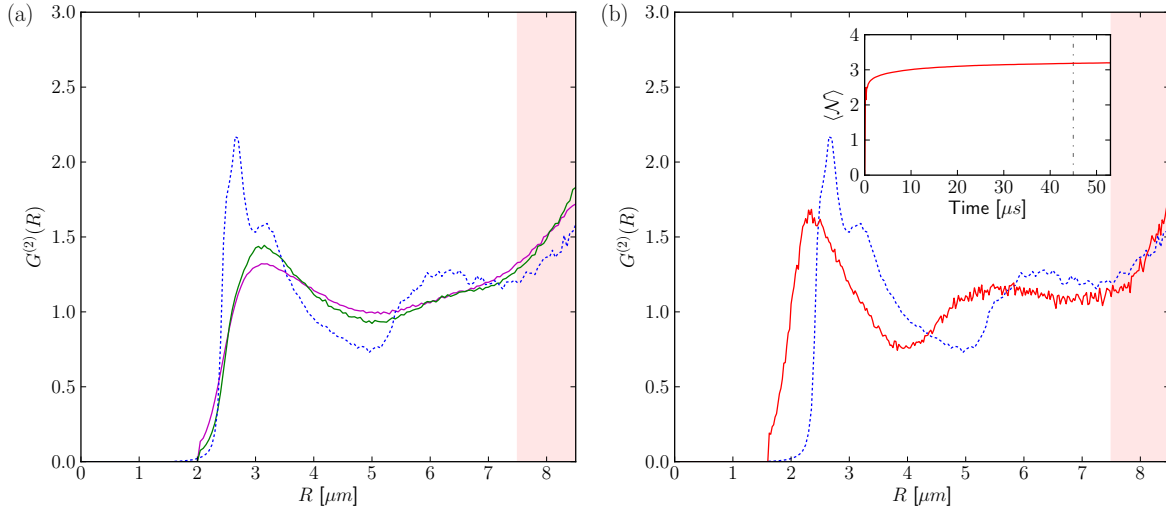
Figure 5.4: Pair correlation functions $G^{(2)}(R)$ for different rates γ, Γ: (a) $\Gamma = 0$ and $\gamma/2\pi = 0.5$ (solid, green), $\gamma/2\pi = 2$ (solid, magenta); (b) $\gamma/2\pi = 0.001$, $\Gamma/2\pi = 1$ (red, solid). In the inset, the time evolution is shown; the dash-dotted line indicates the start of the temporal $G^{(2)}(R)$ averaging for the red line in (b). The blue, dashed line in both figures shows the coherent case with $\gamma = \Gamma = 0$ [32]. The reddish shaded area indicates dominance of finite-size effects. The abrupt onset of $G^{(2)}(R)$ is due to the numerical blockade radius, i.e., an artifact of the numerical calculation. Further parameters: $N = 30$, $\Omega/2\pi = 1$, $C_6/2\pi = 900$, $\Delta = 0$, $L_{1D} = 10$.

doesn't change significantly, as indicated by the dash-dotted line in the inset, which marks the starting point of the averaging. Figure 5.4b allows two observations.

Firstly, the double peak structure disappears. Analyzing the contributions of the different excitation subspaces, we find that the double peak structure is mainly due to the threefold excited subspace $m = 3$ whereas for the red curve, the $m = 4$ subspace dominates. This observation is consistent with our expectation that an increased dephasing leads to an enhanced population of the higher excited subspaces, stemming from the observation that for two interacting atoms with $\Delta = 0$, dephasing-induced damping of the coherences leads to an enhanced population of the doubly excited state in the absence of an appreciable decay (cf. Figure 5.8 and the associated discussion in Section 5.6). Reconsidering Figure 5.4a where the main contribution to $G^{(2)}(R)$ is due to the $m = 2, 3$ subspaces, we conclude that the first sub-peak is caused by coherent effects which vanish as incoherent processes become stronger.

Secondly, the blockade radius gets smaller. Simply put, the dephasing increases the laser linewidth[13], thereby allowing to excite atoms with higher interaction energies (cf. Figure 1.3), which explains the decrease of the blockade radius. For the sake of completeness we should add that the laser linewidth is also broadened by power-broadening, which denotes broadening due to the laser intensity itself, as can be seen from Eq. (5.3): The FWHM is directly proportional to Ω.

For general systems, usually none of the limiting cases applies, but rather both incoherent processes need to be taken into account. Highly excited Rydberg states in the ultracold regime might represent an exception to this rule, featuring extremely small decay constants, but in these cases, experiments normally don't access the steady state of the system but an intermediate state which is readily obtained using MCWF technique.

We cannot state a precise estimate of the blockade radius as a function of the master equation parameters since the Rydberg blockade in a disordered sample depends non-trivially

---

[13]This can be seen by plotting the single-atom Rydberg steady-state value (5.3) over the detuning and varying the dephasing constant.

on many-body interactions and collective effects. For a resonant system to which the rate equation can be applied, an estimate taking into account incoherent effects can be determined semi-analytically by solving for the distance at which the super atom excitation probability as a function of the interaction-induced detuning has fallen off to $1/2$, as has been discussed in Ref. [33]. However, our simulation results shown above suggest that, while decay mainly smoothens the pair correlation function, dephasing also has a significant impact on the blockade radius in addition to its spoiling of the two-photon resonance. Note that these conclusions are drawn from the analysis of the pair correlation function on resonance, i.e., we did not study the impact of spontaneous emission on the two-photon resonance peak in detail. Instead, we focused on the experimentally most important parameter regime, which is characterized by small Rydberg decay but potentially large dephasing.

5.4 Time-Dependent Population Asymmetry

Having mainly discussed the steady-state behavior of the simulated observables, we now focus on the time dependence of observables such as the Rydberg population. In particular, we are interested in what happens when we move from a single super atom to a system with more — say, two excitations for the beginning.

For that purpose, we first consider a single super atom and evaluate the time-dependent Rydberg population as a function of the detuning. The resulting dynamics are shown in Figure 5.5a. Since only one excitation is possible, no resonant excitations can occur, leading to a totally symmetric excitation spectrum around $\Delta = 0$. The dynamics of the system are easily understood by means of single-atom characteristics only, i.e., the collective Rabi oscillation is modified according to

$$\Omega_0 \to \Omega'(\Delta) = \sqrt{N\Omega_0^2 + \Delta^2}\,, \tag{5.5}$$

where Ω_0 denotes the single-atom Rabi frequency and N the number of atoms that are contributing to the collective behavior. In Figure 5.5a, the white, dashed lines indicate the positions of the population maxima, which are given by $(0.5 + i)/\Omega'(\Delta)$ with $i \in \{1, \dots, 4\}$, respecting that the first maximum of a single-atom Rabi cycle with $\Omega/2\pi = 1$ occurs at $t = 0.5\,\mu s$. The inset shows the Rydberg population as a function of the detuning at two times, $t = 0.13\,\mu s$ (blue curve) and $t = 4.8\,\mu s$ (red curve). It can be seen that the population stays symmetric around resonance $\Delta = 0$ for all times and that the steady-state population of the super atom is independent of the detuning, whose only effect is to slow down the equilibration. Moreover, given the time evolution of the system, quantities like the atom number can be readily determined. For instance, reading off $\Delta t \simeq 0.18\,\mu s$ for a single Rabi oscillation on resonance, we find $\sqrt{N}\Omega_0 \simeq 1/0.18$ which yields $N \approx 30$ for the parameters of Figure 5.5a, as expected.

Considering a system in which two excitations are possible, we find that the dynamics is much more versatile, even though collective Rabi oscillations are observed in this case as well, with $\sqrt{N_b}\Omega$ instead of $\sqrt{N}\Omega$,

$$\Omega_0 \to \Omega'(\Delta) = \sqrt{N_b\Omega_0^2 + \Delta^2}\,. \tag{5.6}$$

The corresponding dynamics are shown in Figure 5.5b; the white, dashed lines are given as above by $\Omega'(\Delta)$ with the only difference being the replacement $N \to N_b$ where N_b can be estimated from the $G^{(2)}$ function via $N_b \simeq N \times R_{\mathrm{onset}}/L$. However, while in the super atom case we found a totally symmetric excitation spectrum around resonance, there is a population maxima in Figure 5.5b at all times, which shifts towards positive detuning values
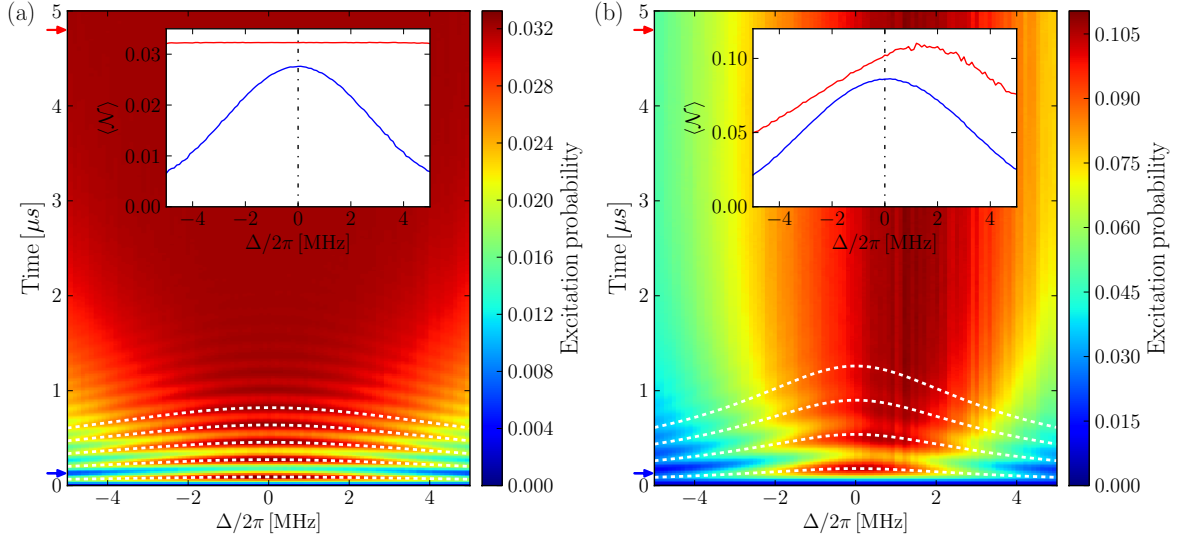
Figure 5.5: Time-dependent Rydberg population per atom as a function of the detuning for a super atom (a) with only one excitation and for a system with two excitations (b). In (a), $N = 30$ and $\gamma = 0$; in (b), $N = 10$, $\gamma/2\pi = 0.1$ and trap length $L_{1D} = 3.5$. Common parameters: $\Omega/2\pi = 1$, $C_6/2\pi = 900$ and $\Gamma/2\pi = 1$. The dashed, white lines follow the population maxima (cf. text). The insets show the Rydberg population as a function of the detuning at $t = 0.13\,\mu s$ (blue curve) and $t = 4.8\,\mu s$ (red curve), respectively. The arrows in corresponding colors indicate the evaluation times in the main figures.

over time as shown in the inset.

This behavior can be understood by recalling that, for positive detuning values, the detuning can compensate for the Rydberg-Rydberg interaction, giving rise to resonant effects. Since such processes build up over time, the maximum of the Rydberg excitation shifts towards positive detunings until the steady state of the system is reached.

More specifically, in the coherent case we can write an interacting two-atom system at two-photon resonance in the basis $\{|gg\rangle, |+\rangle, |rr\rangle\}$ and subsequently eliminate the intermediate level assuming $\Delta \gg 1$ and $2\Delta \simeq \mathcal{V}_{rr}$. Then, the reduced system exhibits Rabi oscillations between the ground and the doubly excited state with the Rabi frequency Ω^2/Δ. In the presence of dephasing and decay, the impact of two-photon resonance effects decreases in favor of single-photon resonance effects. Still, resonant excitations build up over time, rendering the excitation spectrum manifestly time-dependent.

In principle, one can quantify the asymmetry by introducing the asymmetry parameter

$$A_{\mathrm{LR}} = \frac{\langle \mathcal{N} \rangle_R - \langle \mathcal{N} \rangle_L}{\langle \mathcal{N} \rangle_R + \langle \mathcal{N} \rangle_L} \tag{5.7}$$

with $\langle \cdot \rangle_L = |\int_{-\Delta_{\max}}^{0} \langle \cdot \rangle \, \Delta \, d\Delta|$ and $\langle \cdot \rangle_R = |\int_{0}^{\Delta_{\max}} \langle \cdot \rangle \, \Delta \, d\Delta|$. Analyzing the asymmetry parameter A_{LR} we find that the asymmetry is dominated by the Rabi oscillations whose phases are different for each detuning value at short times, while a constant value is reached as the system approaches its steady state.

When discussing resonance effects, note that the notion of 'either' single-photon 'or' two-photon processes involved in the dynamics is misleading in general as quantum mechanics never 'keeps things separate'. We can only identify dominant contributions of certain processes to the observables we are interested in, while needing to keep in mind that our simple picture of two separate and separable processes holds only for systems for which the interaction strength as well as the detuning can be accurately controlled (e.g. in a lattice geometry).

5.5 Dynamics of Atomic Coherences

Motivated by recent experiments [29], we now turn to the study of the atomic coherences present in our two-level system. More precisely, we evaluate the imaginary part of the atomic coherences,

$$\langle \mathcal{D} \rangle \equiv \left\langle \sum_\alpha \Im\{|r_\alpha\rangle \langle g_\alpha|\} \right\rangle, \tag{5.8}$$

in our simulation. As the imaginary part of the susceptibility χ quantifies the absorption of light by an atomic gas [84] and $\chi \propto \rho_{rg}$ for a two-level atom [50], $\langle \mathcal{D} \rangle$ is proportional to the absorption of the laser light propagating through a gas of two-level atoms. Technically, the coherence can be easily extracted since the single-atom operator in Eq. (5.8) couples states differing by one excitation, which is simply the upper triangular part of the Hamiltonian matrix (2.29) modulo the Rabi frequency $\Omega/2$.

In thermal Rydberg vapor, the motional degrees of freedom cannot be neglected in the first place, so we need to take into account the Doppler shift in our simulation. Starting from a three-level system, this can be done by replacing the detuning of the intermediate level by $\Delta_1 \to \Delta_1 + k_p v$ and $\Delta - \Delta_1 \to \Delta - \Delta_1 - k_c v$ [85], with p, c denoting probe and coupling laser wave vector, respectively (cf. Figure 2.1). Accordingly, the interacting Rydberg level is effectively shifted by

$$\Delta_{\text{Dpl}} = (k_p - k_c)v. \tag{5.9}$$

Note that the different signs for probe and coupling beam originate from the experimental setup, i.e., counter-propagating lasers. The Doppler shift (5.9) can now be easily implemented in our two-level MCWF simulation. First, the velocity v is drawn from the Maxwell-Boltzmann distribution

$$f(v) = \frac{1}{\sqrt{2\pi}u} e^{\frac{-v^2}{2u^2}} \tag{5.10}$$

with $u = \sqrt{k_B T/m}$, m being the atom mass, k_B the Boltzmann constant and T the temperature in Kelvin. Each atom is Doppler shifted according to its velocity, randomly drawn from the distribution (5.10). In the simulation, many-body states form the basis states and hence the shifts need to be summed up in order to yield the effective Doppler shift, $\Delta_{\text{tot}}^{(\ell)} = \sum_\alpha \Delta_{\text{Dpl}}^{(\alpha)}$ with α denoting the excited atom in the many-body state ℓ.

The model introduced for the Doppler shift is only a first approximation since it totally disregards the motion of the atoms, i.e., it considers the atoms as non-colliding particles with fixed velocities that are frozen in position space during the time evolution of the system. This approximation only holds for very small excitation times as the ones used in the experiments [29]. In the parameter regime of the experiments [29], the impact of the Doppler shift on the coherence is expected to be rather small (cf. supplemental of Ref. [29]).

In the experiments, the effective Rabi frequency is $\Omega/2\pi \simeq 550$ [29]; much larger than the frequencies usually employed in our simulations. To avoid possible issues with numerical instabilities, all parameters entering the MCWF simulation are rescaled by the effective Rabi frequency, reading $C_6/(2\pi\Omega) \simeq 0.7$ for the $37S$ state [54], $\Gamma/(2\pi\Omega) \simeq 0.5$ and $\Delta = \gamma = 0$; moreover, also the Doppler shift calculated via (5.9) is rescaled by the Rabi frequency. To make simulation data as comparable as possible, the experimental excitation pulse of Ref. [29] with peak height normalized to 1 is implemented.

With a rescaled C_6 coefficient smaller than unity and consequently weak blockade, the
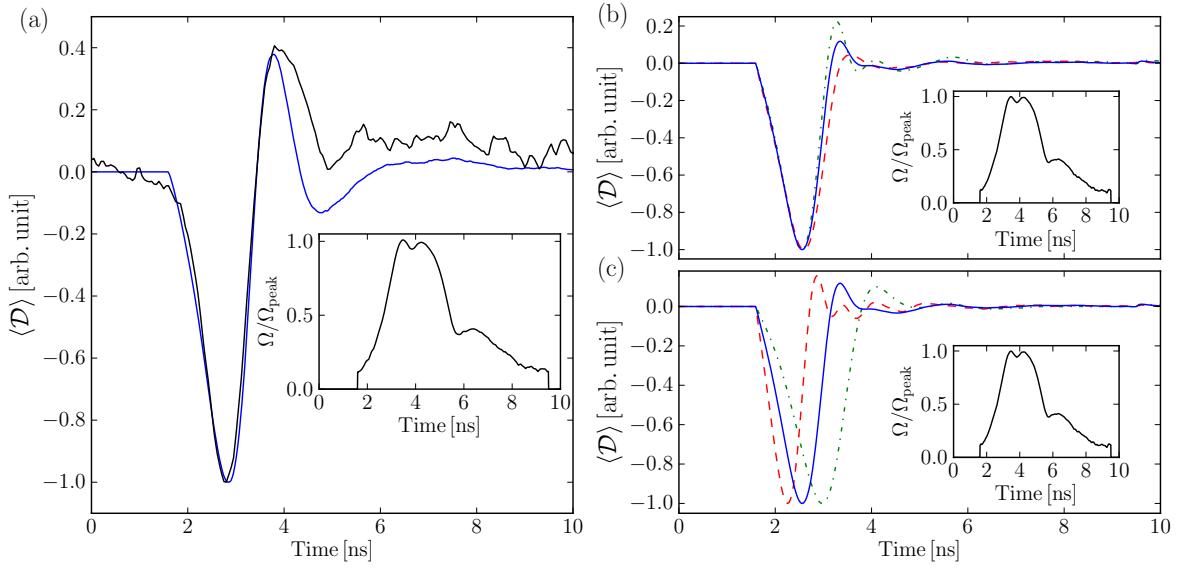
Figure 5.6: Time-dependent atomic coherences in the low (a) and high (b), (c) density regime. In (a), the MCWF simulation (blue) is compared to experimental data [29] (black). The experimental density $\sim 1.6 \times 10^{12}$ cm^{-3} is modeled using a cylindrical trap containing $N = 3$ atoms (cf. text). In (b) and (c), a density of $\sim 6.5 \times 10^{12}$ cm^{-3} is simulated and for fixed Rabi frequency the dephasing constant is varied (b) and vice versa (c). The solid blue line in both plots corresponds to the parameters $(N, \Gamma/2\pi\Omega, \Omega_{\text{peak}}/2\pi\Omega) = (20, 0.5, 1)$ while the curves in (b) correspond to $(16, 0.2, 1.0)$ (green, dash-dotted), $(16, 1.0, 1.0)$ (red, dashed) and in (c) to $(16, 0.5, 0.5)$ (green, dash-dotted) and $(16, 0.5, 2.0)$ (red, dashed). The insets show the pulse shape employed in the respective simulation [86].

simulation of some physical density is only possible using a very small excitation volume that contains few atoms. For an experimental density[14] of $\sim 1.6 \times 10^{12}$ cm^{-3} ($T \simeq 65°$C), $N = 3$ atoms are placed in a cylindrical trap of radius $R = 0.72\,\mu m$ and length $L = 4\,\mu m$. In the high density regime ($\sim 6.5 \times 10^{12}$ cm^{-3}), the impact of using different excitation volumes is analyzed by placing on the one hand $N = 16$ atoms in a cylindrical trap of radius $R = 0.8\,\mu m$ and length $L = 4\,\mu m$ whereas on the other hand $N = 20$ in the same trap with increased length $L = 5\,\mu m$.

The simulation results are shown in Figure 5.6. Figure 5.6a shows that the low density MCWF simulation reproduces the first one and a half Rabi cycles of the coherence correctly but fails to reproduce the enhanced duration of the second Rabi cycle. The two-level coherences also approach small values more rapidly than the experimental data. Keeping in mind that the signal basically quantifies the absorption of the laser beam driving the lower transition, the positive values measured experimentally could indicate that some population is still trapped in the Rydberg state, reducing the absorption on the lower transition.

Figures 5.6b, 5.6c correspond to high density simulations; in Figure 5.6b the dephasing constant is varied for a fixed Rabi frequency whereas conversely the Rabi frequency is varied for a fixed dephasing in Figure 5.6c. The latter two plots allow for more in-depth observations.

Firstly, comparing the blue with the red dashed and the green dash-dotted line, respectively, we see that the atomic coherences seem to be already converged with respect to system size, i.e., the slight variation of the number of atoms and the trap size does not have any significant impact on $\langle \mathcal{D} \rangle$ (cf. Figure 5.6b). Secondly, while an increasing dephasing damps out the coherences more rapidly, the main features remain unchanged. This observation holds true for the variation of the Rabi frequency as well, though the oscillation period as well as the

---

[14]Note that the densities modeled are actually the experimental densities multiplied by a factor of ~ 0.3, accounting for the fraction of ^{85}Rb atoms and the fraction of the laser-addressed hyperfine $F = 2$ level [29, 86].

number of oscillations strongly depend on the Rabi frequency (cf. Figure 5.6c). Lastly, the qualitative features of the time-dependent atomic coherences, notably the overshooting above $\langle \mathcal{D} \rangle = 0$ after the first Rabi cycle, can be observed in all simulations.

Supplementary simulations indicate that the qualitative features mentioned before do not change in the presence of a small decay; the many-body coherence is modified after its first local maximum but maintains its main properties before reaching the first local maximum, as expected for the large time scale associated with a small decay constant.

We conclude that our simple two-level model fails to reproduce the experimental data in the high density regime which exhibits a non-trivial dependency of the shape of the first local maximum on the density [86]. We attribute the failure to the neglect of the third, intermediate level, whose coherence with the ground state is experimentally probed. Thus, a three-level treatment seems to be required to obtain meaningful information on the atomic coherences, which are not well modeled by means of a two-level description, even though full quantum correlations between the atoms are taken into account. We conclude this, although the simulation results discussed above feature some uncertainty associated with the model parameters, on grounds of the invariant qualitative features of the extracted coherences. The importance of the third level has also been noted in [29], and is a consequence of the large Rabi frequencies, which are comparable to the detuning of the intermediate state.

5.6 Excitation Dynamics

Up to now, only the Rydberg population $\langle \mathcal{N} \rangle$ as well as the atomic coherences $\langle \mathcal{D} \rangle$ have been analyzed from the point of view of dynamics. Therefore, a detailed analysis of excitation dynamics is performed for a simple one-dimensional geometry in this section.

More precisely, we study the impact of spontaneous decay on dynamical observables such as the Rydberg population and the Mandel Q parameter introduced below for resonant and off-resonant excitation in the presence of considerable dephasing. Depending on the equilibration time scale, these observables are found to exhibit significant dynamics which might be relevant in current experiments [4, 40]. Besides that, we consider quasi-coherent, off-resonant excitation, which features a bimodality in the excitation statistics even at times large as $t = 6 \, \mu s$ at $\Delta/2\pi = 5$. We attribute this bimodality to dynamical effects, namely the coherent oscillation between ground states and doubly excited states, as well as finite-size effects, namely the limited number of excited pairs constrained by the system size.

Aiming at a comprehensive study of excitation dynamics, we realize that the observables such as the Rydberg population introduced so far provide only limited information on the excitation dynamics, meaning that detailed knowledge of the mean Rydberg population $\langle \mathcal{N} \rangle$ does not include any information on whether, in each simulation, a fixed number of atoms is excited from the cloud or whether the excitation statistics features a strongly bimodality with respect to the excitation numbers. These features, which characterize the excitation statistics, are not quantified by the first moment $\langle \mathcal{N} \rangle$ of the excitation distribution. Higher moments are required to further characterize the full excitation (counting) statistics.

For this purpose, it has become conventional to utilize the Mandel Q parameter defined as

$$Q = \frac{\langle (\mathcal{N} - \langle \mathcal{N} \rangle)^2 \rangle}{\langle \mathcal{N} \rangle} - 1, \tag{5.11}$$

which compares the measured excitation number fluctuations directly with Poisson statistics with $\langle (\mathcal{N} - \langle \mathcal{N} \rangle)^2 \rangle = \langle \mathcal{N} \rangle$, i.e., $Q = 0$ indicates Poissonian, $Q < 0$ sub-Poissonian (squeezed), and $Q > 0$ super-Poissonian (broadened) statistics. In the same manner, the third cumulant
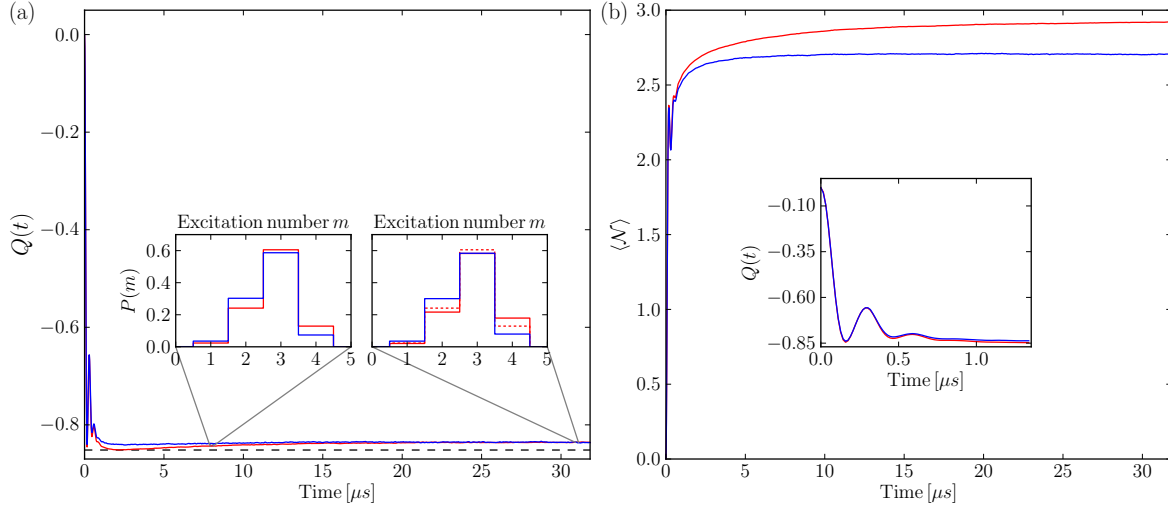
Figure 5.7: Time-dependent Q parameter (a) and Rydberg population (b) at resonance ($\Delta = 0$) for both very weak decay $(\Omega, \gamma, \Gamma)/2\pi = (0.8, 0.004, 1)$ (solid, red) and weak decay $(0.8, 0.02, 1)$ (solid, blue). The horizontal, dashed line in (a) is positioned at $\min[Q(t)]$, indicating that Q increases slightly for very weak decay. The insets in (a) show the excitation histograms for the respective curves at times $t = \{8, 31\}\,\mu s$; the red, dashed line in the right inset corresponds to the solid, red line in the left inset. In (b), the inset shows an enlarged detail of $Q(t)$ for small times.

is quantified via the Q_3 parameter

$$Q_3 = \frac{\langle (\mathcal{N} - \langle \mathcal{N} \rangle)^3 \rangle}{\langle \mathcal{N} \rangle} - 1, \tag{5.12}$$

which, as before, is by design zero for Poissonian statistics.

By means of these parameters, in particular the Q parameter, the excitation statistics is commonly studied (cf., for example, Refs. [4, 17, 40]), usually as a function of the detuning or the density. In contrast, we focus on the dynamics of the Q value for a fixed detuning as well as a fixed line density of 2.67×10^4 cm^{-1} ($N = 40$ atoms randomly placed in a one-dimensional trap of length $L_{1D} = 15\,\mu m$). The (repulsive) van der Waals interaction by which the Rydberg excitations interact is given by $C_6/2\pi = 16\,000$, corresponding to the $|50S_{1/2}\rangle$ state of Rb [54].

Comparing the Q parameter on resonance ($\Delta = 0$) for two different decay rates ($\gamma/2\pi = 0.004$ and $\gamma/2\pi = 0.02$, respectively) and a fixed dephasing constant of $\Gamma/2\pi = 1$, we find interesting dynamical features shown in Figure 5.7. Specifically, Figure 5.7a shows that the Q parameter first drops rapidly below zero but subsequently increases for very weak decay ($\gamma/2\pi = 0.004$).

The first observation can be readily understood by the blockade effect, which reduces the excitation number fluctuation since only a rather well-defined number of excitations fits in the excitation volume [87]. The increase of Q, conversely, is a dynamical effect rooted in equilibration dynamics. That is, for very weak decay and nonzero dephasing, the Rydberg population reaches its steady-state value only in the limit of large times (cf. Figure 5.7b), implicating a (slight) increase in higher excitation numbers at large times. Considering the two insets in Figure 5.7a, notably the right one, and comparing the solid, red ($t = 31\,\mu s$) and dashed, red ($t = 8\,\mu s$) histograms, one observes that the histogram at $t = 31\,\mu s$ is slightly shifted towards higher excitation numbers, increasing the excitation number fluctuation quantified by the Q parameter.

The observed increase requires extremely weak decay, such that the Rydberg population equilibrates very slowly, since for a larger decay constant of $\gamma/2\pi = 0.02$ the Rydberg population equilibrates much faster (cf. Figure 5.7b, blue curve), which is also reflected in the
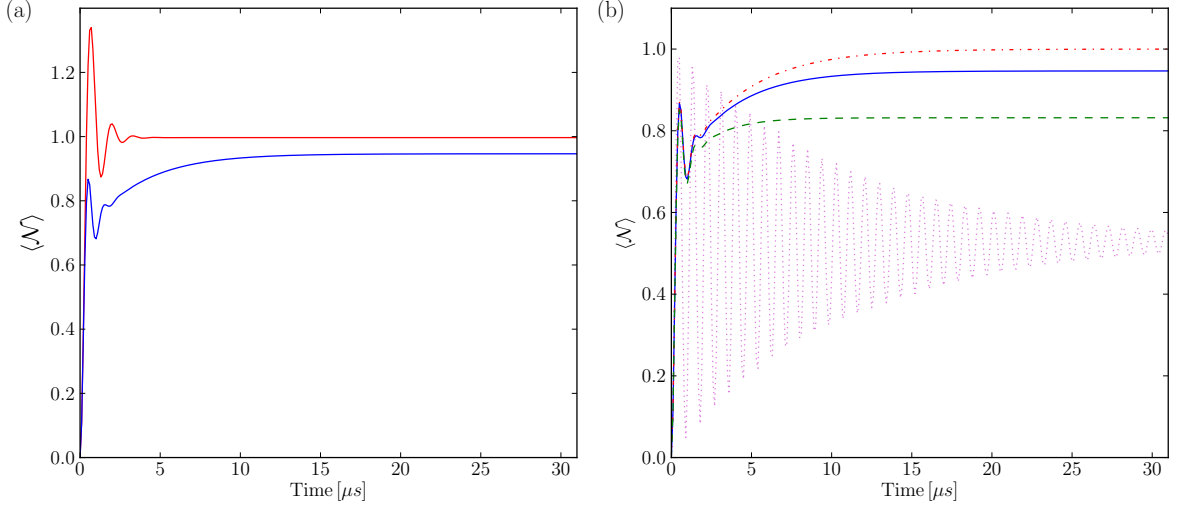
Figure 5.8: Time-dependent Rydberg population for a simple two-atom master equation simulation on resonance using $(\Omega, \Gamma)/2\pi = (0.8, 1)$. In (a), the population is shown for different interaction strengths, $\mathcal{V}_{rr} = 0$ (red) and $\mathcal{V}_{rr}/2\pi = 3$ (blue) for very weak decay ($\gamma/2\pi = 0.004$). In (b), the interaction strength is held fixed at $\mathcal{V}_{rr}/2\pi = 3$ and the decay constant is varied. The different lines correspond to $\gamma = 0$ (red, dash-dotted), $\gamma/2\pi = 0.004$ (blue, solid) and $\gamma/2\pi = 0.02$ (green, dashed). The dotted, magenta line indicates the Rydberg population for zero dephasing, $(\gamma, \Gamma)/2\pi = (0.02, 0)$.

Q parameter (cf. Figure 5.7a, blue curve). The oscillations in $Q(t)$ at small times (cf. inset in Figure 5.7b) are due to the Rabi oscillations in the Rydberg population.

The slow equilibration time scale can be traced back to the Rydberg interaction, which, in combination with a large dephasing, induces slow equilibration, as has been already noted in Figure 4.3b and the corresponding discussion in the main text. A more rigorous analysis of a simple system consisting of two atoms, however, is shown in Figure 5.8.

Comparing the two lines in Figure 5.8a, we immediately see that nonzero interaction is crucial for slow equilibration in the dissipative regime, i.e., independent atoms equilibrate fast for sufficiently large dephasing. For a fixed interaction strength $\mathcal{V}_{rr}/2\pi = 3$, the equilibration time scale for large dephasing is basically given by the decay constant, as illustrated in Figure 5.8b. While for $\gamma/2\pi = 0.02$ the steady state is already reached at $t \approx 8\,\mu s$, it takes $t \approx 18\,\mu s$ if no decay is present.

The impact of dephasing on the Rydberg population of an interacting system can also be deduced from Figure 5.8b, notably from the comparison of the the dotted, magenta line showing damped oscillations obtained for $(\gamma, \Gamma)/2\pi = (0.02, 0)$ with the red, dash-dotted line obtained for $(\gamma, \Gamma)/2\pi = (0, 1)$. Being far detuned, the doubly excited state is hardly populated for zero dephasing, and the population, which features coherent oscillations at small times, further decreases due to nonzero decay of the Rydberg state until it reaches its steady-state value

$$\lim_{\Gamma \to 0} \langle \mathcal{N}^{(1)} \mathcal{N}^{(2)} \rangle \Big|_{t \to \infty} = \frac{\Omega^4}{(\gamma^2 + 2\Omega^2)^2 + \mathcal{V}_{rr}^2(\gamma^2 + 4\Omega^2)} \xrightarrow{\mathcal{V}_{rr} \gg \Omega} 0. \tag{5.13}$$

For large dephasing and small decay (both compared to the Rabi frequency), conversely, the population of the doubly excited state increases significantly over time, reaching its steady-state value

$$\lim_{\gamma \to 0} \langle \mathcal{N}^{(1)} \mathcal{N}^{(2)} \rangle \Big|_{t \to \infty} = \frac{1}{4} \tag{5.14}$$
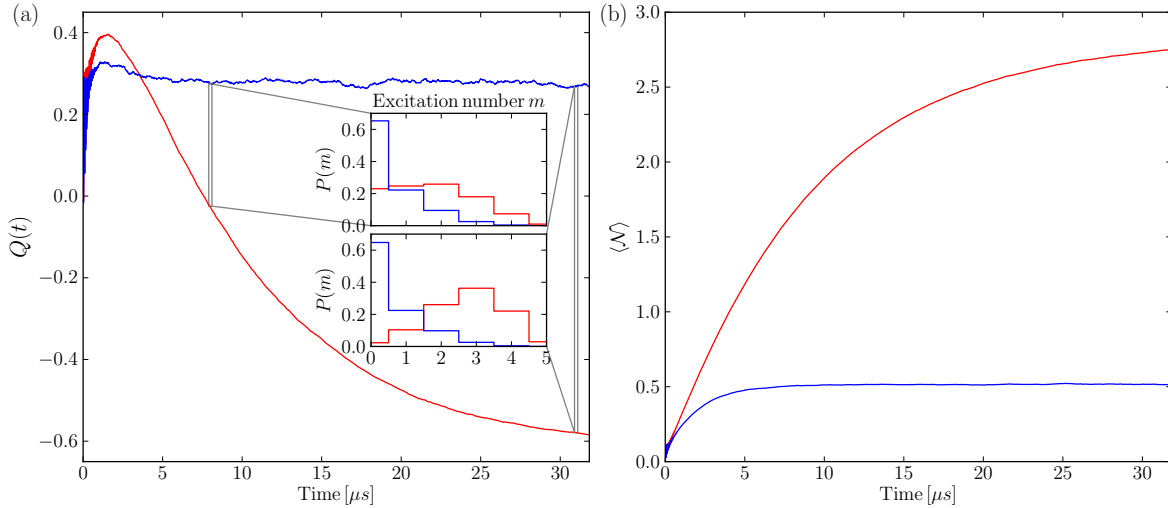
Figure 5.9: Time-dependent off-resonant ($\Delta/2\pi = 15$) Q parameter (a) and Rydberg population (b) for very weak Rydberg decay $(\Omega, \gamma, \Gamma)/2\pi = (0.8, 0.004, 1)$ (solid, red) and intermediate decay $(0.8, 0.1, 1)$ (solid, blue). The insets in (a) show the excitation histograms at two times, $t = \{8, 31\}\,\mu s$ for both decay constants.

only in the limit of large times. For zero decay and strong interaction, $\mathcal{V}_{rr} \gg \Omega$, the steady state of the system is only reached in the limit of infinite times, $t \to \infty$. Eq. (5.14) can be understood via symmetry arguments: In the absence of decay, there is no particular direction due to the absence of a distinct lower state, so in equilibrium, all states are equally populated. This is simply the detailed balance condition discussed in Section 5.1. Decay conversely breaks the symmetry and imposes a particular direction towards the ground state of the system, reducing the population of the doubly excited state in equilibrium and imposing the equilibration time scale for sufficiently large values.

With this in mind, we conclude that the slow dynamics for zero decay is due to the slow time scale associated with the equilibration of the far-detuned excited state(s), which can be shifted off resonance by both laser-detuning and Rydberg interaction. Nonzero dephasing, in turn, is necessary to guarantee convergence to the steady state; for zero dephasing, the system needs to be prepared in a configuration with all states equally populated in order to feature a time-independent solution. For nonzero decay, the equilibration time scale is basically given by the shorter of the two time scales associated with off-resonant excitation and decay of the excited state respectively, as — in a classical model — discussed below. Hence, the equilibration dynamics can be well understood on the basis of a two-atom system.

Returning to the many-body case, we can summarize that for interacting systems in the dissipative regime the slow equilibration time scale leads to non-trivial dynamics of the Q parameter. As a matter of fact, this does not only hold true for resonant, but also for off-resonant excitation.

Indeed, for off-resonant excitation ($\Delta/2\pi = 15$) the dynamics of the Q parameter shown in Figure 5.9 is even more remarkable as the Rydberg population increases considerably up to large times (cf. Figure 5.9b). As a consequence of the excitation histogram as a whole shifting towards higher excitation numbers, the Q parameter decreases strongly after having reached its (positive) maximum at $t \approx 1.6$. These dynamics are a consequence of "slow resonant effects": Due to the large detuning, the excitation of a single atom is — in classical terms — very unlikely, happening only on a large time scale. Resonant excitation can occur on smaller time scales, yet requiring well-defined inter-atomic separation, which is not always provided in a small trap, leading to an overall slow population increase.

In a simple single-atom two-level rate equation obtained by eliminating the atomic coherences

(cf. Section 3.1), the off-resonant excitation rate is given by

$$\gamma_{\uparrow,\text{offres}} = \frac{\Omega^2(\gamma + \Gamma)}{4\Delta_{\text{eff}}^2 + (\gamma + \Gamma)^2} \xrightarrow{\Delta_{\text{eff}} \gg \Gamma, \gamma} \frac{\Omega^2(\gamma + \Gamma)}{4\Delta_{\text{eff}}^2} \, , \tag{5.15}$$

while the resonant excitation rate reads

$$\gamma_{\uparrow,\text{res}} = \frac{\Omega^2(\gamma + \Gamma)}{(\gamma + \Gamma)^2} \xrightarrow{\Gamma \gg \gamma} \frac{\Omega^2}{\Gamma} \, , \tag{5.16}$$

being much larger than the off-resonant excitation rate (5.15) for large Δ_{eff}. Thus, initial off-resonant excitation followed by resonant excitation results in slow population increase in the classical model, as the first excitation occurs on a large time scale and not all subsequent excitations fulfill the exact resonance conditions but are detuned by an effective detuning (including the Rydberg interaction) $\Delta_{\text{eff}}/2\pi < 15$. The de-excitation rate, conversely, is simply $\gamma_{\downarrow} = \gamma_{\uparrow} + \gamma$, indicating that the equilibration time scale results from the interplay of (off-resonant) excitation and atomic decay.

The simple classical model given above is only valid, however, if two-photon processes can safely be neglected. Examining the pair correlation function $G^{(2)}$, we find that for very weak decay single-photon and two-photon excitations contribute almost equally to resonant excitations whereas for intermediate decay the single-photon contribution dominates over the two-photon contribution. This observation is consistent with the conclusions drawn from Figure 5.9 since coherent two-photon processes typically occur on a larger time scale than single-photon processes, given by the effective two-photon Rabi frequency $\Omega_{\text{eff}} = \Omega^2/\Delta$ with Δ being the detuning of the singly excited state (cf. Section 5.4). Accordingly, the classical model is not fully appropriate for quantitative discussion, but taking into account slow coherent double-excitation processes does not alter the "slow resonant excitation" picture established above.

For intermediate decay ($\gamma/2\pi = 0.1$), the equilibration time scale is much smaller (cf. Figure 5.9b); the atomic decay competes with the slow excitation process, yielding a broad excitation histogram with dominant ground state contribution and consequently a super-Poissonian Q value (cf. Figure 5.9a). In simple terms, as soon as the decay constant dominates over the slow time scale of the excitation processes, the equilibration time scale is imposed by the inverse of the decay constant, trapping a substantial fraction of the Rydberg population in the ground state. In a classical model, the equilibration time scale is given by $\min\{1/\gamma, 4\Delta_{\text{eff}}^2/\Omega^2(\gamma + \Gamma)\}$.

In a nutshell, for far off-resonant and incoherent ($\Gamma > 0$) excitation, appreciable atomic decay, competing with the slow excitation processes, leads to fast equilibration and broad excitation histograms featuring a positive Q value even at large times. Negligible decay, in contrast, implies slow equilibration, entailing a strong decrease of the Q value after initial increase, reaching significant negative values at large times. These particular dynamics can be attributed to resonant effects, which first give rise to super-Poissonian Q values via broad excitation histograms and subsequently sub-Poissonian Q values as the excitation histograms shift towards and peak at higher excitation numbers. This shows that the precise value of the Rydberg decay can be crucial for the long-time properties in the far blue detuned case. Note that, for larger system sizes, our observation $Q > 0$ for intermediate decay constants might not necessarily hold true any more, but distinct differences in the dynamics for small and intermediate decay, respectively, are still expected to emerge, due to the different equilibration time scales present in the systems.

Finally, we consider off-resonant excitation in the weakly dissipative regime, i.e., $\Delta/2\pi = 5$, $\Gamma = 0$ and $\gamma/2\pi = 0.005$. In this regime, bimodal excitation histograms can be observed even
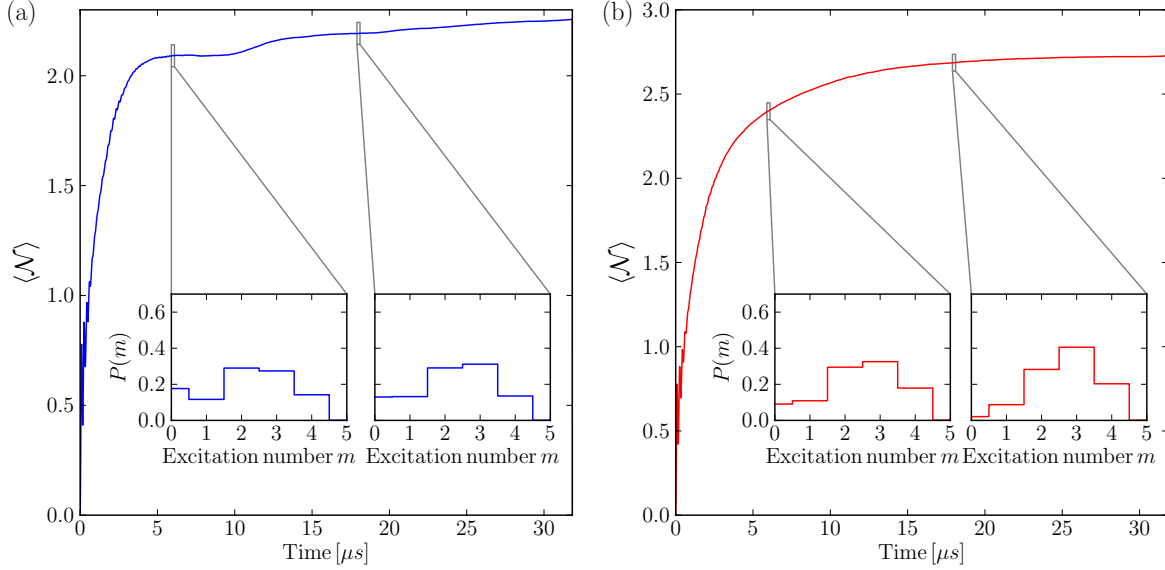
Figure 5.10: Time-dependent off-resonant ($\Delta/2\pi = 5$) Rydberg population for two different dephasing constants, $(\Omega, \gamma, \Gamma)/2\pi = (0.8, 0.005, 0)$ (a) and $(0.8, 0.005, 0.05)$ (b). The insets show the excitation histograms at two times, $t = \{6, 18\}\,\mu s$.

at rather large times $t = 6\,\mu s$ (cf. left inset in Figure 5.10a).

Before studying in detail the reasons for this bimodality, we first note that it is *a)* a transient effect which *b)* requires strong coherence ($\Gamma \approx 0$). This can be directly seen from Figure 5.10: While for $\Gamma = 0$ the excitation histogram displays bimodality at $t = 6\,\mu s$, this feature is lost at larger times. Furthermore, for $\Gamma/2\pi = 0.05$ the ground state is already strongly depopulated at $t = 6\,\mu s$, such that no bimodal feature can be observed anymore (cf. Figure 5.10b).

The striking feature of the bimodality shown in Figure 5.10 is that it is visible for a small detuning at rather large times, while a bimodality stemming from the fact that resonant processes depopulate the ground state on a faster time scale than the one by which it loses population via off-resonant excitation (cf. Section 6.4) would, for a small detuning, be expected to be visible only at small times. The reason for this is that the off-resonant excitation rate for a small detuning is rather large, such that the population quickly escapes the ground state. As a matter of fact, our explanation must not involve classical terms as we consider a rather coherent system ($\Gamma = 0$, $\gamma \ll \Omega$). Instead, we need to have a closer look at the different geometrical realizations underlying the population average.

This is done in Figure 5.11, which shows the time-dependent Rydberg population for two different geometrical realizations. In Figure 5.11a, a realization with a small density of excited states (i.e., a small state space) is shown, whereas Figure 5.11b shows a realization for a large density of excited states corresponding to a state space consisting of many states, which is also reflected in the larger mean Rydberg population. Considering the excitation histograms at different times, one observes strong fluctuations in the excitation statistics, associated with the collective Rabi oscillations between ground and doubly-excited Rydberg state.

Thus, we attribute the bimodality observed in Figure 5.10 to both finite-size as well as dynamical effects. That is, in a geometrical configuration in which only a small density of excited states exist, only few pairs feature a inter-atomic separation which approximately corresponds to the resonant distance. These pairs can oscillate coherently, leading to strong oscillations in the total Rydberg population between the ground and doubly-excited state, $m = 0 \leftrightarrow m = 2$. These oscillations constitute the transient nature of the bimodality. For a configuration with a large density of excited states, more pairs separated by approximately the resonant distance exist, leading to oscillations which dephase more quickly. This is what
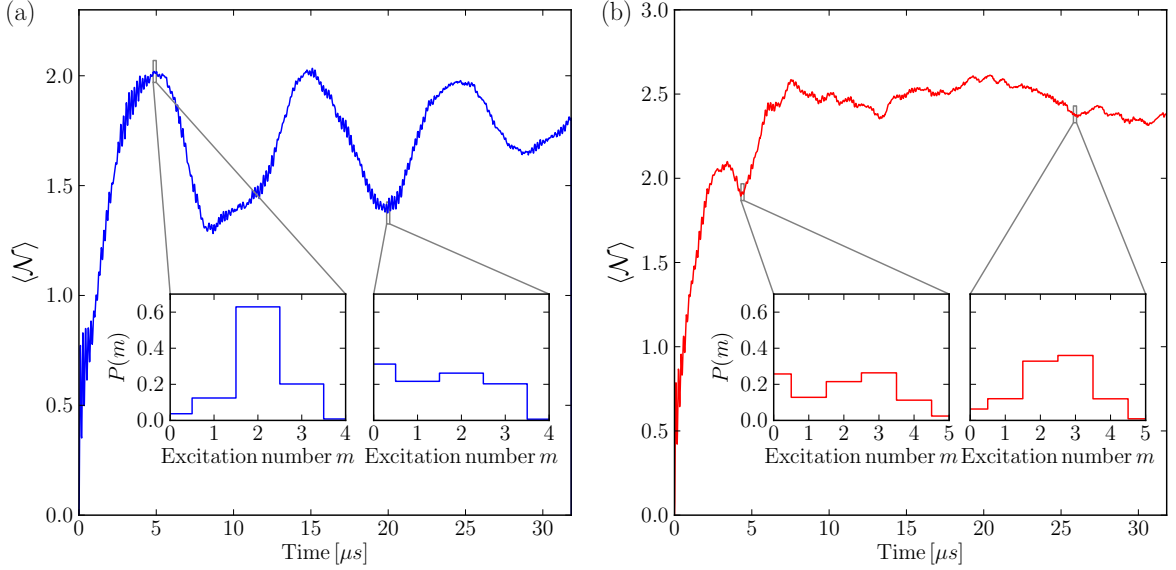
Figure 5.11: Time-dependent off-resonant ($\Delta/2\pi = 5$) Rydberg population for two different geometries, notably a geometry with small density of excited states (a) and a geometry with large density of excited states (b). The insets show the excitation histograms at two times, $t = \{4.9, 20\} \, \mu s$ in (a) and $t = \{4.4, 25.9\} \, \mu s$ in (b).

we refer to as finite-size effect, as the dephasing time scale depends strongly on the number of excited pairs, i.e., the density of excited states, which is limited by the system size.

In conclusion, averaging over various different geometrical realizations yields a bimodal excitation histogram up to times $t = 6 \, \mu s$ in the approximately coherent regime ($\Gamma = 0$, $\gamma \ll \Omega$) for the considered sample. This bimodality is due to both finite-size and dynamical effects. Dynamical in the sense that the average over oscillating Rydberg pairs with distinct frequencies (depending on how precisely the resonant distance is realized) yields an excitation histogram with non-negligible ground state population even at larger times. The reason for such oscillations being visible is given by finite-size effects, which limit the total number of excitations, thereby allowing for oscillations that re-populate the ground state as well as clearly visible oscillations which are not smeared out by the superposition of various frequencies. For larger systems, these oscillations are not expected to be visible but smeared out by natural dephasing; dynamical effects, in turn, are expected to involve only higher excited states at larger times rather than the ground state.

6 Rate Equation Results

In this chapter, we discuss simulations performed for the the experimental setup[15] of Ref. [4], using the rate equation introduced in Section 3.1. We start off by describing the experimental setup as well as the relevant simulation parameters in Section 6.1 and subsequently explain some details of the implementation of the kinetic Monte Carlo algorithm (cf. Section 3.1) in Section 6.2. In Section 6.3, the simulation results are discussed, whereupon the pertinent interpretation is given in Section 6.4, stemming from thorough analysis of the numerical data. Finally, the benchmark of the kMC rate equation model using the wave function Monte Carlo technique is discussed for the parameters of the preceding simulations in Section 6.5.

We find that the asymmetry of the excitation spectra as well as the super-Poissonian Mandel Q values for positive detunings can be assigned to resonant processes which lead to aggregate formation subsequent to initial seeding on a much faster time scale than the initial seeding process. Benchmark simulations comparing wave function Monte Carlo (MCWF) with rate equation results show good agreement for the considered parameter regime.

6.1 Experimental Setup

The experimental setup on which our simulations are based is the setup of Ref. [4]. Specifically, we consider ^{87}Rb atoms that are excited to the $|50S_{1/2}\rangle$ Rydberg state from the ground state $|5S_{1/2}, F = 2, m_F = 2\rangle$ via two step excitation scheme involving the intermediate state $|5P_{3/2}, F = 3, m_F = 3\rangle$. The laser that drives the lower transition with $\Omega_{12}/2\pi \simeq 8$ uniformly illuminates the cloud while the second laser with $\Omega_{23,0}/2\pi \simeq 6.7$ is focused to an elliptical region of size $19\,\mu m \times 7.5\,\mu m$ (vertical $\times$ horizontal Gaussian $e^{-1/2}$ beam radii). To reduce the effect of the intermediate state on the system dynamics, the lower transition is red-detuned by $\Delta_1/2\pi = 65$. The Rydberg and the intermediate state decay with decay constants $\gamma_{32} \simeq 0.025$ and $\gamma_{21}/2\pi \simeq 6.07$, respectively.

Due to finite laser linewidth, the system undergoes dephasing of type (2.24), with the dephasing rates given by $\Gamma_{32}/2\pi \simeq 0.7$, $\Gamma_{21}/2\pi \simeq 0.33$ and $\Gamma_{31}/2\pi = (\Gamma_{32} + \Gamma_{21})/2\pi \simeq 1.03$. The Rydberg states interact repulsively via van der Waals interaction quantified by the coefficient $C_6/2\pi \simeq 16\,000$ [54]. All measurements are taken after an excitation time of $t = 5\,\mu s$.

The trap in which the atoms are loaded is an optical dipole trap of cigar shape with $e^{-1/2}$ radii of $\approx 1.65\,\mu m$ (radial) and $\approx 240\,\mu m$ (axial, horizontal), providing a quasi one-dimensional geometry.

Due to the uncertainties with respect to the radial size of the cloud caused by finite optical resolution as well as with respect to the Rabi frequency driving the lower transition, the numbers given above are to be taken as 'best fit' parameters, which we plugged into our model to theoretically investigate the dynamics arising therein.

For the simulation, the parameters stated above are plugged into the rates for the kinetic Monte Carlo algorithm that have been calculated analytically. For the upper transition, the non-uniform Rabi frequency is taken into account via the spatially varying Rabi frequency
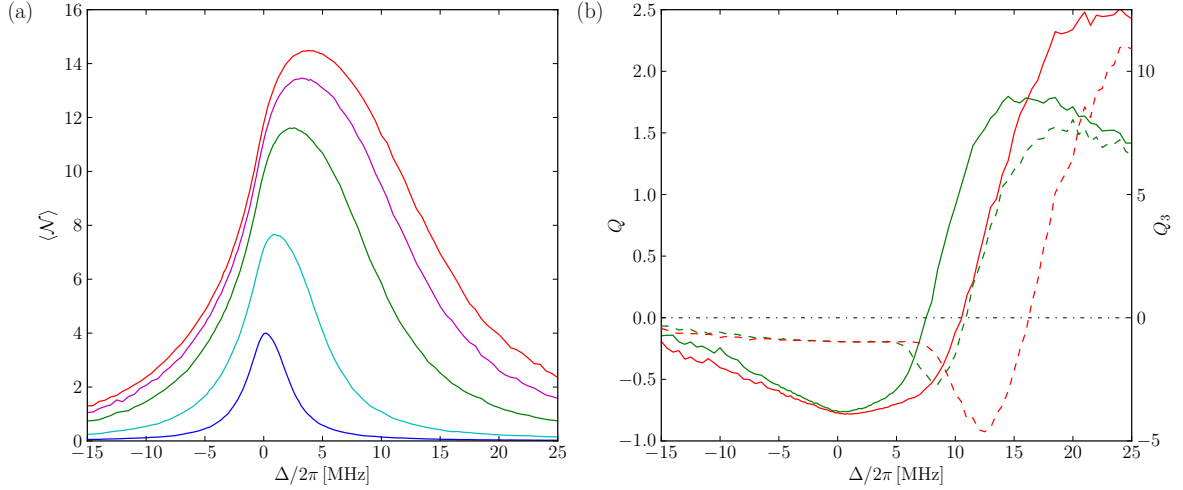
$$\Omega_{23}(x, z) = \Omega_{23,0} \exp\left(-\frac{x^2}{2\sigma_{x'}^2} - \frac{z^2}{2\sigma_{z'}^2}\right), \tag{6.1}$$

with the x axis aligned along the direction of largest extension of the cloud (horizontal), the y

---

Figure 6.1: (a) Rydberg excitation spectrum for different densities: $5 \times 10^{10} \, \text{cm}^{-3}$ (blue), $2 \times 10^{11} \, \text{cm}^{-3}$ (cyan), $8 \times 10^{11} \, \text{cm}^{-3}$ (green), $1.2 \times 10^{12} \, \text{cm}^{-3}$ (magenta) and $1.5 \times 10^{12} \, \text{cm}^{-3}$ (red). In (b), Q (solid) and Q_3 (dashed) values are shown for the two the corresponding densities $8 \times 10^{11} \, \text{cm}^{-3}$ (green) and $1.5 \times 10^{12} \, \text{cm}^{-3}$ (red). The dash-dotted line in (b) indicates Poissonian statistics where $Q = Q_3 = 0$.

axis aligned along the propagation direction of the laser and the z axis aligned perpendicular to both (vertical). In Eq. (6.1), $\sigma_{x'}$ and $\sigma_{z'}$ are given by $19 \, \mu m$ and $7.5 \, \mu m$, respectively, as mentioned above.

6.2 Computational Implementation

Starting from Algorithm 1, some extensions, specifications and improvements are necessary to facilitate an efficient calculation of the experimental setup described in Section 6.1.

Firstly, the simulation is significantly sped up if the effective detuning is not calculated anew for each time step in the kMC algorithm, but only updated after each system change [55]. As all atoms start in the ground state, the effective detuning is, for the first run, given by the two-photon detuning; subsequent excitations and de-excitations of atoms then modify the effective detuning, which can be efficiently stored in an array and updated after each system change. Implementing the storage of the effective detuning and calculating in addition the (de-)excitation rates by means of inline functions using the optimized GSL power routines `gsl_pow_n(x)` [88] for the nth power of `x`, an efficient simulation of several hundreds of atoms is rendered possible.

Further speedup is obtained by trivial parallelization, i.e., running the same simulation with less statistics on several kernels and combining the simulation results in the end. While observables such as the Rydberg population and the excitation histograms can be simply averaged, observables such as the pair correlation function $G^{(2)}$ or the Q parameter require separate averaging of the numerator and denominator in principle to yield the correct result. It is only in the limit of good statistics for each individual calculation (i.e., when the population average $\langle \mathcal{N} \rangle$ is already converged) that observables such as Q or Q_3 can be directly averaged.

Secondly, the precise experimental geometry is implemented computationally efficiently by using the trap parameters to sample the positions of the atoms utilizing the GSL routine `gsl_ran_gaussian`, but only keeping the atoms that lie inside the laser spot $2\sigma_{x'} \times 2\sigma_{z'}$ for the simulation. Thereby, the number of simulated atoms is significantly reduced. For the highest considered density of $1.5 \times 10^{12} \, \text{cm}^{-3}$, ≈ 750 atoms lie inside the laser spot volume given by $2\sigma_{x'} \times 2\sigma_{z'}$, whereas $\approx 15\,000$ atoms are contained inside the total trap volume. By
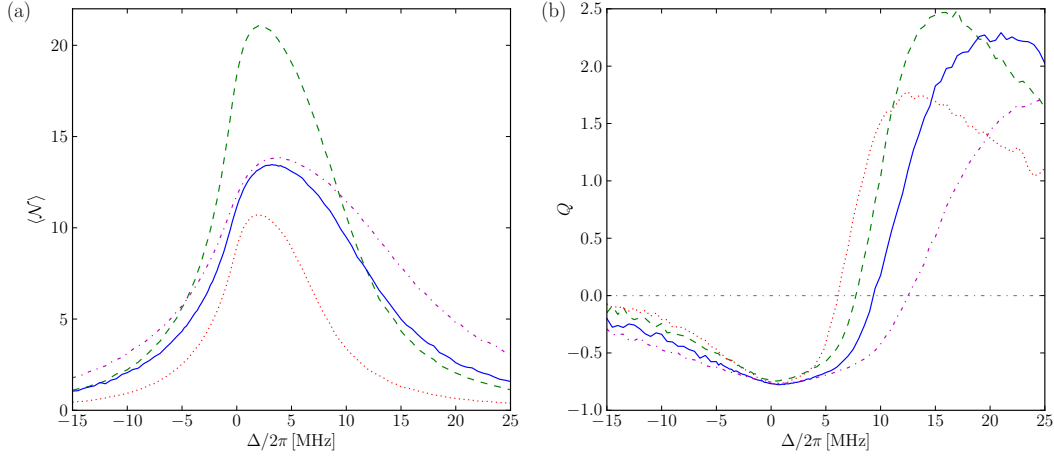
Figure 6.2: Rydberg population (a) and Mandel Q parameter (b) as a function of the laser detuning. The solid, blue line is identical to the magenta one in Figure 6.1. The dotted, red line is obtained for $\Omega_{12}/2\pi = 5$, the dash-dotted, magenta line for approximately doubled dephasing constants and the dashed, green line for an enhanced radial trap size $\sigma_{r'} = 2.5$ while holding the total number of atoms constant, corresponding to a density of $0.5 \times 10^{12}\,\mathrm{cm}^{-3}$. All other parameters are identical to the ones in Figure 6.1.

increasing the spot size to $3 \times \{\sigma_{x'}, \sigma_{z'}\}$ while holding the density constant, it was verified that our simulation results are converged with respect to a further increase of the simulated excitation volume.

6.3 Simulation Results

For different atomic densities, the Rydberg population is plotted in Figure 6.1a. With increasing density the maximum of the excitation probability shifts towards positive detuning values and the excitation spectrum becomes increasingly asymmetric. In Figure 6.1b, the higher moments Q and Q_3 defined in Eqs. (5.11), (5.12) are shown as a function of the detuning. Around the resonance $\Delta = 0$, the Q value is clearly negative, indicating sub-Poissonian excitation statistics induced by the Rydberg blockade [17]. For positive detuning values, the Q value rapidly increases, reaching values as high as 2.5 for the highest density $1.5 \times 10^{12}\,\mathrm{cm}^{-3}$. This super-Poissonian behavior points to enhanced fluctuations in the excitation statistics. Similar behavior is found for the Q_3 value. Interestingly, the Q value decreases for the intermediate density $8 \times 10^{11}\,\mathrm{cm}^{-3}$ for large detunings after having reached its maximum around $\Delta/2\pi \simeq 15$.

In Figure 6.2, the impact of the variation of the lower Rabi frequency Ω_{12}, the dephasing and the radial trap size on the excitation spectrum as well as the Mandel Q parameter is shown. While the increase of the radial trap size (implying an effective decrease in density) leads to a narrower excitation spectrum with larger peak population as well as narrower Q parameter, an increased dephasing broadens both excitation spectrum and Q parameter, with the broadening affecting the blue side of the spectrum somewhat stronger than the red side. A decrease of the Rabi frequency yields a reduced and less asymmetric excitation spectrum and, accordingly, a Q parameter that decreases for large detunings, indicating that slow off-resonant excitations (and not resonance effects) dominate the dynamics at large values of Δ.

Before discussing the behavior of the Q parameter in more detail, we note that both Q and Q_3 quantify higher moments of the full counting statistics, i.e., the excitation histograms measured in the simulation. They provide measures to estimate the deviation of the simulated excitation histograms from Poissonian statistics, i.e., totally uncorrelated excitation statistics.
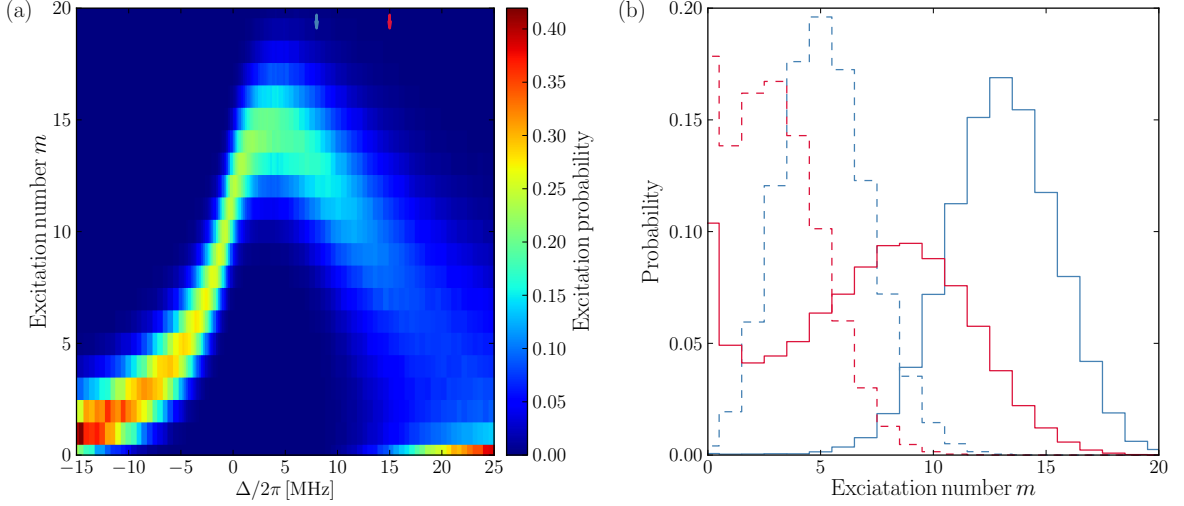
Figure 6.3: (a) Full Rydberg excitation histograms for the highest density $1.5 \times 10^{12} \, \mathrm{cm}^{-3}$. The steel blue and crimson arrows indicate the detuning values $\Delta/2\pi = 8$ and $\Delta/2\pi = 15$, respectively, for which the corresponding histograms are plotted in (b). The dashed lines indicate the same histograms, but convoluted with a finite detection efficiency of $\eta = 0.4$.

The higher the order of the moment calculated, the better measurement statistics is required to allow for a significant statement. Moreover, a real measurement is always complicated by the finite detection efficiency of the detector, i.e., in real experiments, only a fraction of the total Rydberg excitation is detected. For the experiments of Ref. [4], the detection efficiency is $\eta \simeq 0.4$. On that account, to make simulation results comparable, the simulation data with flawless detection needs to be convoluted with the finite detection efficiency according to [4]

$$P_\eta(m) = \sum_{m' \geq m} \binom{m'}{m} \eta^m (1-\eta)^{m'-m} P(m'), \tag{6.2}$$

where $P_\eta(m)$ is the measured probability to detect m excitations taking into account the finite detection efficiency η and $P(m')$ is the true probability to find m excitations.

With this in mind, we can turn to Figure 6.3, which shows excitation histograms for the highest density $1.5 \times 10^{12} \, \mathrm{cm}^{-3}$. In Figure 6.3a, the excitation histograms are plotted for the whole range of simulated detuning values, nicely showing the anti-bunching of excitations around resonance while enhanced fluctuations for positive detuning values. The two arrows in the top part of the figure mark the detuning values for which the histograms are shown as a vertical slice in Figure 6.3b in the corresponding colors. In Figure 6.3b, the dashed lines indicate the histograms convoluted with the finite detection efficiency η according to Eq. (6.2). As expected, the features of the histograms, namely the bimodality observed for $\Delta/2\pi = 15$, get blurred and the maximal excitation number shifts towards smaller values.

6.4 Unraveling the Aggregate Formation Mechanism

While the sub-Poissonian Q value around resonance is well understood in terms of the Rydberg blockade, the reason for the super-Poissonian Q is not so obvious at first glance. Certainly, the enhanced fluctuations can be attributed to resonant effects, but the precise mechanism of these fluctuations has yet to be analyzed.

Therefore, we first rule out that the fluctuations in the excitation number are caused by averaging over different geometrical configurations that have different excitation properties. Simulating for a low density several fixed, random geometries for various detuning values, we
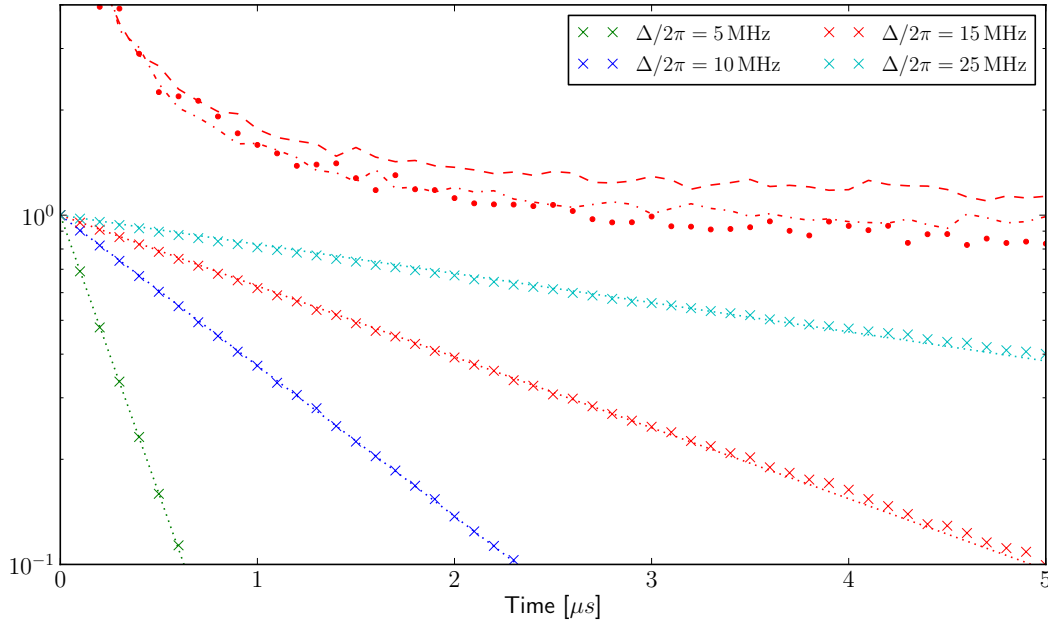
Figure 6.4: Time evolution of the populations of the different excitation number subspaces $P(m)$ with m excitations. The four curves (crosses) in the lower part of the figure show the time evolution of the zero excitation subspace $P(0)$ for different detunings $\Delta/2\pi = 5, 10, 15, 25$, from bottom to top. The data points obtained from the rate equation model are overlaid with an exponential fit. The three curves (dashed, dash-dotted, dotted) in the upper half of the figure show the time evolution of ratios $P(m)/P(m+1)$ of excitation probabilities of adjacent subspaces for $m \in \{1, 2, 3\}$. From top to bottom, ratios with increasing m are shown.

checked that all different geometrical realizations show the same Q parameter behavior with very small fluctuations between the distinct geometries.

Focusing now on the dynamical aspect of the excitation, we start by analyzing how the rate equation simulation is performed in order to subsequently carve out the physics that is incorporated therein.

At the beginning of the simulation, all atoms are in the ground state, so the total rate for an excitation to happen is strongly suppressed by a large detuning. Consequently, for large detunings the first excitation occurs on average at larger times. This is illustrated in Figure 6.4 where the probability of the ground state $P(0)$ is, on a logarithmic scale, plotted for different detuning values in the lower part of the figure. As the detuning increases, the excitation dynamics slow down, with the ground state probability $P(0)$ dropping exponentially as $e^{-t/\tau}$ for small times. The decay constant τ can be determined via an exponential fit and scales approximately as Δ^2. To leading order, this scaling can be also verified by expanding the excitation rate $\gamma_\uparrow$ to second order in the master equation parameters. Neglecting two-photon processes for the moment, the slowdown of the excitation dynamics can be easily understood by noting that the energy gap between the ground state and any singly excited state increases with the detuning. Two-photon processes in turn exhibit dynamics given by the effective Rabi frequency Ω^2/Δ, which also slows down with increasing detuning.

The upper half of Figure 6.4 shows the ratios $P(m)/P(m+1)$ for $m \in \{1, 2, 3\}$. Initially, the ratios are large as the probability to find higher excited states is small, but the ratios converge rather rapidly to a stationary value, indicating that the process $m \leftrightarrow m+1$ ($m \neq 0$) is much faster than the process $0 \to 1$. The reason for this is that only the first excitation is off-resonant, while subsequent excitations are prevalent (nearly) resonant and thus occur on a much faster time scale than the first excitation, leading to a rapid equilibration when
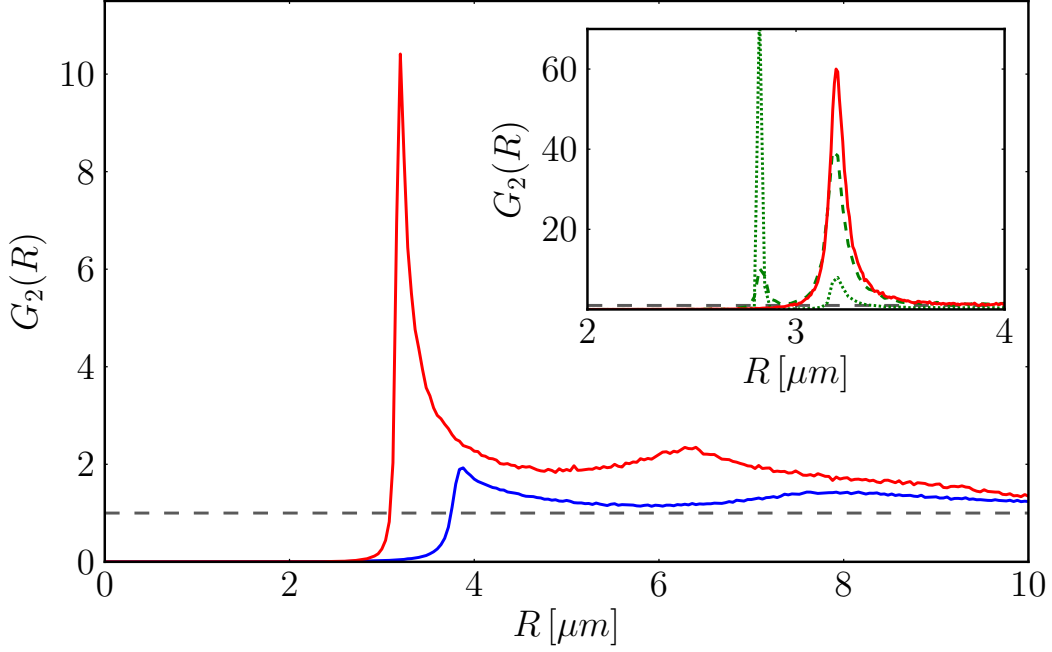
Figure 6.5: Pair correlation functions $G^{(2)}(R)$ for $\Delta/2\pi = 5$ (blue) and $\Delta/2\pi = 15$ (red). The inset shows MCWF simulations for $\Delta/2\pi = 15$ with dephasing rates $\Gamma = 0$ (green, dotted) and $\Gamma/2\pi = 1$ (green, dashed), compared to the rate equation simulation with $\Gamma/2\pi = 1$ (red, solid). To improve visibility, the dotted curve is scaled by a factor of $1/10$.

compared to the time scale of the initial excitation. These (nearly) resonant processes are single-photon resonance processes which arise when the energy shift induced by an additional Rydberg excitation in the vicinity of the first excitation is (approximately) compensated by the detuning. The presence of two distinct time scales, specifically the slow time scale for the formation of the seed excitation and the fast time scale for subsequent growth, results in enhanced excitation number fluctuations that manifest themselves in an increased Q parameter value.

It should be noted, however, that the mechanism just explained, namely the subsequent-growth-after-initial-seed mechanism is inherent in the rate equation model which explicitly excludes other kinds of excitation schemes such as two-photon processes. The claim is not that since we understand our relatively simple model we can deduce the precise excitation mechanism; the claim is that, since our simulations seem to be very well applicable in the parameter range considered (cf. Section 6.5), we have good grounds to trust the mechanism inherent in our model to be physically relevant. Hence, the features exhibited by the kMC method are rooted in physical arguments such as the availability of resonant pairs, even if they express themselves via properties of the model.

The attribution of enhanced excitation fluctuations resulting in a large Q value to (single-photon) resonance effects is also supported by the pair correlation function $G^{(2)}(R)$, which can be calculated in the numerical simulations. In Figure 6.5, $G^{(2)}(R)$ is shown for two detuning values, $\Delta/2\pi = 5$ and $\Delta/2\pi = 15$, for the highest considered density. With increasing detuning, the peak at the single-photon resonance position $R_\gamma = (C_6/\Delta)^{1/6}$ becomes more pronounced, giving rise to an enhanced excitation fluctuation since the more atoms are excited in a well-defined distance, the larger the fluctuation in the Rydberg population can become. In fact, for a homogeneous and isotropic system, the Q parameter can be directly related to the integral over the pair correlation function [89]. In the modeled experiments, these assumptions do not apply; nonetheless the relation between Q and the pair correlation function supports consulting $G^{(2)}$ to infer information on the physical origin of the characteristics of the Q

parameter.

The knowledge of the aggregate formation mechanism allows us now to also understand the properties of the Q parameter more properly. The first implication from the previous reasoning is that the Q value is bounded from above by the total number of excitations that fit in the system — and this value depends on the detuning since the resonance distance becomes smaller as the detuning increases. However, also the sharpness of the resonance peak increases for increasing Δ, requiring a large density to allow for a strong impact of resonance effects. For a given (positive) detuning, for instance, the maximal number $m_{\max}$ of excitations that fit in a three-dimensional trap can be estimated by solving $m_{\max} V_s = V_t$ with V_s denoting the volume of a sphere with radius equal to the (single-photon) resonance distance and V_t denoting the trap volume. Consequently, $m_{\max}$ limits the width of the excitation number histogram, thereby imposing an upper bound on the Q parameter. For the simple picture of densely packed spheres to be valid, many atoms need to be separated by the resonance distance for the particular detuning, so a large density is necessitated.

The second implication is that the Q parameter is a dynamic parameter, meaning that as soon as the ground state fraction $P(0)$ is exhausted, the Q value will decrease again[16] as the excitation numbers equilibrate around a steady-state value which corresponds to saturation of the system (neglecting possibly experimentally relevant processes such as collisions, plasma formation etc. which might lead to a re-population of the ground state fraction). Graphically, the excitation histogram for positive detunings starts off by developing a small tail towards multiple excitations, which goes over into an excitation histogram which is rather symmetric around the mean count. Thus, for a system completely characterized by parameters like the ones stated above, the Q value first rises for a fixed, positive detuning and subsequently drops at larger times until it reaches its steady-state value. This is contrary to the observations reported in Ref. [40], where the (excitation number) counting distribution was observed to become more strongly bimodal at larger times.

In the same way, we estimate that the bimodality shown in Figure 6.3b is a transient feature that occurs as the population develops a peak around a certain excitation number for large detunings due to resonance effects, while a considerable fraction of the population is still trapped in the ground state. The visibility of this feature depends on the trap parameters, i.e., density and trap size, in a non-trivial way.

In conclusion, we have found that the super-Poissonian Q parameter in Figure 6.1 can be explained by the resonant excitation dynamics characterized by slow initial seed excitation and fast, resonant subsequent excitations. This very same mechanism also causes a transient bimodality in the exciation number statistics by coupling the ground state preferentially to higher excited state numbers.

6.5 Benchmark Calculations

To benchmark the time-dependent rate equation, we use the two-level wave function Monte Carlo technique developed in Section 3.2 since there are no exact models that allow one to simulate the atom numbers required for realistic modeling. As a benchmark geometry, we choose a cylindrical three-dimensional trap with radius $R = 1.65\,\mu m$ and length $L = 6\,\mu m$, because a one-dimensional system could never feature the nearest neighbor distribution arising in a cigar-shaped trap for realistic densities. In the cylinder, 100 atoms are placed, corresponding to a (homogeneous) density of $\simeq 1.9 \times 10^{12}\,\mathrm{cm}^{-3}$.

To take into account the heterogeneity of the excitation laser driving the upper transition,

---

[16]Strictly speaking, this claim is not bolstered by the data shown here. Though, simulating longer excitation periods using kMC as well as benchmark simulations using the MCWF model support our claim (cf. Section 5.6).
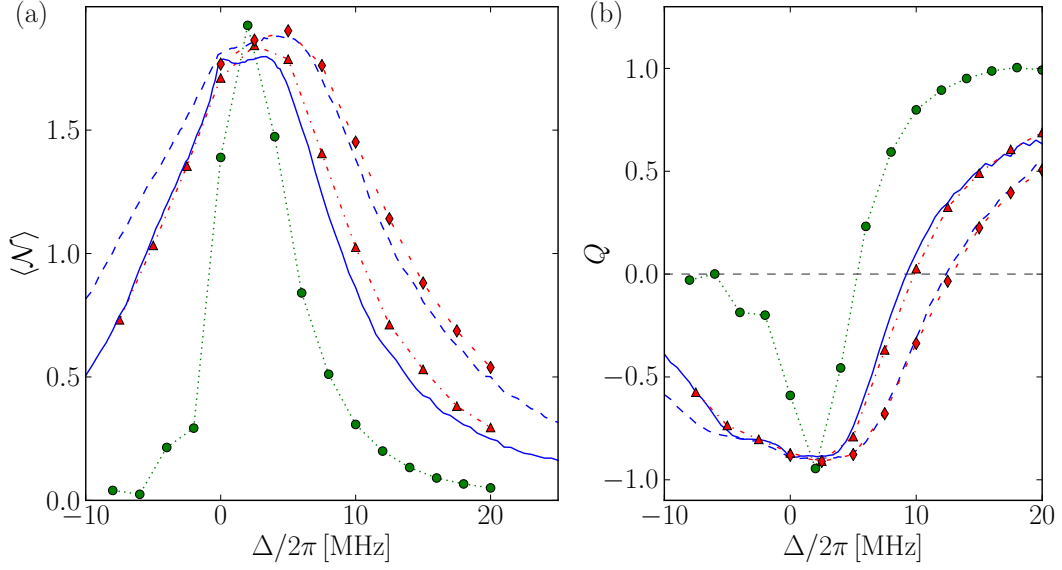
Figure 6.6: Rydberg population (a) and Mandel Q parameter (b) as a function of the laser detuning, comparing rate equation (blue), MCWF (red) and coherent [32] (green) simulation results. The solid, blue line as well as the red triangles correspond to $\Gamma/2\pi = 1$ whereas the dashed blue line and the red diamonds are obtained for $\Gamma/2\pi = 2$. Further parameters: $\Omega/2\pi = 0.3$, $\gamma = 0.025$ and $C_6/2\pi = 16\,000$. The dashed/dash-dotted/dotted lines connecting the data points are intended to serve as a guide to the eye only.

we employ an averaged Rabi frequency $\Omega/2\pi = 0.3$ rather than $\Omega_{12}\Omega_{23}/2\Delta_1 \simeq 0.4 \times 2\pi$, as

$$0.4 \times \frac{1}{2\sigma_{x'}} \int\limits_{-\sigma_{x'}}^{\sigma_{x'}} e^{-x^2/2\sigma_{x'}^2}\, dx \simeq 0.3\,. \tag{6.3}$$

Furthermore, $C_6/2\pi = 16\,000$, $\gamma = 0.025$ and $\Gamma/2\pi = 1$. Again, the dynamics is evaluated after $t = 5\,\mu s$. The state space is, in addition to the standard truncation, further truncated by applying the self-consistent condition $|E| \le C_6/R_b^{*6}$ on the energy of the basis states.

Note that while in Sections 6.3, 6.4 we used an effective two-level rate equation model including the three-level master equation parameters, the benchmark is performed using the literal two-level version of the rate equation employed above to allow for direct comparison of the simulation results of rate equation and two-level MCWF model respectively.

The results are shown in Figure 6.6. In Figure 6.6a, the Rydberg population has been plotted as a function of the detuning, comparing for two dephasing constants MCWF and rate equation simulation results as well as the coherent Schrödinger equation simulation. In Figure 6.6b, the Q parameters have been compared as a function of the detuning. For the benchmark parameters, the results of MCWF and rate equation calculation agree remarkably well. While, in the case of positive detunings, the population is slightly underestimated by the rate equation, especially for the smaller dephasing constant $\Gamma/2\pi = 1$, the Q parameters agree well, even at large detuning values. Both MCWF and rate equation simulations show a broadened excitation spectrum and Q parameter for increased dephasing. In contrast, the coherent simulation features a narrow excitation spectrum with coherent oscillations dominating the population dynamics for negative detunings. Additionally, the Q parameter yields significantly larger values for positive detunings than the MCWF simulations and decreases rapidly to zero for large negative detunings, as opposed to MCWF simulations. Accordingly, there is a pronounced difference between coherent and incoherent excitation dynamics in the considered regime, emphasizing the need for a model which takes into account
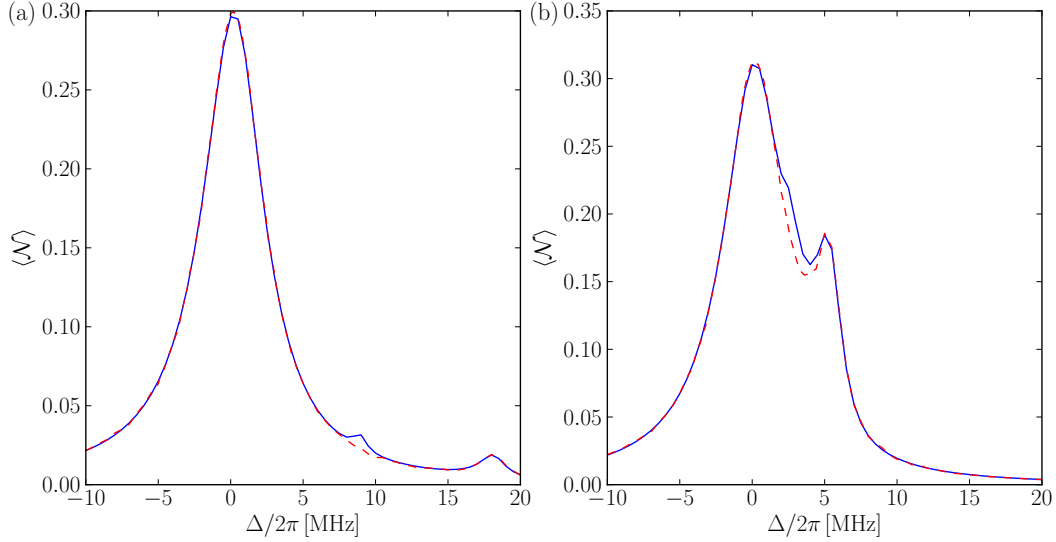
Figure 6.7: Four-atom steady-state Rydberg population, comparing rate equation (red, dashed) with exact master equation (blue, solid) calculation for different interaction strengths, $\mathcal{V}_{rr}/2\pi = 18$ (a) and $\mathcal{V}_{rr}/2\pi = 5$ (b), respectively. Note that the master equation data is more coarse-grained than the rate equation data.

incoherent effects.

In addition, we simulated the master equation for 4 atoms on a lattice with nearest neighbor interaction $\mathcal{V}_{rr}/2\pi \in \{5, 10, 18, 51\}$ and verified that the steady state of the kMC model ($t = 500\,\mu s$) agrees with the full master equation solution for the parameters stated in Section 6.1, except for the small two-photon contribution at $\Delta \simeq \mathcal{V}_{rr}/2$ (cf. Figure 6.7).

We also compared the $G^{(2)}$ function of the kMC model to MCWF simulations using the same geometry and laser parameters as above for $\Delta/2\pi = 15$. The MCWF simulation is repeated for zero dephasing, $\Gamma = 0$ for the same detuning as before. The resulting $G^{(2)}$ function is shown in the inset of Figure 6.5. Clearly, the laser dephasing strongly reduces the impact of two-photon processes which occur at smaller distances $R_{2\gamma} = (C_6/2\Delta)^{1/6}$, supporting the assumption that the dynamics of the system can be understood by considering single-photon resonance effects only. However, since the two-photon contribution does not totally vanish for the effective two-level parameters corresponding to the parameters given in Section 6.1, a small contribution of two-photon resonance effects particularly for the seeding excitation cannot be ruled out.

Finally, we estimated the impact of atomic motion on the excitation spectrum, which may play an important role in real systems' dynamics [90]. For this purpose, we solved the classical equations of motion arising from the repulsive van der Waals force for point-like atoms of mass $\mu \simeq 1.44 \times 10^{-25}\,\mathrm{kg}$ for ^{87}Rb atoms.

Specifically, we first abandoned the kinetic Monte Carlo algorithm by introducing a fixed numerical time step $\delta t = 0.01\,\mu s$ in the simulation. Though coming at the expense of computational efficiency, this step is required since, due to atomic motion, the (de-) excitation rates can change over time, invalidating the kinetic Monte Carlo procedure sketched in Algorithm 1, which relies on time-independent (de-) excitation rates. In principle, the kinetic Monte Carlo procedure can be modified such that it allows one to handle time-dependent rates by employing the integral of the rates over time instead of constant rates [76]; however, since the integral cannot be calculated analytically and numerical calculation involves discretization of time, abandoning kinetic Monte Carlo is the most convenient procedure. In the discretized Monte Carlo algorithm, a (de-) excitation process only takes place if the random number r_1
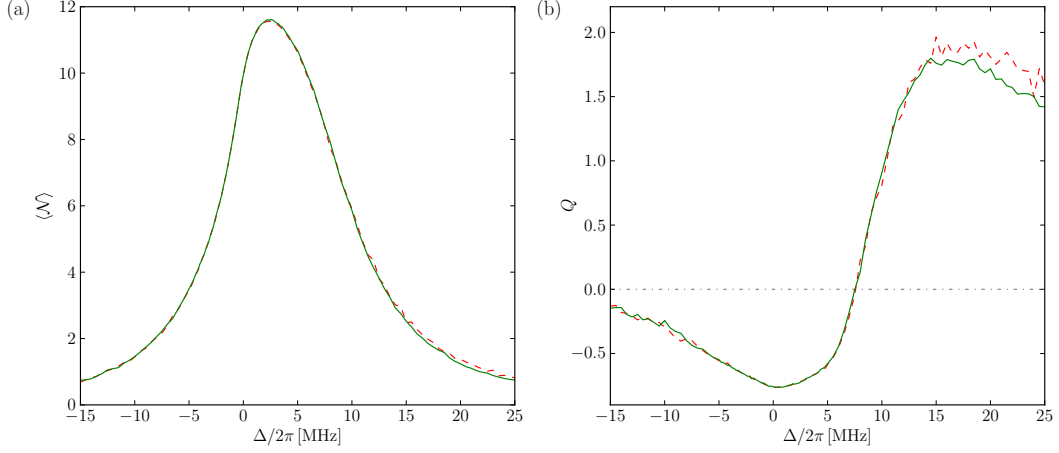
Figure 6.8: Rydberg population (a) and Q parameter (b) for the intermediate density $0.8 \times 10^{12}\,\mathrm{cm}^{-3}$. The red, dashed line indicates simulation results including the atomic motion induced by the repulsive van der Waals interaction as well as Doppler shifts caused by both thermal and interaction-induced motion. The green, solid line shows simulation results without motion.

is smaller than the total (de-) excitation rate times the numerical time step, $r_1 < \gamma_{\updownarrow\mathrm{tot}}\delta t$. If this is the case, the (de-) excitation process is determined as usual via linear search, i.e., the atom β which changes its state is determined via the condition $\min\{\beta \,|\, r_1 < \sum_{\alpha=1}^{\beta} \gamma_{\downarrow,\uparrow}^{(\alpha)} \delta t\}$. If $r_1 \geq \gamma_{\updownarrow\mathrm{tot}}\delta t$, which is true most of the time, the system remains in its current state.

In each time step, the force acting on the individual Rydberg atoms is determined by looping over all excited atoms and summing up the force that is exerted by each atom,

$$\mu\ddot{\boldsymbol{R}} = -\hbar\nabla\mathcal{V}_{rr} = 6\hbar\frac{C_6}{R^7}\hat{\boldsymbol{R}}. \tag{6.4}$$

Subsequently, the equations of motion are solved and the Rydberg interactions as well as the non-uniform Rabi frequencies are updated. In particular, the set of second-order differential equations is reduced to a set of first-order differential equations, which can be readily solved via `gsl` routines, by introducing the auxiliary variable $\dot{\boldsymbol{R}} = \boldsymbol{v}$.

As required by a self-consistent approach, the Doppler shifts induced by the atomic motion are implemented as well via Eq. (5.9). The initial conditions for the velocities are drawn from the Maxwell-Boltzmann distribution (5.10) with $T = 5\,\mu\mathrm{K}$.

The simulation results are shown in Figure 6.8 for the intermediate density $0.8 \times 10^{12}\,\mathrm{cm}^{-3}$. It can be seen that atomic motion leads to a slight increase of Rydberg excitations on the blue side of the spectrum, as well as to a larger Q parameter for large positive detunings. Overall, however, we found that the *classical* atomic motion as implemented in our model does not significantly change the excitation spectrum.

7 Summary and Further Research

By virtue of their tunable long-range interactions, Rydberg systems are particularly suitable for studying interacting many-body quantum systems. While in theory the most straightforward approach to study such systems is to consider them as being closed, i.e., not interacting with the surrounding environment, current experiments are almost always performed in the (weak) dissipative regime. What is more, most interesting applications of Rydberg systems employ atomic coherences in some way [6, 8, 10], giving rise to collective effects of truly quantum nature. Off-resonant excitation experiments of large atomic samples on the other hand require theory to provide models capable of following the dynamics of the system [4, 40].

Considering the theoretical models developed so far, there are (quasi) exact models which account for full quantum correlations, namely models based on the Schrödinger equation [23, 32], neglecting incoherent effects, and models which allow for simulating dissipative effects, such as the wave function Monte Carlo method [46, 47]. Both models are only applicable to rather small systems since they have to overcome the problem of exponentially growing Hilbert space, but allow the study of the dynamics of the system. Furthermore, there are effective models such as the rate equation, which can be applied to large systems, but provide only limited [35], or no [36] access to dynamical quantities. In this thesis we covered both kinds of approaches.

We implemented the wave function Monte Carlo method as an extension to an existing coherent many-body Schrödinger model [23, 32, 33] and characterized the properties of the resulting model. Specifically, we discussed the accuracy and robustness of our simulations with respect to parameters related to numerics and introduced the pair correlation function in the process. We found that the main caveat regarding the numerical simulation is the appropriate choice of the numerical time step in the strongly interacting and far-detuned regime, as we observed relative deviations of few ($\lesssim 2$) percent when varying the numerical time step. Enforcing an increased number of matrix-vector multiplications, which constitute the bottleneck of our simulation, the numerical time step was also found to reduce computational efficiency most, along with the total state number.

To check the reliability of our model in the many-body regime, we simulated super atom dephasing and noted excellent agreement with theoretical predictions, while both the rate equation model [36] and coherent calculation [23] turned out to fail for the chosen parameters ($\gamma = 0$, $\Gamma \neq 0$).

We then compared for the first time steady-state two-level rate equation results [36] to wave function Monte Carlo simulations and assessed the range of validity of the rate equation. In the strong dissipative regime ($\gamma \neq 0$, $\Gamma \gtrsim \Omega_{\text{eff}}$), the simulation results of both models showed good agreement for resonant as well as off-resonant excitation, whereas strong deviations, especially in the pair correlation function $G^{(2)}$, were found in the weak dissipative regime, where the approximations made in the derivation of the rate equation can no longer be applied. That is, ignoring of two-photon processes is invalidated when coherent excitation processes such as two-photon excitation become relevant, which is the case for small dephasing and in particular in lattice geometries with appropriate lattice spacing. The benchmark of rate equation models is of special interest as these models can easily be applied to realistic experimental setups.

Analyzing the impact of dephasing and decay on the pair correlation function $G^{(2)}$ in more detail, we saw that dephasing decreases the blockade radius and destroys the two-photon resonance, which can be understood in a simple two-atom picture in which the singly-excited states (more precisely, the symmetric state $|+\rangle$) can only be eliminated if a coherent description is possible, i.e., if the inter-atomic coherences are not destroyed by strong dephasing. Decay on

the other hand mainly smears out the structure of the pair correlation function on resonance.

For off-resonant excitation we found that, for positive detunings, an asymmetric excitation spectrum emerges, which can be attributed to resonant excitations that are possible if the detuning compensates for the energy shift induced by the Rydberg interaction. This stands in stark contrast to the super atom case where a symmetric excitation spectrum was observed with the steady-state value being independent of the detuning.

We discussed modifications made to the wave function Monte Carlo model to take into account the Doppler shift experienced by thermal Rydberg atoms as well as an experimental pulse shape. In spite of employing parameters comparable to the experimental ones [29], we found that for high atomic densities our two-level model could not reproduce the oscillations measured in the transmission of the laser light driving the lower ($|g\rangle \leftrightarrow |m\rangle$) transition. This we attributed to the disregard of the third level, which at the considered densities turned out to be even more crucial for correct modeling than taking into account full many-body correlations.

The Mandel Q parameter quantifying excitation number fluctuations was studied as a function of time in a one-dimensional, disordered gas for several detuning values in the presence of decoherence. We found non-trivial dynamics, in particular an increase of the Q parameter in the blockade regime ($\Delta = 0$) as well as a strong decrease of the Q parameter in the blue-detuned regime ($\Delta/2\pi = 15$), which was traced back to the slow equilibration time scale of the Rydberg population for very weak decay and strong interaction. In addition, a bimodal excitation statistics was encountered even at intermediate times ($t = 6\,\mu s$) in the weak dissipative regime, which we ascribed to dynamical effects, namely resonant pair excitations, that cause a clearly visible ground state fraction at intermediate times in small systems. The findings highlight the impact of the different time scales introduced by incoherent processes in experiments.

In the last part of the thesis we applied an effective two-level rate equation model to a particular experimental setup [4]. We analyzed the excitation dynamics resulting from our numerical simulation and identified the dominant mechanism by which excitations form as subsequent-growth-after-initial-seed mechanism, meaning that after an initial seed, Rydberg aggregates form mainly via resonant single-photon excitation. This mechanism causes enhanced excitation number fluctuations that manifest themselves via super-Poissonian Q values. Benchmark calculations using MCWF technique yielded good agreement with rate equation results. Our simulations shed light on the aggregate growth mechanism in a certain parameter regime, allowing an understanding of the excitation dynamics via rather classical reasoning.

Beyond the findings that have been presented in this thesis there are still many open questions to address. Concerning our simulations, the most prominent one is under which circumstances a weak dissipative many-body three-level system typically utilized in experiments can be accurately modeled by a two-level system. This issue is rather crucial since rate equations are not applicable in the weak dissipative regime, as we have seen in this thesis, and incoherent effects might lead to different dynamics comparing full quantum two- and three-level description. A possible approach to this matter is to extend the two-level treatment to a three-level one, which, at the cost of much smaller system sizes, would allow one to directly compare two- and three-level many-body simulations and discern parameter regimes of equivalent and dissimilar dynamics.

To generalize our simulation technique, one could allow for electronic states with larger angular momentum, such as Rydberg P states. Rydberg P states feature an interaction which depends on the relative orientation of the dipoles, hence qualitatively different dynamics are expected even for low-dimensional systems when applying different external fields.

Computational efficiency of our simulation in turn could be improved by harnessing graphics processing units (GPUs) for the calculation of the matrix-vector multiplication $\mathcal{H}_{\mathrm{nh}}|\psi\rangle$, in

that way rendering possible the simulation of larger system sizes, for instance.

Another open question concerns the validity of the classical treatment of the atomic positions, assumed distinct in this thesis, in contrast to what one would expect from a quantum mechanical wave function. Thorough analysis of full quantum calculations is required to provide a profound understanding of when the classical approximation of point particles that are exposed to an interaction potential of simple shape are no longer valid. In addition, it is far from obvious how atomic motion, induced by the Rydberg-Rydberg interaction, affects the excitation dynamics in cold Rydberg gases. Further research is needed in this specific area to reliably estimate the impact of motion in current experiments [90, 91].

Starting from our findings with respect to the dynamics of observables quantifying excitation statistics such as the Mandel Q parameter, we wonder whether these effects could be observed in experiments. A more profound understanding of the dynamical effects which depend on the distinct time scales given by Rabi frequency, Rydberg interaction, detuning, dephasing and decay would enable more accurate preparation techniques and avert false interpretations stemming from the neglect of time-dependence present in the measured observables.

Moreover, experimental $G^{(2)}$ measurements in disordered systems via imaging techniques, for instance, could confirm the established simulation techniques and provide an independent estimate on the strength of dissipative effects in current experiments.

Eventually, a more extensive numerical study on disordered gases using wave function Monte Carlo simulations in similar fashion as performed in Refs. [45–47, 75] for lattice geometries could answer questions pertaining to the intrinsic differences of lattice geometries compared to disordered geometries. The wave function Monte Carlo technique could also be applied to other dissipative systems (e.g. solid state systems) and could be compared to further state-of-the-art techniques, from both methodological and interpretational point of view.

Bibliography

[1] T. Gallagher, *Rydberg Atoms*. Cambridge Monographs on Atomic, Molecular and Chemical Physics. Cambridge University Press, Cambridge, 2005.

[2] D. Comparat and P. Pillet, "Dipole blockade in a cold Rydberg atomic sample (Invited)", *J. Opt. Soc. Am. B* **27** (Jun, 2010) A208–A232.

[3] P. Schauß, M. Cheneau, M. Endres, T. Fukuhara, S. Hild, A. Omran, T. Pohl, C. Gross, S. Kuhr, and I. Bloch, "Observation of spatially ordered structures in a two-dimensional Rydberg gas", *Nature* **491** (2012) 87–91.

[4] H. Schempp, G. Günter, M. Robert-de-Saint-Vincent, C. S. Hofmann, D. Breyel, A. Komnik, D. W. Schönleber, M. Gärttner, J. Evers, S. Whitlock, and M. Weidemüller, "Full counting statistics of laser excited Rydberg aggregates in a one-dimensional geometry", *ArXiv e-prints* (Aug., 2013), `arXiv:1308.0264`.

[5] T. Peyronel, O. Firstenberg, Q.-Y. Liang, S. Hofferberth, A. V. Gorshkov, T. Pohl, M. D. Lukin, and V. Vuletic, "Quantum nonlinear optics with single photons enabled by strongly interacting atoms", *Nature* **488** (2012) 57–60.

[6] D. Jaksch, J. I. Cirac, P. Zoller, S. L. Rolston, R. Côté, and M. D. Lukin, "Fast Quantum Gates for Neutral Atoms", *Phys. Rev. Lett.* **85** (Sep, 2000) 2208–2211.

[7] M. Saffman, T. G. Walker, and K. Mølmer, "Quantum information with Rydberg atoms", *Rev. Mod. Phys.* **82** (Aug, 2010) 2313–2363.

[8] M. Müller, I. Lesanovsky, H. Weimer, H. P. Büchler, and P. Zoller, "Mesoscopic Rydberg Gate Based on Electromagnetically Induced Transparency", *Phys. Rev. Lett.* **102** (Apr, 2009) 170502.

[9] H. Weimer, M. Müller, I. Lesanovsky, P. Zoller, and H. P. Büchler, "A Rydberg quantum simulator", *Nature Phys.* **6** (May, 2010) 382–388.

[10] M. Saffman and T. G. Walker, "Creating single-atom and single-photon sources from entangled atomic ensembles", *Phys. Rev. A* **66** (Dec, 2002) 065403.

[11] J. Honer, R. Löw, H. Weimer, T. Pfau, and H. P. Büchler, "Artificial Atoms Can Do More Than Atoms: Deterministic Single Photon Subtraction from Arbitrary Light Fields", *Phys. Rev. Lett.* **107** (Aug, 2011) 093601.

[12] F. Cinti, T. Macrì, W. Lechner, G. Pupillo, and T. Pohl, "Defect-induced supersolidity with soft-core Bosons", *ArXiv e-prints* (Feb., 2013), `arXiv:1302.4576`.

[13] D. Tong, S. M. Farooqi, J. Stanojevic, S. Krishnan, Y. P. Zhang, R. Côté, E. E. Eyler, and P. L. Gould, "Local Blockade of Rydberg Excitation in an Ultracold Gas", *Phys. Rev. Lett.* **93** (Aug, 2004) 063001.

[14] K. Singer, M. Reetz-Lamour, T. Amthor, L. G. Marcassa, and M. Weidemüller, "Suppression of Excitation and Spectral Broadening Induced by Interactions in a Cold Gas of Rydberg Atoms", *Phys. Rev. Lett.* **93** (Oct, 2004) 163001.

[15] A. Reinhard, K. C. Younge, and G. Raithel, "Effect of Förster resonances on the excitation statistics of many-body Rydberg systems", *Phys. Rev. A* **78** (Dec, 2008) 060702.

[16] E. Urban, T. A. Johnson, T. Henage, L. Isenhower, D. D. Yavuz, T. G. Walker, and M. Saffman, "Observation of Rydberg blockade between two atoms", *Nature Phys.* **5** (Jan, 2009) 110–114.

[17] C. S. Hofmann, G. Günter, H. Schempp, M. Robert-de Saint-Vincent, M. Gärttner, J. Evers, S. Whitlock, and M. Weidemüller, "Sub-Poissonian Statistics of Rydberg-Interacting Dark-State Polaritons", *Phys. Rev. Lett.* **110** (May, 2013) 203601.

[18] R. Heidemann, U. Raitzsch, V. Bendkowsky, B. Butscher, R. Löw, L. Santos, and T. Pfau, "Evidence for Coherent Collective Rydberg Excitation in the Strong Blockade Regime", *Phys. Rev. Lett.* **99** (Oct, 2007) 163601.

[19] Y. O. Dudin, L. Li, F. Bariani, and A. Kuzmich, "Observation of coherent many-body Rabi oscillations", *Nature Phys.* **8** (2012) 790–794.

[20] A. Gaetan, Y. Miroshnychenko, T. Wilk, A. Chotia, M. Viteau, D. Comparat, P. Pillet, A. Browaeys, and P. Grangier, "Observation of collective excitation of two individual atoms in the Rydberg blockade regime", *Nature Phys.* **5** (Feb., 2009) 115–118.

[21] L. Béguin, A. Vernier, R. Chicireanu, T. Lahaye, and A. Browaeys, "Direct Measurement of the van der Waals Interaction between Two Rydberg Atoms", *Phys. Rev. Lett.* **110** (Jun, 2013) 263201.

[22] H. Weimer, R. Löw, T. Pfau, and H. P. Büchler, "Quantum Critical Behavior in Strongly Interacting Rydberg Gases", *Phys. Rev. Lett.* **101** (Dec, 2008) 250601.

[23] M. Gärttner, K. P. Heeg, T. Gasenzer, and J. Evers, "Dynamic formation of Rydberg aggregates at off-resonant excitation", *Phys. Rev. A* **88** (Oct, 2013) 043410.

[24] T. Pohl, E. Demler, and M. D. Lukin, "Dynamical Crystallization in the Dipole Blockade of Ultracold Atoms", *Phys. Rev. Lett.* **104** (Jan, 2010) 043002.

[25] B. Olmos, W. Li, S. Hofferberth, and I. Lesanovsky, "Amplifying single impurities immersed in a gas of ultracold atoms", *Phys. Rev. A* **84** (Oct, 2011) 041607.

[26] J. Otterbach, M. Moos, D. Muth, and M. Fleischhauer, "Wigner Crystallization of Single Photons in Cold Rydberg Ensembles", *Phys. Rev. Lett.* **111** (Sep, 2013) 113001.

[27] J. D. Pritchard, D. Maxwell, A. Gauguet, K. J. Weatherill, M. P. A. Jones, and C. S. Adams, "Cooperative Atom-Light Interaction in a Blockaded Rydberg Ensemble", *Phys. Rev. Lett.* **105** (Nov, 2010) 193603.

[28] D. Petrosyan, J. Otterbach, and M. Fleischhauer, "Electromagnetically Induced Transparency with Rydberg Atoms", *Phys. Rev. Lett.* **107** (Nov, 2011) 213601.

[29] T. Baluktsian, B. Huber, R. Löw, and T. Pfau, "Evidence for Strong van der Waals Type Rydberg-Rydberg Interaction in a Thermal Vapor", *Phys. Rev. Lett.* **110** (Mar, 2013) 123001.

[30] J. B. Balewski, A. T. Krupp, A. Gaj, D. Peter, H. P. Büchler, R. Löw, S. Hofferberth, and T. Pfau, "Coupling a single electron to a Bose-Einstein condensate", *ArXiv e-prints* (June, 2013), `arXiv:1306.5181`.

[31] K. C. Younge, A. Reinhard, T. Pohl, P. R. Berman, and G. Raithel, "Mesoscopic Rydberg ensembles: Beyond the pairwise-interaction approximation", *Phys. Rev. A* **79** (Apr, 2009) 043420.

[32] M. Gärttner, K. P. Heeg, T. Gasenzer, and J. Evers, "Finite-size effects in strongly interacting Rydberg gases", *Phys. Rev. A* **86** (Sep, 2012) 033422.

[33] M. Gärttner, *Many-body effects in Rydberg gases.* PhD thesis, University of Heidelberg, 2013.

[34] C. Ates, T. Pohl, T. Pattard, and J. M. Rost, "Antiblockade in Rydberg Excitation of an Ultracold Lattice Gas", *Phys. Rev. Lett.* **98** (Jan, 2007) 023002.

[35] C. Ates, T. Pohl, T. Pattard, and J. M. Rost, "Many-body theory of excitation dynamics in an ultracold Rydberg gas", *Phys. Rev. A* **76** (Jul, 2007) 013413.

[36] K. P. Heeg, M. Gärttner, and J. Evers, "Hybrid model for Rydberg gases including exact two-body correlations", *Phys. Rev. A* **86** (Dec, 2012) 063421.

[37] M. Höning, D. Muth, D. Petrosyan, and M. Fleischhauer, "Steady-state crystallization of Rydberg excitations in an optically driven lattice gas", *Phys. Rev. A* **87** (Feb, 2013) 023401.

[38] D. Petrosyan, M. Höning, and M. Fleischhauer, "Spatial correlations of Rydberg excitations in optically driven atomic ensembles", *Phys. Rev. A* **87** (May, 2013) 053414.

[39] H. Schempp, G. Günter, C. S. Hofmann, C. Giese, S. D. Saliba, B. D. DePaola, T. Amthor, M. Weidemüller, S. Sevinçli, and T. Pohl, "Coherent Population Trapping with Controlled Interparticle Interactions", *Phys. Rev. Lett.* **104** (Apr, 2010) 173602.

[40] N. Malossi, M. M. Valado, S. Scotto, P. Huillery, P. Pillet, D. Ciampini, E. Arimondo, and O. Morsch, "Full counting statistics and phase diagram of a dissipative Rydberg gas", *ArXiv e-prints* (Aug., 2013), `arXiv:1308.1854`.

[41] H. J. Carmichael, *An open systems approach to quantum optics.* Springer, Berlin Heidelberg, 1993.

[42] J. Dalibard, Y. Castin, and K. Mølmer, "Wave-function approach to dissipative processes in quantum optics", *Phys. Rev. Lett.* **68** (Feb, 1992) 580–583.

[43] R. Dum, P. Zoller, and H. Ritsch, "Monte Carlo simulation of the atomic master equation for spontaneous emission", *Phys. Rev. A* **45** (Apr, 1992) 4879–4887.

[44] K. Mølmer, Y. Castin, and J. Dalibard, "Monte Carlo wave-function method in quantum optics", *J. Opt. Soc. Am. B* **10** (Mar, 1993) 524–538.

[45] C. Ates, B. Olmos, J. P. Garrahan, and I. Lesanovsky, "Dynamical phases and intermittency of the dissipative quantum Ising model", *Phys. Rev. A* **85** (Apr, 2012) 043620.

[46] T. E. Lee and M. C. Cross, "Spatiotemporal dynamics of quantum jumps with Rydberg atoms", *Phys. Rev. A* **85** (Jun, 2012) 063822.

[47] T. E. Lee, H. Häffner, and M. C. Cross, "Collective Quantum Jumps of Rydberg Atoms", *Phys. Rev. Lett.* **108** (Jan, 2012) 023602.

[48] I. Martinson and L. Curtis, "Janne Rydberg – his life and work", *Nucl. Instr. Meth. Phys. Res. B* **235** (2005) 17 – 22.

[49] W. Demtröder, *Experimentalphysik 3.* Springer, Berlin Heidelberg, 2009.

[50] P. Meystre and M. Sargent, *Elements of Quantum Optics*. Springer, Berlin Heidelberg, 2007.

[51] C. S. Hofmann, *Emergence of correlations in strongly interacting ultracold Rydberg gases*. PhD thesis, University of Heidelberg, 2013.

[52] N. Tezak, "Spectra and Excitation Dynamics of Laser-driven Lattices of Ultracold Rydberg Atoms", Diploma thesis, University of Heidelberg, 2010.

[53] T. G. Walker and M. Saffman, "Consequences of Zeeman degeneracy for the van der Waals blockade between Rydberg atoms", *Phys. Rev. A* **77** (Mar, 2008) 032723.

[54] K. Singer, J. Stanojevic, M. Weidemüller, and R. Côté, "Long-range interactions between alkali Rydberg atom pairs correlated to the n s– n s, n p– n p and n d– n d asymptotes", *J. Phys. B* **38** (2005) S295.

[55] K. P. Heeg, "Models for correlated Rydberg gases", Diploma thesis, University of Heidelberg, 2011.

[56] M. D. Lukin, M. Fleischhauer, R. Cote, L. M. Duan, D. Jaksch, J. I. Cirac, and P. Zoller, "Dipole Blockade and Quantum Information Processing in Mesoscopic Atomic Ensembles", *Phys. Rev. Lett.* **87** (Jun, 2001) 037901.

[57] F. Robicheaux and J. V. Hernández, "Many-body wave function in a dipole blockade configuration", *Phys. Rev. A* **72** (Dec, 2005) 063403.

[58] J. Stanojevic and R. Côté, "Many-body dynamics of Rydberg excitation using the Ω expansion", *Phys. Rev. A* **81** (May, 2010) 053406.

[59] M. Scully and S. Zubairy, *Quantum Optics*. Cambridge University Press, Cambridge, 1997.

[60] B. Shore, *Manipulating Quantum Structures Using Laser Pulses*. Cambridge University Press, Cambridge, 2011.

[61] M. Nielsen and I. Chuang, *Quantum Computation and Quantum Information: 10th Anniversary Edition*. Cambridge University Press, Cambridge, 2010.

[62] H. Breuer and F. Petruccione, *The Theory of Open Quantum Systems*. Oxford University Press, Oxford, 2002.

[63] A. Rivas and S. Huelga, *Open Quantum Systems: An Introduction*. Springer, Berlin Heidelberg, 2011.

[64] H. Wiseman and G. Milburn, *Quantum Measurement and Control*. Cambridge University Press, Cambridge, 2010.

[65] G. Schaller, "Non-Equilibrium Master Equations", TU Berlin, lecture notes, Feb, 2012. `http://wwwitp.physik.tu-berlin.de/~schaller/download/NEQME1.pdf`.

[66] J. Gea-Banacloche, Y.-q. Li, S.-z. Jin, and M. Xiao, "Electromagnetically induced transparency in ladder-type inhomogeneously broadened media: Theory and experiment", *Phys. Rev. A* **51** (Jan, 1995) 576–584.

[67] V. Paulisch, R. Han, H. Khoon Ng, and B.-G. Englert, "Beyond adiabatic elimination: A hierarchy of approximations for multi-photon processes", *ArXiv e-prints* (Sept., 2012), `arXiv:1209.6568`.

[68] B. T. Torosov and N. V. Vitanov, "Adiabatic elimination of a nearly resonant quantum state", *J. Phys. B* **45** (2012) 135502.

[69] F. Reiter and A. S. Sørensen, "Effective operator formalism for open quantum systems", *Phys. Rev. A* **85** (Mar, 2012) 032111.

[70] E. M. Kessler, "Generalized Schrieffer-Wolff formalism for dissipative systems", *Phys. Rev. A* **86** (Jul, 2012) 012126.

[71] R. Löw, H. Weimer, U. Krohn, R. Heidemann, V. Bendkowsky, B. Butscher, H. P. Büchler, and T. Pfau, "Universal scaling in a strongly interacting Rydberg gas", *Phys. Rev. A* **80** (Sep, 2009) 033422.

[72] M. Kiffner, M. Macovei, J. Evers, and C. Keitel, "Chapter 3 - Vacuum-Induced Processes in Multilevel Atoms", in *Progress in Optics*, E. Wolf, ed., vol. 55 of *Progress in Optics*, pp. 85 – 197. Elsevier, Amsterdam, 2010.

[73] J. Mompart and R. Corbalán, "Quantum-jump approach to dipole dephasing: Application to inversionless amplification", *Eur. Phys. J. D* **5** (1999) 351–356.

[74] R. Puri, *Mathematical Methods of Quantum Optics*. Springer, Berlin Heidelberg, 2001.

[75] D. Petrosyan, "Dynamics and equilibration of Rydberg excitations in dissipative atomic ensembles", *J. Phys. B* **46** (July, 2013) 141001.

[76] A. Chotia, M. Viteau, T. Vogt, D. Comparat, and P. Pillet, "Kinetic Monte Carlo modeling of dipole blockade in Rydberg excitation experiment", *New J. Phys.* **10** (2008) 045031.

[77] A. P. J. Jansen, "An Introduction To Monte Carlo Simulations Of Surface Reactions", *ArXiv e-prints* (Mar., 2003), `arXiv:cond-mat/0303028`.

[78] M. Heath, *Scientific Computing: An Introductory Survey (2nd International Edition)*. McGraw-Hill Higher Education, New York, 2002.

[79] C. Ates, S. Sevinçli, and T. Pohl, "Electromagnetically induced transparency in strongly interacting Rydberg gases", *Phys. Rev. A* **83** (Apr, 2011) 041802.

[80] M. Gärttner and J. Evers, "Nonlinear absorption and density-dependent dephasing in Rydberg electromagnetically-induced-transparency media", *Phys. Rev. A* **88** (Sep, 2013) 033417.

[81] W. Dunn and J. Shultis, *Exploring Monte Carlo Methods*. Elsevier Science, Amsterdam, 2011.

[82] J. V. Hernández and F. Robicheaux, "Coherence conditions for groups of Rydberg atoms", *J. Phys. B* **39** (2006) 4883–4893.

[83] N. Bell and M. Garl, "Efficient sparse matrix-vector multiplication on CUDA", Tech. Rep. NVR-2008-004, NVIDIA, 2008.

[84] M. Fleischhauer, A. Imamoglu, and J. P. Marangos, "Electromagnetically induced transparency: Optics in coherent media", *Rev. Mod. Phys.* **77** (Jul, 2005) 633–673.

[85] M. Tanasittikosol, C. Carr, C. S. Adams, and K. J. Weatherill, "Subnatural linewidths in two-photon excited-state spectroscopy", *Phys. Rev. A* **85** (Mar, 2012) 033830.

[86] B. Huber. Private communication, Sept., 2013.

[87] C. Ates, T. Pohl, T. Pattard, and J. M. Rost, "Strong interaction effects on the atom counting statistics of ultracold Rydberg gases", *J. Phys. B* **39** (2006) L233.

[88] M. Galassi and B. Gough, *GNU Scientific Library: Reference Manual.* GNU manual. Network Theory Limited, 2009.

[89] C. Ates, *Anregungsdynamik ultrakalter Rydberggase.* PhD thesis, TU Dresden, 2009.

[90] W. Li, C. Ates, and I. Lesanovsky, "Nonadiabatic Motional Effects and Dissipative Blockade for Rydberg Atoms Excited from Optical Lattices or Microtraps", *Phys. Rev. Lett.* **110** (May, 2013) 213005.

[91] T. Macri and T. Pohl, "Rydberg-dressing of atoms in optical lattices", *ArXiv e-prints* (Aug., 2013), `arXiv:1308.5562`.

Acknowledgments

Erklärung:

Ich versichere, dass ich diese Arbeit selbstständig verfasst habe und keine anderen als die angegebenen Quellen und Hilfsmittel benutzt habe.

Heidelberg, den 31. Oktober 2013   . . . .